Final report
on the Partner Project Agreement

P-051

OPTICAL VORTICES UNDERSTANDING AND ASSESSMENT

Between

THE SCIENCE AND TECHNOLOGY CENTER IN UKRAINE

and

Institute of Physics, National Academy of Sciences of Ukraine

and
European Office of Aerospace Research and Development

Kyiv,

October 2001

REPORT DOCUMENTATION PAGE

Form Approved OMB No. 0704-0188

1. REPORT DATE (DD-MM-YYYY)	2. REPORT TYPE	3. DATES COVERED (FROM - TO)
30-10-2001	Final	01-10-2000 to 07-11-2001

4. TITLE AND SUBTITLE
Optical Vortices: Understanding and Assessment
Unclassified

5a. CONTRACT NUMBER
5b. GRANT NUMBER
5c. PROGRAM ELEMENT NUMBER

6. AUTHOR(S)
Soskin, Marat S. ;

5d. PROJECT NUMBER
5e. TASK NUMBER
5f. WORK UNIT NUMBER

7. PERFORMING ORGANIZATION NAME AND ADDRESS
Institute of Physics, National Academy of Sciences of Ukraine
Prospect Nauki 46
Kiev, Ukraine39 03650

8. PERFORMING ORGANIZATION REPORT NUMBER

9. SPONSORING/MONITORING AGENCY NAME AND ADDRESS
EOARD
PSC 802 BOX 14
FPO, 09499-0014

10. SPONSOR/MONITOR'S ACRONYM(S)
11. SPONSOR/MONITOR'S REPORT NUMBER(S)

12. DISTRIBUTION/AVAILABILITY STATEMENT
APUBLIC RELEASE
,

13. SUPPLEMENTARY NOTES

14. ABSTRACT
This report results from a contract tasking Institute of Physics, National Academy of Sciences of Ukraine. Optical vortices (OVs) are unique optical objects, existing around phase singularities in electromagnetic fields. Their unique properties allow possible applications that include 'optical traps' for cold atoms, OV optical tweezers for microparticles, data transmission through optical communications systems, correction of phase distortions in an adaptive optical system, testing a turbulent atmosphere, etc. In this project the contractor will conduct theoretical studies and experiments to 1) better define the quantum properties of OV; 2) explore OV optical tweezers; and 3) examine vortex sensors with extremely high sensitivity.

15. SUBJECT TERMS
EOARD; Physics; Optics

16. SECURITY CLASSIFICATION OF:			17. LIMITATION OF ABSTRACT	18. NUMBER OF PAGES	19. NAME OF RESPONSIBLE PERSON
a. REPORT	b. ABSTRACT	c. THIS PAGE	Public Release	78	Fenster, Lynn lfenster@dtic.mil
Unclassified	Unclassified	Unclassified			19b. TELEPHONE NUMBER International Area Code Area Code Telephone Number 703767-9007 DSN 427-9007

REPORT DOCUMENTATION PAGE

Form Approved OMB No. 0704-0188

1. REPORT DATE *(DD-MM-YYYY)*	2. REPORT TYPE	3. DATES COVERED *(From – To)*
30-10-2001	Final Report	01-Oct-00 - 07-Nov-01

4. TITLE AND SUBTITLE

OPTICAL VORTICES: UNDERSTANDING AND ASSESSMENT

5a. CONTRACT NUMBER
STCU Registration No: P-051
EOARD Project 008002

5b. GRANT NUMBER

5c. PROGRAM ELEMENT NUMBER

6. AUTHOR(S)

Professor Marat S Soskin

5d. PROJECT NUMBER

5d. TASK NUMBER

5e. WORK UNIT NUMBER

7. PERFORMING ORGANIZATION NAME(S) AND ADDRESS(ES)

Institute of Physics, National Academy of Sciences of Ukraine
Prospect Nauki 46
Kiev - 39 03650
Ukraine

8. PERFORMING ORGANIZATION REPORT NUMBER

N/A

9. SPONSORING/MONITORING AGENCY NAME(S) AND ADDRESS(ES)

EOARD
PSC 802 BOX 14
FPO 09499-0014

10. SPONSOR/MONITOR'S ACRONYM(S)

11. SPONSOR/MONITOR'S REPORT NUMBER(S)
STCU 00-8002

12. DISTRIBUTION/AVAILABILITY STATEMENT

Approved for public release; distribution is unlimited.

13. SUPPLEMENTARY NOTES

14. ABSTRACT

This report results from a contract tasking Institute of Physics, National Academy of Sciences of Ukraine. Optical vortices (OVs) are unique optical objects, existing around phase singularities in electromagnetic fields. Their unique properties allow possible applications that include 'optical traps' for cold atoms, OV optical tweezers for microparticles, data transmission through optical communications systems, correction of phase distortions in an adaptive optical system, testing a turbulent atmosphere, etc. In this project the contractor will conduct theoretical studies and experiments to 1) better define the quantum properties of OV; 2) explore OV optical tweezers; and 3) examine vortex sensors with extremely high sensitivity.

15. SUBJECT TERMS
EOARD, Physics, Optics

16. SECURITY CLASSIFICATION OF:			17. LIMITATION OF ABSTRACT	18, NUMBER OF PAGES	19a. NAME OF RESPONSIBLE PERSON
a. REPORT	b. ABSTRACT	c. THIS PAGE			Ronald D. Reed
UNCLAS	UNCLAS	UNCLAS	UL	77	19b. TELEPHONE NUMBER *(Include area code)* +44 (0)20 7514 4318

C o n t e n t s

4.3.4 Technique of high-efficiency synthesis of optical-vortex laser beams.
4.3.5 Technique of measurements with OVFS.
4.3.6 Programming of computer processing of the measurement data.
4.3.7 The stability of OVFS parameters. Testing protocol.

4.4. Pulse VFOS (theory, schemes and parameters assessment) (task 5).

5. Summary and conclusion of the project P-051 results

Chapter 1

Introduction: the project objectives, tasks and the report structure

Key words: optical vortices, phase singularities, orbital angular momentum, computer-synthesized holographic optical elements, low-mode optical fibers, vortex modes of optical fibers, optical-vortex fiber sensors.

A wide class of effects associated with phase singularities in optical wave fields, as well as topology of wave fronts, became recently the subject of *singular optics*, new chapter of modern photonics [1]. Although phase is an auxiliary function in electromagnetic field description, it is very useful as it gives a perception of a wave propagation and transformation along its path. An important relevant conception is a wave front, or a surface of equal phase, usually associated with a crest of a wave, where the field strength attains its highest value. The normal to the wave front, or phase gradient direction, shows the Poynting vector direction of energy flow, at least in the geometrical optics approximation [2]. The wave fronts follow each other with spatial separation in one wavelength, and between two neighbor crests there are two surfaces where field strength attains zero value, and one surface where field reaches minimum (negative) value (trough). This perfect regular motion, being true for a plane wave, can be violated for real waves. In brief, phase of a wave can experience a "π-jump", which corresponds to a step on a half of a wavelength in a wave train, producing a *phase defect* of a wave front along a continuous line in space. For instance, some physical reasons can lead to local variation of a phase velocity across a wave front. Resulting bending of the wave front can lead to its tear, and the phase becomes indeterminate, or *singular* along the tear. The necessary and sufficient condition for phase singularity to appear is the vanishing of the field amplitude. According to the classification introduced by Nye and Berry [3], a monochromatic light wave can possess two main types of phase singularities: *screw* wave-front dislocation and *edge* dislocation, while mixed edge-screw dislocation is most common situation. Nowadays the term "*optical vortex*" (OV) [4] became widely used, reflecting the general feature of phase singularities: phase circulation around the dislocation line. Therefore, a pure screw dislocation is an example of a "longitudinal" OV, and edge dislocation is the "transversal" OV, with respect to the wave propagation direction.

There is now theoretically predicted [5] and experimentally verified [6] conclusion on the existence of an *orbital angular momentum* for the longitudinal OV beam. It could be treated as well as classical effect, caused by the tangential (azimuth) component of the Poynting vector, as inherent quantum property of a photon [7]. The deep insight to the problem seems to be important, as both explanations have some obscurities.

Most important for fundamentals and applications are longitudinal OVs, which possess zero-amplitude axis and helicoidal wave front. A vortex core can be described with a factor $r^{|m|}\exp(im\varphi)$, where r is the radius, φ is the azimuth angle, and m is the signed integer called OV *topological charge.* Therefore, a laser beam with an axial OV looks like dark-core "hollow" self-similar beam, which preserves its structure up to infinity, i.e. to the far field. The unique properties of OVs open a variety of possibilities for new applications.

The investigations of fundamental properties and possible applications of OVs develop rapidly during last years [8,9]. This is clearly seen from the Proceedings of SPIE vol. 3487 [10] and vol. 4403 [11] of the 1st (1997) and the 2nd (2000) International Conferences on Singular Optics (Optical Vortices), organized by Institute of Physics, NAS of Ukraine, sponsored by many organizations, including EOARD**.** The essential account in organization of these conferences was done by Prof. A. V. Volyar with co-workers from Tavrida National University (Simferopol, Crimea, Ukraine), the leading group in the area of investigations and applications of optical vortices in fiber optics.

At the same time many principal questions of optical vortices understanding and assessment are still not established. To make an essential contribution to this problem was the goal of the Partner Project P-051.

The project **objectives** were twofold:

- more deep understanding of OVs unique properties, including their topological and quantum features, which are new for classical optics;

- the assessment of possible new applications of OVs mainly in optical-vortex fiber sensors with high sensitivity and multi-channel optical tweezers for manipulation with a system of micro-particles.

The investigations were carried out in two institutions, which gained a reach experience in OVs and are leading groups in singular optics:

1. INSTITUTE OF PHYSICS, NATIONAL ACADEMY OF SCIENCES OF UKRAINE
Prospect Nauki 46, Kyiv-39, 03650, Ukraine,
Tel.: +(38044) 265 12 20; Fax +(38044) 265 15 89: e-mail: negriyko@marion.iop.kiev.ua

2. TAVRIDA NATIONAL UNIVERSITY, SIMFEROPOL, CRIMEA, UKRAINE
Yaltinskaya 4, Simferopol, 95007, Crimea, Ukraine
Tel.: +(380652) 23 22 80, Fax: +(380652) 23 23 10; e-mail: rector@ccssu.crimea.ua

Project Manager

Soskin Marat S., correspondent-member of National Academy of Sciences of Ukraine, Professor, Head of Department of Optical Quantum Electronics, Institute of Physics, National Academy of Sciences of Ukraine,
Tel.: +(38044) 265 55 63; Fax +(38044) 265 15 89: e-mail: msoskin@iop.kiev.ua and marats@vortex.kiev.ua

The following **activities** were planned to perform the project objectives:

Task 1. Theoretical consideration of the linear and nonlinear optical effects, which embrace OV beams. This task was planned to contribute to the optical vortices understanding (report and publications) and has been performed by IP NASU.

Task 2. Experimental investigations of OV beams diffraction and interference. This task was planned to contribute to the assessment of possible applications of optical vortices (report and publications) and has been performed by IP NASU.

Task 3. Theoretical and experimental research of OV use in multi-channel tweezers. This task was planned to contribute to the assessment of optical vortices possible applications for manipulating with system of micro-particles (modeling and report) and has been performed by IP NASU.

Task 4. Theoretical and experimental studies of optical-vortex fiber sensors. This task was planned to contribute to the proposed optical-vortex sensor assessment (report, test protocol, publications) and has been performed by TNU.

Task 5. Consideration and computer simulation of applicability of short-pulse lasers in OV fiber sensors. This task was planned to contribute to the assessment of the proposed sensor application area (report) and has been performed by TNU.

The final report structure is built in accordance with the described scope of activities and consists from three chapters with text, figures, summary and general conclusion.

It is seen that the project objectives cover a wide scope of manifold specific effects in free space propagation, optical fibers, etc. To facilitate the reading and evaluation of this huge material each relatively independent section possesses its own numeration of formulae, figures and references.

References

1. M.S. Soskin and M.V. Vasnetsov, Photonics Science News **4**, issue 4, 21-42(1999).
2. M. Born and E. Wolf, Principles of Optics, 6th ed. (Pergamon Press, Oxford, 1980).
3. J. F. Nye and M. V. Berry, Proc. Roy. Soc. Lond. A **336**, 165-190 (1974).
4. P. Coullet, L. Gil and F. Rocca, "Optical vortices", Opt. Commun. **73** 403-408 (1989).
4. L. Allen, M. W. Beijersbergen, R. J. C. Spreeuw and J. P. Woerdman, Phys. Rev. A **45**, 8185 (1992).
5. H. He, M. E. J. Friese, N. R. Heckenberg and H. Rubinsztein-Dunlop, Phys. Rev. Lett. **75**, 826 (1995).
6. N. B. Simpson, K. Dholakia, L. Allen and M. J. Padgett, Optics Lett. **22**, 52 (1997).
7. Optical Vortices, M. Vasnetsov and K. Staliunas eds, Nova Science Publishers, NY (1999).
8. J. F. Nye, *Natural focusing and fine structure of light: Caustics and wave dislocations* (Institute of Physics Publishing, Bristol and Philadelphia (1999).
9. M. S. Soskin and M. V. Vasnetsov, "Singular Optics", Progress in Optics **42** (2001) (in press).
10. Proc. of SPIE, v. **3487** *Int. Conf. on Singular Optics,* ed. M. Soskin (Partenit, Crimea, Ukraine, October 1997) (Bellingham, USA, 1998).
11. Proc. of SPIE, v. **4403,** 2nd *Int. Conf. on Singular Optics,* ed. M. Soskin and M. Vasnetsov (Alushta, Crimea, Ukraine, October 2000) (Bellingham, USA, 2001).

Chapter 2

Interference and diffraction phenomena, nonlinear effects in light beams with optical vortices

2.1. Introduction

As it was pointed out above, light beams with optical vortices and/or edge dislocations of wave front possess quite new properties, which are absent in light beams with "usual" smooth wave front. This is connected mainly with the next new features of light beams with dislocations of wave front:

- helical wave-front shape for optical vortices or wave-front phase steps for edge dislocations,

- non-zero orbital angular momentum of OV light beams, which conserves at free propagation.

Our analysis of state-of-art of OVs understanding at the beginning of the project has shown that some basic optical phenomena like interference and diffraction of OV light beams were not considered yet carefully. Therefore, we tried to fill this gap during fulfillment of the project for better understanding of OV physics, according to the tasks 1 and 2.

The material is arranged in the following way, natural from our point of view:

(i) basic properties of phase singularities in combined light beams with two mutually coherent Gaussian beams and unusual transformation of OV beam orbital angular momentum and total topological charge by cylindrical lens in the focal plane and its vicinity (2.2 – 2.7),
(ii) second harmonic generation with OV beams with fractional topological charges (2.8).

2.2. Transversal Optical Vortices in a Light Wave: Structure and Topological Reactions

The purpose of the present paragraph is to report a study of a structure of wave-front edge dislocations in an interference field of two-dimensional (2D) Gaussian beams and to discuss the topological reactions, which occur in the process of saddle-vortex collision. The central question is to find the condition, which determines the direction of an "optical vortex" circulation around the dislocation line, which is a line of zero amplitude of the field. In contrast to the configuration used in [1], we now simplify the problem to 2D (cylindrical) waves and therefore can operate within scalar wave field approximation.

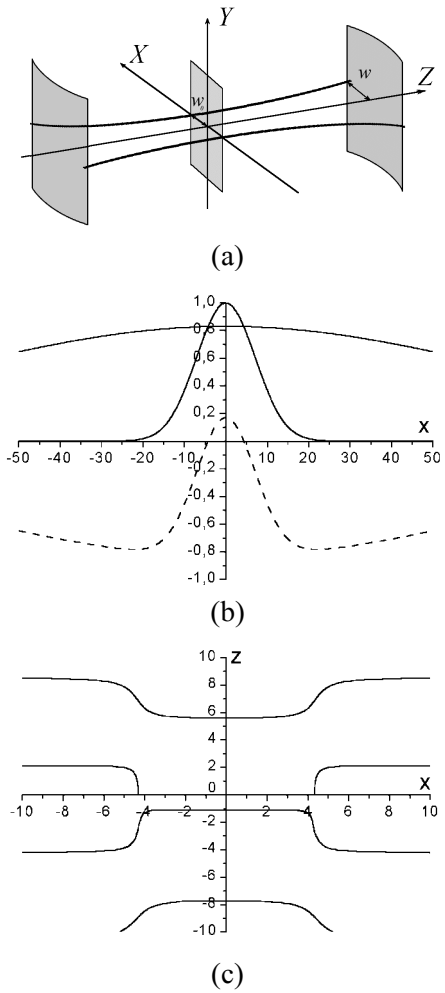

Fig. 1. . (a) A schematic view of a 2D Gaussian beam with the waist located at $z = 0$ position. (b) Destructive interference of two 2D Gaussian beams with different waist parameters. Resulting amplitude distribution in the waist is shown by dashed line. Negative amplitude denotes the π phase shift. (c) A wave-front sequence near the waist ($\Phi_1 = 1$): there is a lack of one wave front between the dislocation lines. The wave-front ledge before the waist is directed along the direction of the wave propagation and opposite after the waist.

The geometry of waves is explained in Fig. 1. A structure of a single 2D Gaussian beam is shown in Fig. 1a, with the beam waist at $z = 0$ position. The beam is polarized along Y-axis and propagates along Z-axis, with diffraction spread-out in $\pm X$-axis directions. For this 2D beam of Gaussian shape the paraxial solution satisfying paraxial wave equation looks as follows:

$$E(x,z) = E_G \sqrt{\frac{w_0}{w}} \exp\left(-\frac{x^2}{w^2} \right) \exp i\left(\frac{kx^2}{2R(z)} - \frac{1}{2}\arctan\frac{z}{z_R} + kz + \Phi \right), \quad (1)$$

where E_G is the amplitude parameter, w_0 is the waist parameter, k is the wavenumber, z_R is the Rayleigh range, $z_R = kw_0^2/2$, $R(z)$ is the radius of the wave front curvature in the XZ plane, $w = w_0(1+z^2/z_R^2)^{1/2}$, Φ is a constant phase term.

The solution (1) is very similar to the description of 3D Gaussian beam (see 2.5), except another degree of amplitude diminishing along the propagation path z, $(w_0/w)^{1/2}$, instead of (w_0/w) for 3D Gaussian beam, and coefficient ½ before the Gouy phase shift $\arctan(z/z_R)$.

To produce a pair of edge dislocations parallel to the Y-axis in the plane $z = 0$, let us make a superposition of two 2D Gaussian beams with different amplitudes $E_1 > E_2$, waist parameters $w_2 > w_1$, and a phase shift π between their phases Φ_1 and Φ_2, very similar to how it has been done for 3D Gaussian beams [1]:

$$E(x, z=0) = E_1 \exp\left(-\frac{x^2}{w_1^2} \right) \exp i\Phi_1 + E_2 \exp\left(-\frac{x^2}{w_2^2} \right) \exp i\Phi_2 . \quad (2)$$

At the waist plane, both waves have plane wave front, and their relative phases are locked as $\Phi_1 = \Phi_2 + \pi$, thus producing destructive interference, as shown in Fig.1b.

The edge dislocation position (zero amplitude of the field) is determined by

$$x_0 = \pm\sqrt{\frac{w_1^2 w_2^2}{w_2^2 - w_1^2} \ln(E_1/E_2)}. \quad (3)$$

For the analysis below, we define the ratio E_2/E_1 as the governing parameter η. A family of wave fronts (crests) is shown in figure1b for $\eta = 0.83$, $w_1 = 10$, $w_2 = 100$, $\Phi_1 = 1$. (Here and below all ranges are normalized for $k = 1$). First, it is seen from Fig. 1c that there is a lack of one wave front inside the interval bordered by edge dislocations. Before the waist, the wave front has a ledge along the direction of propagation, after the waist the ledge is directed opposite. The ledge is smoothed far from the waist and the resulting lack of the wavefront results in a small wavelength difference within the interval between the dislocations and outside, or phase velocity variation. The phase velocity is larger within the interval between the dislocations, the physical reason is the Gouy effect [2]: a spatially compressed light beam increases the phase velocity on the axis. To calculate the phase velocity of a 2D Gaussian beam in the waist, Eq. (1) can be applied:

$$v = c\left(1 + \frac{x^2}{2z_R^2} - \frac{1}{2kz_R} \right)^{-1}, \quad (4)$$

where c is the speed of light. There is a distance x_v where $v = c$: $x_v = w_0/\sqrt{2}$. When $x < x_v$, the phase velocity exceeds c, and vice versa. Due to this phase velocity variation, a wave front being plane at the waist gradually transforms to cylindrical at the far field.

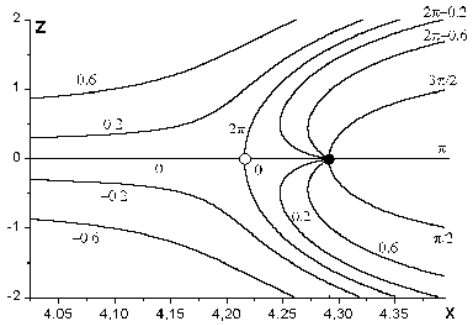

Fig. 2. Lines of equal phase of the interference field produced by two 2D Gaussian beams in the cross-section *XZ* nearby the edge dislocation, for $\eta = 0.83$, $\Phi_1 = 0$. Saddle point is indicated as a circle, vortex as a dot. There is a π-jump of the phase at the zero-amplitude point (core of the vortex).

Figure 2 shows a family of equiphase lines in the cross-section *XZ* in the vicinity of the edge dislocation, for $\eta = 0.83$. There is an additional wave front outside the inner stripe between the dislocation lines, and a point where it enters the periodic sequence: here, at the phase saddle, lines of $\Phi(x,z) = 0$ and $\Phi(x,z) = 2\pi$ join.

Analysis shows that the position of the saddle can be as inside the interval x_0, ($x_s < x_0$), as outside it ($x_s > x_0$). The physical sense of the saddle point is the condition of the energy current stagnation: vortex flow is exactly compensated by the longitudinal flow, and a line of standing wave is created. Therefore the vorticity area is ended in the saddle point, and the whole torous light current around the zero-amplitude line is localized in a very narrow region. In comparison with the wavelength, the separation between the vortex and the saddle is extremely small and amounts of about 10^{-2} of the wavelength.

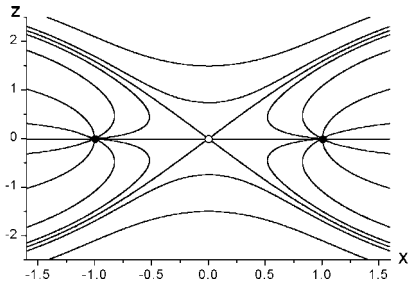

(a)

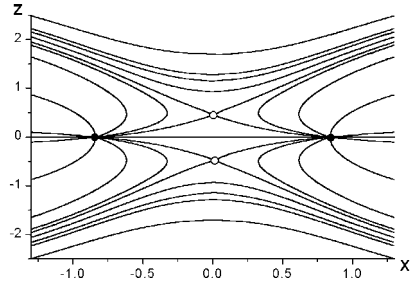

(b)

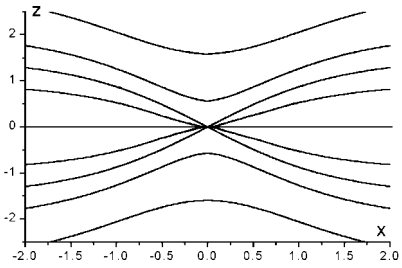

(c)

Fig. 3. Collapse of edge dislocations. (a) Equiphase lines around the dislocations, which are close to the beam center, saddle points have joint. (b) Vortices approach closer, saddles are split along the *Z*-axis. (c) All topological objects collide and annihilate at $\eta = 1$.

With increasing η, x_0 diminishes according to Eq. (3), and two dislocation lines come closer as well as saddles. The saddles which are located inside the interval between the vortices will meet at $x = 0$ point when $\eta = z_{R2}(2kz_{R1}-1)/\, z_{R1}(2kz_{R2}-1)$. This is the first stage of the collapse (Fig. 3a). Then saddles appear again separately, but are located now symmetrical on the *Z*-axis (Fig. 3b). The maximum distance between the saddles will be reached for $\eta \approx 0.995$ and amounts approximately to 1. In this moment the distance between vortices becomes equal to the distance between saddles. With further increase of η the saddles as well as vortices come closer. Finally, vortices and saddles collide and annihilate altogether at the point $x = 0$ (Fig. 3c).

With decreasing of η, saddle point moves toward the vortex and meets it when $\eta = \eta_0 = \exp\left[\dfrac{w_1^{\,2} - w_2^{\,2}}{2(w_1^{\,2} + w_2^{\,2})}\right]$ (this condition corresponds to the coincidence of the dislocation line to the line of equality of phase velocities of the interfering waves, as will be discussed below). In the moment of this collision a saddle-vortex point appears, which is a "pathological" topological object. After the crossing event, the saddle appears outside the dislocation line, and thus the light flow circulation around the dislocation reverses the direction.

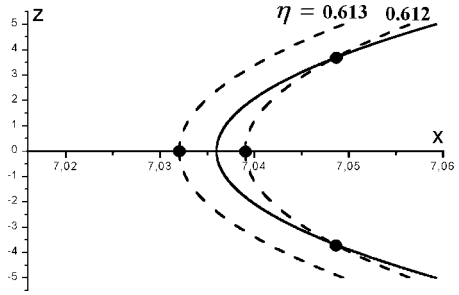

Fig. 4. Solid line: cross-section of the surface of destructive interference (π phase difference between interfering beams), for $x > 0$. Dashed line: cross-section of the surface of the amplitude equality. For $\eta > \eta_0$, there is only one possible crossing point and therefore one zero-amplitude line (edge dislocation). For $\eta < \eta_0$, there are three points of the crossing and therefore three edge dislocations. (Saddle points are not shown here).

Let us examine now how new edge dislocations can sprout from the saddle-vortex line. The cross-section of the surface of the destructive interference is shown in Fig. 4 by solid line. To find the location of edge dislocation out of the waist plane, the surface of the amplitude equality can be found also, as shown in Fig. 4 by dashed line. Its position depends on the governing

parameter η, whereas the line of the destructive interference does not depend on the amplitude ratio of the beams. This line crosses the *X*-axis exactly in the point, which corresponds to the equality of phase velocities of the interfering waves. This coincidence is hardly occasional, and can give a hint for understanding of the vortex behavior. The consequence can be made: the vortex rotation is directed *toward the area of higher phase velocity*.

Summarizing, we have found how the topological reactions of edge dislocation collapse and "unfolding" [3] occur in an interference field of two two-dimensional Gaussian beams. The results obtained are valid as well for three-dimensional beams.

The rule for determination of the optical vortex circulation direction around an edge dislocation was established: the light vortex rotates toward the region of the higher phase velocity. This rule can be used for the explanation of the natural structure of phase circulation around dark rings (circular edge dislocations) observed by Karman et al. [4]. The physical reason of this feature is not clear enough and this fundamental property of light propagation seems worthwhile for further investigations.

References

1. M.V. Vasnetsov, V.N. Gorshkov, I.G. Marienko and M.S. Soskin, Optics and Spectroscopy, 88 (2000) 260 [*Optika Spectrosk.* 88 (2000) 298 (in Russian)], see also M.S. Soskin and M.V. Vasnetsov, in: M. Vasnetsov and K. Staliunas (Eds), Optical Vortices, Nova Science Publishers, Commack, New York, 1999, pp. 23-27.
2. M. Gouy, Compt. Rendue Acad. Sci. Paris 110 (1890) 1251; A. E. Siegman, Lasers, University Science Book, Mill Valley, 1986, pp. 682-683.
3. J.F. Nye, J. Opt. Soc. Am. A **15** (1998) 1132.
4. G.P. Karman, M.W. Beijersbergen, A. van Duijl and J.P. Woerdman, Optics Letters **22** (1997) 1503; G.P. Karman and J.P. Woerdman, J. Opt. Soc. Am. A **15** (1998) 2862.

2.3. Transformations of Laguerre-Gaussian modes carrying optical vortex by a cylindrical lens and orbital angular momentum conservation

Even in free-space propagation singular beams may demonstrate some unusual properties. Single-charged optical phase singularities as morphological objects are robust with respect to perturbations. For instance, addition of a small coherent background does not destroy single-charged vortex, but only shifts its position to another place where the combined field amplitude has a zero value. For vortices with multiple charge this operation will split an initially *m*-charged vortex into $|m|$ single-charge vortices [1]. Intuition suggests that the total topological charge would be conserved in a beam propagating in free space [2,3]. On the basis of the present experimental study, we demonstrate what happens in the process of transformation of phase singularities.

The rotation of field around the vortex axis causes a nonzero value of an orbital angular momentum of a beam [4,5]. The origin of the angular momentum may be easy explained from simple consideration. As the wave front of a singular beam has helicoidal shape, the Poynting vector $S(\rho,\varphi,z)$, which is perpendicular to the wave-front surface, has the nonzero tangential component at each point. This component equals $S_\varphi(\rho,\varphi,z) = -mS/k\rho$ in the paraxial approximation. The orbital angular momentum density is $M_z(\rho,\varphi,z) = (\rho/c^2)S_\varphi(\rho,\varphi,z)$ in the *Z*-axis direction. As the Poynting vector modulus is proportional to the square of light wave amplitude, $S \propto |E_s(\rho,\varphi,z)|^2$, we may obtain the expression for $M_z(\rho,\varphi,z)$ of a singular beam in the *Z*-axis direction:

$$M_z(\rho,\varphi,z) \propto -m \left| E_s(\rho,\varphi,z) \right|^2 . \quad (1)$$

In more rigorous approach, we need to calculate a vector product to determine the angular momentum as:

$$\mathbf{M}=\varepsilon_0 \mathbf{r} \times (\mathbf{E} \times \mathbf{B}), \quad (2)$$

where ε_0 is the permittivity of free space. The relation between magnetic and electrical field components in a monochromatic electromagnetic wave is given by

$$i\omega \mathbf{B} = \nabla \times \mathbf{E} \quad (3)$$

what follows from Maxwell equations. To calculate the product in eq. (2) we shall use the full form of the field description and write

$$\mathbf{M} = \varepsilon_0 \mathbf{r} \times \left(\frac{\mathbf{E}+\mathbf{E}^*}{\mathbf{2}} \times \frac{\mathbf{B}+\mathbf{B}^*}{2}\right), \quad (4)$$

where the asterisk denotes complex conjugation.

Taking into account the non-zero z component of the field, we come to the time-averaged density of orbital angular momentum directed along Z-axis [4,5]:

$$M_z = \frac{i}{2\omega}\varepsilon_0 [x(E^* \frac{\partial E}{\partial y} - E\frac{\partial E^*}{\partial y}) - y(E^* \frac{\partial E}{\partial x} - E\frac{\partial E^*}{\partial x})] \quad (5)$$

The total orbital angular momentum L_z of the beam is an integral over the beam cross-section

$$L_z = \int_{-\infty}^{\infty}\int_{-\infty}^{\infty} M_z \, dxdy \quad (6)$$

The density of orbital angular momentum M_z of a "pure" singular beam is therefore proportional to the topological charge multiplied by beam intensity for any circularly symmetric amplitude distribution, and the total angular momentum L_z to the beam energy, as follows from eq. (5). The total orbital angular momentum L_z, as well as the beam energy is conserved in a medium without losses [4]. The orbital angular momentum of a singular beam does not depend on the frequency of light, what becomes evident if the beam energy is expressed as the product of the number of photons on the photon energy, $\hbar\omega$ [5]. For more complicated beam structure, the conservation of orbital angular momentum is not so evident.

The process of Laguerre-Gaussian mode transformation by a cylindrical-lens mode converter was considered theoretically by M.V. Beijersbergen e*t al.* [4]. It was shown that a so-called π converter reverses the sign of an axial OV, and some considerations about the transfer of an orbital angular momentum to the optical system were presented [5,6].

We present experimental results for a paraxial OV beam with topological charge m =1 passing through a single cylindrical lens. The beam was created by diffraction of a collimated Gaussian beam from He-Ne laser output on a computer- synthesized grating♦. The beam had small divergence of order of 0.3 mrad (Fig.1). Thus created OV beam was directed to a cylindrical lens.

♦ The structure of computer- synthesized grating is described in details in the Section 2.8.

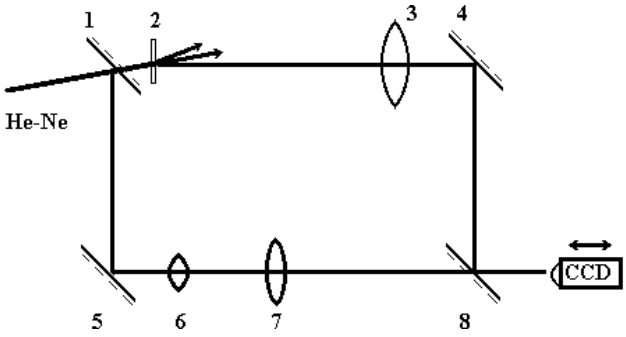

Fig.1 Experimental setup: 1 and 8 are the semitransparent mirrors; 2 is the computer-synthesized hologram; 3 is the cylindrical lens with focal length equal to 120 cm; 4 and 5 are the 100% mirrors, 6 and 7 lenses make the beam expander.

The cylindrical lens used for the experiment had the focal length F = 120 cm. Just behind the lens and before the focal plane we observed a single axial OV, which became more and more astigmatic on the path to the focal plane (Fig. 2a,b,c). The interference patterns with the additional collimated wave produced in the beam expander, shown in Fig. 1, demonstrate the same charge of the OV (Fig. 2d,e,f). The most important transformations of the focused beam occur in the focal plane and behind it.

Theoretical analysis predicts the appearance of an edge dislocation in the focal plane and crossing the axial OV with the edge dislocation. After the crossing, the sign of the OV is reversed [7].

We obtained in the experiment an astigmatic OV in the focal plane (Fig.3 a,c). Behind the focal plane we have observed three OVs, two of them possess the same sign as the initial OV (Fig.3b,d), they are shown by arrows in Fig. 3d (A and C). The central astigmatic OV has the opposite sign with respect the initial one (B in Fig. 3d). The utmost OVs run out after the focal plane to the regions of weak intensity and become non detectable.

The central OV exists in the beam to the far field. The foliation of the lateral OVs shows that they belong to a continuous dislocation line, which is not located in the focal plane, but is slightly bent. Just on the axis, this line makes the edge dislocation. In accordance with the theory, we observed the inversion of the topological charge when the axial OV intersects with the edge dislocation.

The distribution of the orbital angular momentum within the beam transforms after passing the cylindrical lens. The theoretical calculations give and important result: the total orbital angular momentum of the beam is conserved, even when the vortex reverses the sign of the charge [7,8]. This is due to the observed by us spatial rotation of the beam as whole. This unexpected conclusion shows new features of OV beams, especially important for the treatment of the photon structure and some possible applications.

As a summary, our experimental analysis of light beams carrying optical vortices has revealed the general properties of the OV beam from the point of view of conservation law of the orbital angular momentum [7]. We have studied in details the behavior of vortices in an OV beam passed through cylindrical lens. In brief, we obtained the following results:

1) At the focal plane we obtained an astigmatic OV. In our experiment we did not obtain the linear edge dislocation.
2) We detected the existence of three OVs just behind the focal plane. The utmost OVs have the same signs as initial OV and leave the beam after the focal plane for the regions of weak intensity. Central OV has opposite sign of the topological charge with respect to the initial one.
3) .Instead of the linear edge dislocation, we detected a mixed screw-edge dislocation. To explain this effect, we can take into account that the initial OV beam, created by the computer-synthesized hologram, was not a pure Laguerre-Gaussian mode [1].
4) The orbital angular momentum distribution changes in the process of beam propagation: the component associated with the helicoidal shape of the wave front has the opposite sign with respect to the part associated with the spatial rotation of a beam [9].

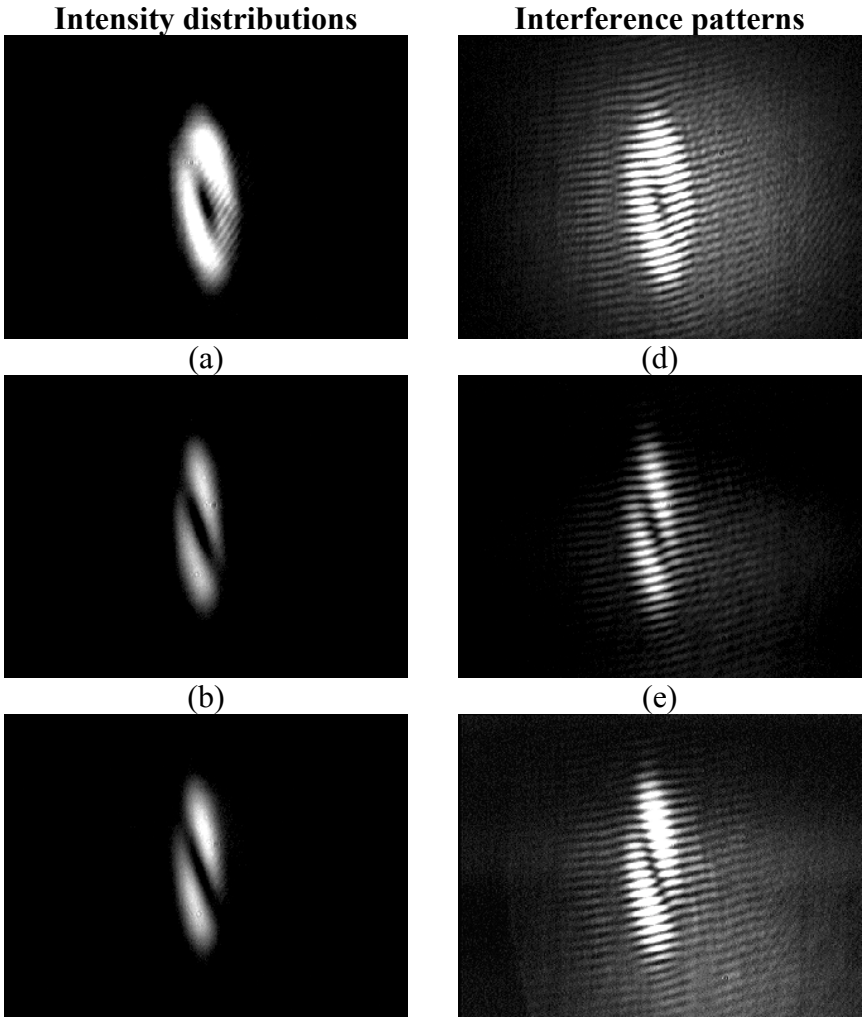

Fig.2. Intensity distributions and interference patterns for the OV beam focused by the cylindrical lens with focal length F= 120 cm at various distances D from the focal plane: (a) D= -55 cm, (b) D = - 40 cm, (c) D = -25 cm. Corresponding interference patterns (d,e,f) were obtained with the expanded Gaussian reference wave.

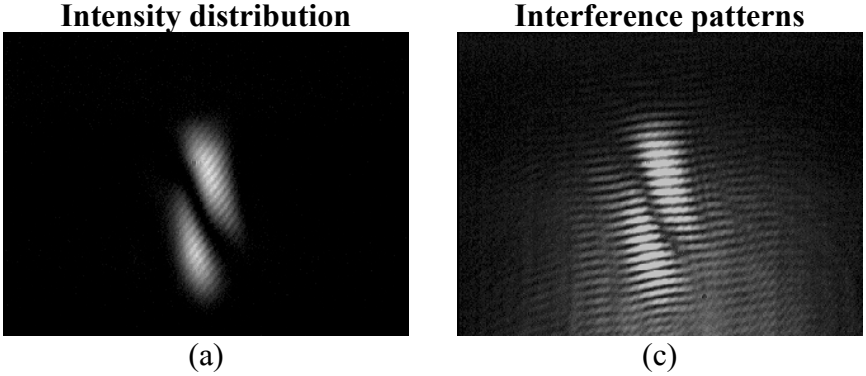

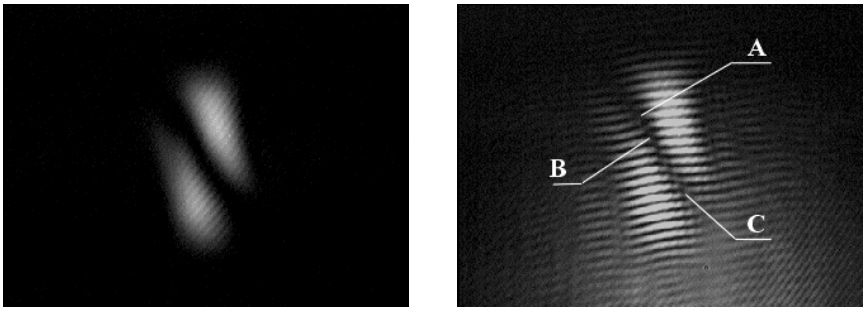

(b) (d)

Fig.3. Intensity distributions and interference patterns for the OV beam focused by the cylindrical lens with focal length F = 120 cm at the distances from the focal plane D = 0 (a,c) and D = +3 cm (b,d). Three OVs (A, B and C) are seen in (d): A and C have equal signs with respect to the initial OV, but B has the opposite sign.

REFERENCES

1. I.V. Basistiy, V.Yu. Bazhenov, M.S. Soskin and M.V. Vasnetsov, "Optics of light beams with screw dislocations", Opt. Commun. **103** 422-428 (1993).
2. J.F.Nye and M.V.Berry, "Dislocations in Wave Trains", Proc. Roy. Soc. Lond. *A* **336** 165-(1974).
3. M.V. Berry, in *Les Houches Lecture Series Session XXXV*, edited by R. Balian, M. Klaeman, and J. -P. Poirier, North-Holland, Amsterdam, 453 (1981).
4. M.W.Beijersbergen, L.AIIen, H.E.L.O. van der Ween and J.P.Woerdman, "Astigmatic Laser Mode Converters and Transfer of Orbital Angular Momentum", Opt. Commun. **96** 123-132 (1993).
5. L. Allen, M.W. Beijersbergen, R.J.C. Spreeuw and J.P.Woerdman, "Orbital Angular Momentum of Light and the Transformation of Laguerre-Gaussian laser modes", Phys. Rev. A **45** 8185-8189 (1992).
6. M. S. Soskin, V. N. Gorshkov, M.V.Vasnetsov, J.T. Malos and N.R. Heckenberg, "Topological Charge and Angular Momentum of Light Beams Carrying Optical Vortices", *Phys. Rev. A* **56** 4064-4075 (1997).
8. L. Allen, M.J.Padgett and M. Babiker, "The Orbital Angular Momentum of Light", in: Progress in Optics, ed. E. Wolf (Elsevier, Amsterdam), vol. **39** 291-372 (1999).
9. M.S.Soskin and M.V.Vasnetsov, "Singular Optics", in: Progress in Optics, ed. E. Wolf (Elsevier, Amsterdam), vol. **42**, in press.
10. A.V.Bekshaev, V.G.Denisenko, V.A.Pas'ko, M.S.Soskin and M.V.Vasnetsov, "Collision of Optical Vortices, Inversion of Topological Charge and Orbital Angular Momentum Conservation", in preparation.

2.4. Mode Separator for a Beam with an Off-Axis Optical Vortex

The goal of the work was an attempt to elaborate some experimental technique for separation of "doughnut" and "normal" photons, i.e. vortex and vortex-free components, from a combined beam with off-axial OV. The idea of the elaborated method is a use of different Gouy phase shifts for the modes with different (even and odd) modal indices [1].

The Laguerre-Gaussian (LG) modes with a nonzero azimuth coefficient l are beams with l-charged axial OV. The structure of such beams is described by the expression for the LG mode LG_p^l (in cylindrical coordinates ρ, φ, z):

$$E(LG_p^l) = E_{LG}\frac{w_0}{w}\left(\frac{\sqrt{2}\rho}{w}\right)^{|l|}\exp\left(-\frac{\rho^2}{w^2}\right)L_p^{|l|}\left(\frac{2\rho^2}{w^2}\right)\exp i\left(kz + \frac{k\rho^2}{2R(z)} + l\varphi - Q\arctan\left(\frac{z}{z_R}\right)\right), \quad (1)$$

where E_{LG} is the amplitude parameter, w_0 is the parameter of the beam size in the waist, $w = w_0\left(1 + z^2/z_R^2\right)^{1/2}$ is the mode transversal size on a distance z from the waist, $R(z) = z\left(1 + z_R^2/z^2\right)$ is the radius of curvature of a wave front in the cross-section along the beam axis, z_R is the Rayleigh range equal to $kw_0^2/2$, k is the wave number, $L_p^{|l|}$ is the associated Laguerre polynomial, l is the azimuth index, p is the radial index of the mode. For $l \neq 0$, there is an axial OV with topological charge $m = l$, because the amplitude on the beam axis is equal to zero, and the phase has azimuth dependence $\exp(il\varphi)$. The index $Q = 2p + |l| + 1$ is termed as the index of a mode. This index determines the accessory of a mode to a family of modes with identical Q. Physically, Q determines a value of a small addition to phase velocity of a mode, which is connected with the Gouy phase shift $\arctan(z/z_R)$ [2]. For the Gaussian beam (p, $l = 0$) $Q = 1$, and the additional phase shift is equal to $-\pi/2$ from the beam waist to the far field (in comparison with a plane wave). "Doughnut" mode LG_0^l ($p = 0$, $l = 1$) has the modal index $Q = 2$, and the relevant additional phase shift is equal to $-\pi$.

It happens frequently inconvenient to realize the laser generation on required LG mode in the laboratory arrangement. The simple way to create wanted beams is a diffraction of a Gaussian beam by a synthesized hologram [3]. Thus, the first- order diffracted beam has in the cross-section a point with phase singularity, i.e. OV with the necessary sign and charge. The simplest way to realize the combined beam in practice is to shift the center of the hologram, where the fringe attains the branching, relatively to the incident Gaussian beam axis.

Let us explain why this method is able to produce a combined beam. The synthesized hologram has a form of thin amplitude grating with transmission T [4]:

$$T(\rho,\varphi) = T_0 + T_1(\rho)\cos(K\rho\cos\varphi + M\varphi), \quad (2)$$

where T_0 is the average value of the hologram transmission, $T_1(\rho)$ is the contrast of fringes, $K = 2\pi/\Lambda$, where Λ is the period of the grating, M is the charge of the phase singularity. The grating with $M = \pm 1$ possesses the branching of the central fringe like a "fork". This "fork" is directed upwards for positive M, and vice versa [3]. Let us assume that the contrast of fringes $T_1(\rho)$ grows linearly with a distance from the center of the grating and becomes equal unity on radius R (we shall note, that the fringe branching point does not coincide exactly with the center of the grating, being displaced on the small quantity $M\Lambda/2\pi$ [4]). Then, the distribution of the field in a Gaussian beam ($w_0 << R$) diffracted by the grating with $M = 1$, attains just behind the grating the following form (in polar coordinates):

$$E_1 \propto \frac{\rho}{R}\exp\left(-\frac{\rho^2}{w_0^2} + i\varphi\right), \quad (3)$$

or in Cartesian coordinates

$$E_1 \propto \frac{x + iy}{R}\exp\left(-\frac{x^2 + y^2}{w_0^2}\right), \quad (4)$$

what corresponds to the LG mode LG_0^1. If the grating center is a little bit shifted relatively to the center of the readout beam, for example on the value $x_0 < R$ along the X-axis, the corresponding distribution of the field in the first order of diffraction becomes:

$$E_1 \propto \frac{x + x_0 + iy}{R} \exp(-\frac{x^2 + y^2}{w_0^2}) . \quad (5)$$

The expression (5) leads to superposition of the mode LG_0^1 carrying OV, and the mode LG_0^0 (Gaussian beam) as the "background" with the contribution proportional to the x_0. As a result, the combined beam is formed. Such simplified approach allows us to make the important conclusion that the structure of the field in the first order of diffraction can be presented as a superposition of an axial OV and a vortex-free component.

The experimental setup is shown in Fig. 1. The initial beam with single OV was obtained in the first diffraction order of the appropriate synthesized hologram (M = 1). The center of the grating was shifted relatively to the center of the incident Gaussian beam (Fig. 2a). The resulting position of the OV in the diffracted beam did not coincide with the center of the beam (Fig. 2b). Then the beam was launched into the “separator” as it is shown in the Fig. 1.

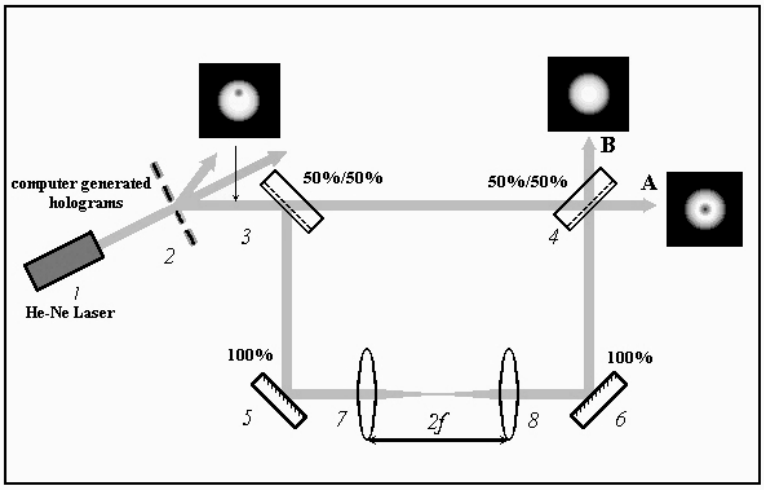

Fig. 1. Experimental setup. 1 is the He-Ne laser, 2 is the computer- synthesized hologram, 3 and 4 are identical beam splitters, 5 and 6 are 100% reflective mirrors, 7 and 8 are two confocal lenses.

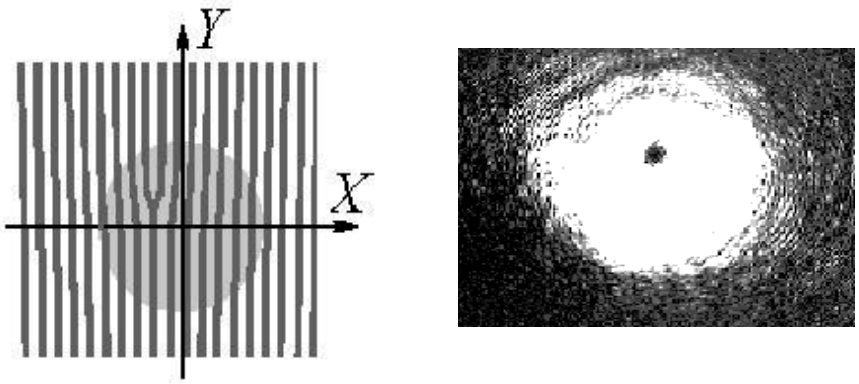

(a) (b)

Fig. 2. (a) The orientation of the incident Gaussian beam on the grating with M =1, the center of the grating does not coincide with the beam axis. (b) Cross-section view of the diffracted beam, the point of zero amplitude is shifted from the beam axis.

In one of arms of the interferometer formed by identical beam splitters 3, 4 and 100% reflective mirrors 5, 6 two confocal lenses 7 and 8 were inserted. Beam propagation between the

lenses results in the incursion of an additional phase shift due to the focusing of a beam and its subsequent expansion. The resulting phase shift equals to the doubled Gouy phase shift, and for a mode with index Q amounts $-Q\pi$. If, for example, the optical path difference between the beam propagating to channel A without reflections and the beam reflected to channel A from the second arm is equal to an even number of half-waves for a mode with even Q, the entire beam will be directed to channel A, whereas radiation in channel B will be absent due to interference quenching. For such an adjusting of the interferometer, the optical path difference for a mode with odd Q is equal to the odd number of half-waves, and the entire beam propagates through channel B.

The necessary adjusting of the interferometer was performed by reaching the maximum beam dumping in the output B for a Gaussian beam (Q = 1) entering into the separator.

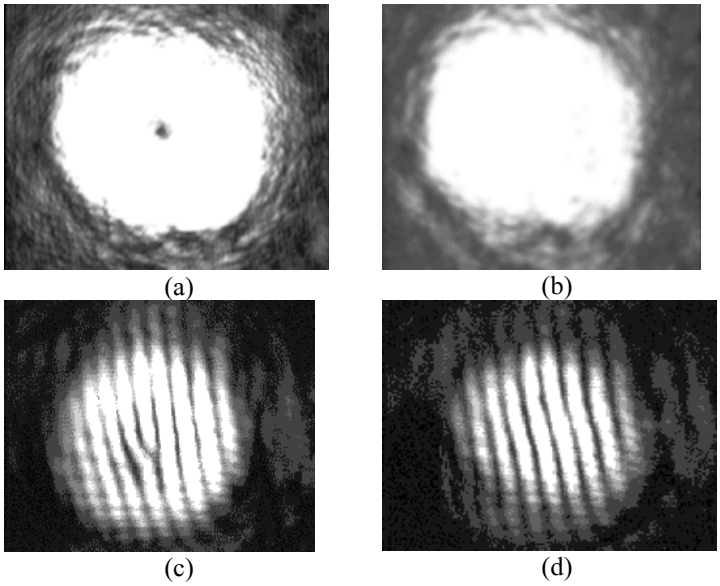

Fig.3. The intensity distributions in a cross-section view in the output A (a) and B (b). Interferograms of the beams in the output A (c) and B (d).

Because the beam with single off-axis OV can be represented as a superposition of modes with even Q (vortex component) and odd Q (vortex-free component), the separator divides vortex and vortex-free components into different output channels. We note that under reflection the sign of OV changes to the opposite, but due to even number of reflections the beam in the output A carries OV of the same sign as the initial OV beam. With the proper adjusting of the interferometer, the expected patterns were observed in the outputs A and B: axial OV in the output A and a beam with a smooth wave front in the output B (Fig. 3a,b). The beams were tested using interference with an additional plane wave (Fig. 3c,d).

It is clearly seen that by use of a pure optical method we succeeded to acieve spatial separation of photons belonging to the "doughnut" LG_0^1 mode and to the Gaussian beam (LG_0^0 mode). More general, this method is suitable for separation of modes with odd indices Q and even Q.

References

1. M. V. Vasnetsov, V.V.Slyusar, M.S.Soskin, “Mode Separator for a Beam with an off-axis Optical Vortex”, Quant. Electron. **31** 464-466 (2001).
2. M. Born and E. Wolf, *Principles of Optics,* 6nd ed. (Pergamon, N.Y.,1986).
3. V. Yu. Bazhenov, M. V. Vasnetsov, M. S. Soskin, *Sov. JETP Lett.* **52** 429-431 (1990).
4**.** I. V. Basistiy, V. Yu. Bazhenov, M. S. Soskin and M. V. Vasnetsov, “Optics of light beams with screw dislocations”, Optics Commun. **103** 422-428 (1993).

2.5. Spontaneous birth of optical vortices in a system of non-coaxial co-propagating Gaussian beams

Light beams carrying optical vortices were realized firstly in oscillation of "doughnut" LG_0^m modes in He-Ne laser with special axial cavity [1]. Nowadays, light beams with embedded OVs can be obtained easy by the help of computer-synthesized holograms which contains an interference pattern of desired OV beam and a reference beam [2]. The survey on all main devices for vortex synthesis can be found in [3]. We can consider all these methods as "induced" birth of vortices in an incident light beam with smooth wave front, typically Gaussian beam.

But is it possible to realize *spontaneous* (natural) birth of vortices due to gradual topological changes of smooth wave front during a light beam free propagation or interaction with nonlinear media? This question of principal importance for OVs understanding was answered both theoretically and experimentally.The general physical approach to solve the formulated problem is based on the consideration of combined light beams carrying optical vortices [4].

The theory of spontaneous birth of vortices in the superposition of co-propagating but non-coaxial Gaussian beams has been recently developed [5]. Here we briefly summarize the main conclusions of this theory to provide comparison with the experimental results. Theoretical treatment is based on the model reducing the stationary three-dimensional problem of propagation and interference of light beams to its two-dimensional analog, where only transversal components of a wave vector are taken into account. The paraxial propagation of Gaussian beams is described by a parabolic equation that is similar to the diffusion equation, and diffraction spreading of such beams turns out to be the function of the parameter z/z_R, where z_R is the Rayleigh range (i.e., the extent of a near-field domain). Such approach permits to find the dynamics of evolution of transversal structure of interfering beams due to diffraction. Computations show that the asymmetry of an interference field of the propagating beams plays the key role. Theory predicts (by computer modeling) the OV "dipole" nucleation due to the fully destructive interference and wave front disruptuion on some distance behind the common waist plane.

To verify the theoretical predictions, we have realized the system of two mutually coherent co-propagating Gaussian beams [6]. The experiment was performed in the scheme of a twin Mach-Zander interferometer (Fig.1). He-Ne laser (λ = 0.6328 μm, P = 40 mW) was the source of the initial Gaussian beam. The outer interferometer (*BS1, M1, M4, BS4*) provides observation of an interference pattern originating under superposition of the vortex-bearing field and expanded (by *BE*) off-axis plane reference wave. The rotation of *BS4* around the *X*-axis on the angle α permited to adjust the period of interference patterns. The inner interferometer (*BS2, M2, BS3*, and *M3*) creates two co-propagating beams which overlap in the near field. Both beams after the beamsplitter *BS2* undergo spatial filtering by the microscopic lenses and pinholes. In our experiment, the pinhole *PH1* was 10 μm in diameter, and the pinhole *PH2* was 30 μm in diameter. The lenses *L1* (focal length f_1 = 35 mm) and *L2* (focal length f_2 = 50 mm) transform diverging beams into converging ones with the waists located at the common plane *PW*. The difference of the focal lengths of the lenses *L1* and *L2* and their distances from the corresponding pinholes (d_1 = 37 mm, d_2 = 65 mm) was used to form two coaxial beams with different waist radii. Displacement of the mirror *M3* along *Y*-axis permits to shift the second beam axis at any distance Δy. For that, the beams leave to be co-propagating.

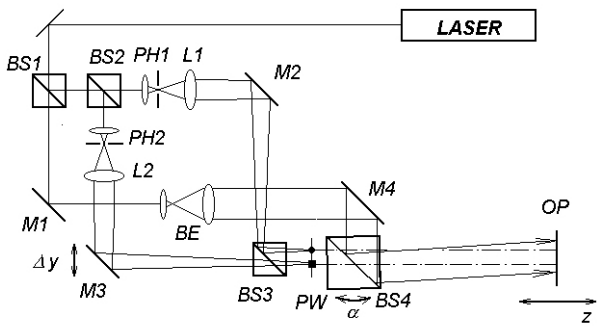

Fig.1. Experimental arrangement for the observation of interference between two co-propagating but non-coaxial Gaussian beams: *BS* are beam splitters, *M1-4* are the mirrors, *PH1,2* are the pinholes, *BE* is the beam expander, *L1,2* are the lenses, *PW* is the common waist plane, *OP* is the observation plane where CCD camera was placed.

The measured spatial intensity distributions at the waist plane for the each of two beams and at the plane distanced from the waist plane by z = 80 mm are shown in Fig.2a and Fig.2b, respectively.

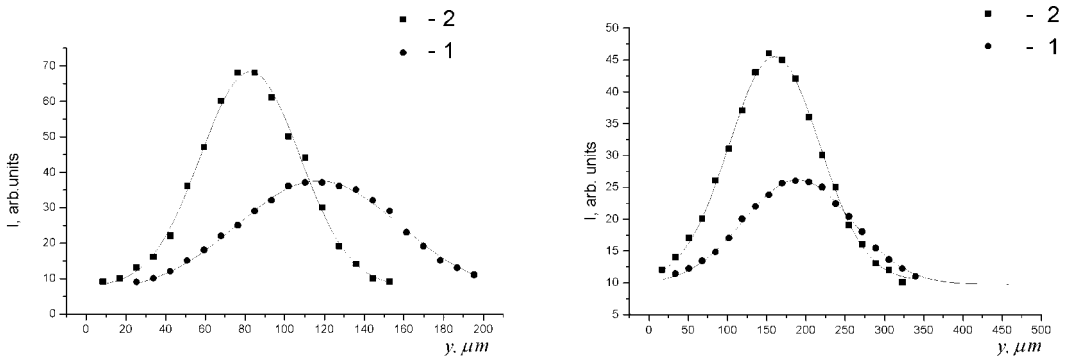

(a) (b)

Fig. 2. . Intensity distributions for two overlapping co-propagating Gaussian beams (• - beam 1, ■ - beam 2): (a) at the common waist plane (r_{02} / r_{01} = 0.6, Δy = 0.4 r_{01}); (b) the same at the plane distanced from the waist plane by z = 9.7 z_{R1}.

Experimental data were fitted by Gaussian envelope with good agreement. The waist radii measured on the level e^{-2} of the central intensity distribution maxima were r_{01} =83 ± 2 μm and r_{02} = 0.6 r_{01} = 50 ± 2 μm, respectively. The transversal beam displacement amounted to Δy = 0.4 r_{01}. The beam radii measured at the level e^{-2} of the central intensity distribution maxima at the distance z = 80 mm were r_1 =139 ± 2 μm and r_2 =115 ± 2 μm respectively.

Using the measured r_{01} and r_{02} values, we calculated the corresponding Rayleigh ranges: z_{R1} = 35±2 mm, and z_{R2} = 0.36 z_{R2} = 12.5 ±1 mm. The divergence of the beams was measured to be θ_1 = 2.4 mrad and θ_2 = 4 mrad, respectively. The intensity maxima at the plane z = 80 mm were distanced by Δy = 0.4r_{01} = 34±5 μm.

It would be of interest to observe in experiment the OVs trajectory and their disappearance. For this purpose, we obtain the set of interference patterns between the combined beam consisting from two Gaussian beams and a tilted plane reference wave at various distances z from the waist plane (Fig. 3).

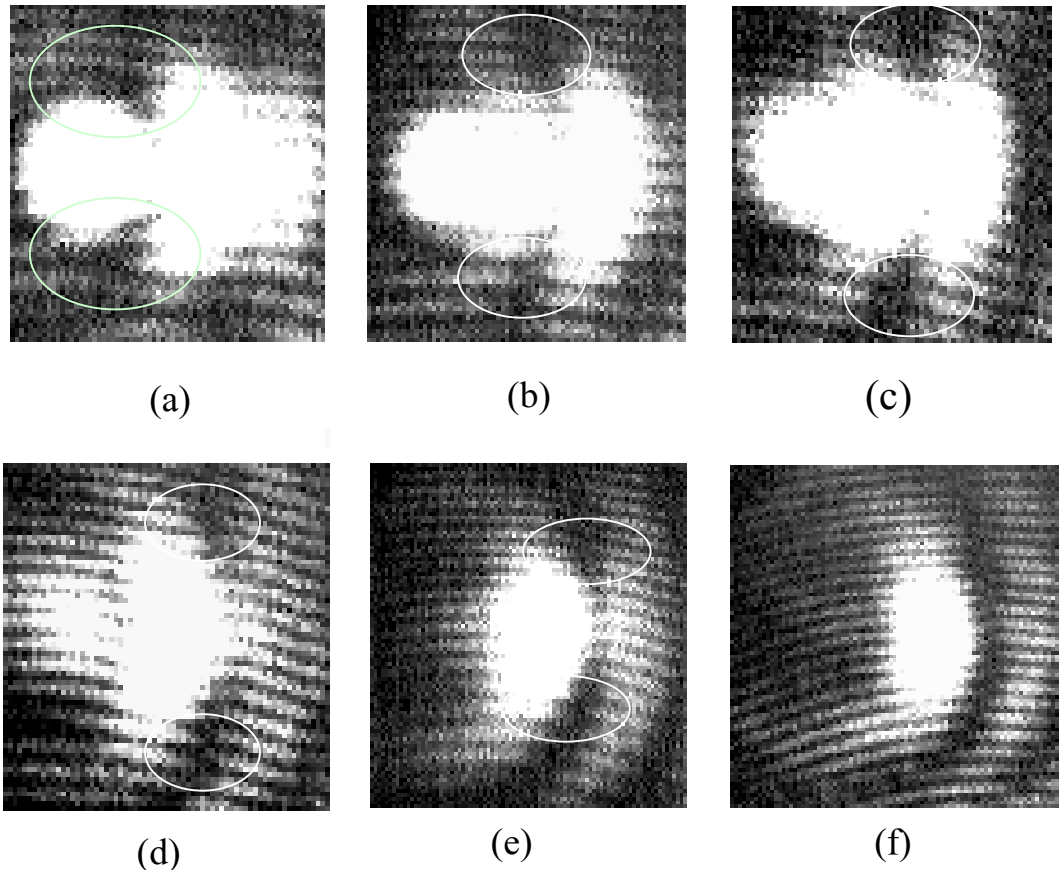

Fig. 3. Interference between the combined beam and tilted reference wave, at various distances: $z = 0.29 L_{R1}$ (*a*), $z = 0.58 L_{R1}$ (b), $z = 1.16 L_{R1}$ (*c*), $z = 2.32 L_{R1}$ (*d*), $z = 4.08 L_{R1}$ (e), $z = 5.8 L_{R1}$ (f). Ellipses show the forks visualizing the OVs.

It is seen in Fig. 3 that the vortex dipole is born already at the near field (fragment (a)), for $z = 0.29 L_{R1}$ and exists over rather large range of distances (up to $z = 4.08 L_{R1}$ at fragment (e)). The pictures shown in Fig.3 are obtained with step-by-step change of the scale, in correspondence with diffraction spread-out of the Gaussian beams. As the distance z increases, the vortices become more anisotropic. At some distance (in our experiment, $z = 5.8 L_{R1}$) the vortex dipole is converted into the structure (Fig.3f), which reminds circular edge dislocation. In the calculations, vortices annihilate and do not exist in the far field.

To the conclusion, we have shown both theoretically and experimentally the possibility of spontaneous (natural) birth of optical vortices in the system of two-co-propagating in free space non-coaxial Gaussian beams with different parameters.

References

1. M. Harris, C. A. Hill and J. M. Vaughan, “Optical helices and spiral interference fringes”, Opt. Commun. **106** 161-166 (1994).
2. V. Yu. Bazhenov, M.V. Vasnetsov and M. S. Soskin,”Laser beams with screw dislocations of wave front”, Sov JETP Lett. **52** 429-431 (1990).
3. M. Soskin and M. Vasnetsov, “Singular optics as a new chapter of modern photonics: optical vortices fundamentals and applications”, Photonics Sci. News **4**, issue 4, 21 – 42 (1999).
4. M. S. Soskin, V. N. Gorshkov, M. V. Vasnetsov, J. T. Malos and N. R. Heckenberg, “Topological charge and angular momentum of light beams carrying optical vortices”, Phys. Rev. A **56** 4064- 4075 (1997).

5. V. N. Gorshkov, A. N. Kononenko, M. S. Soskin, “Topology of optical vortices spontaneous birth”, Int. Conf. in Correlation Optics 2001 (Chernivtsy, Ukraine, May 2001), Proc. of SPIE (in press).
6. M. S. Soskin, G. V. Bogatiryova, and V. Gorshkov, “Spontaneous birth of optical vortices in a system of non-coaxial co-propagating Gaussian beams”, Int. Conf. in Correlation Optics 2001 (Chernivtsy, Ukraine, May 2001), Proc. of SPIE (in press).

2.6. Launching of an Optical Vortex Beam into a Leaky Planar Waveguide

Common experiments with plane reference wave, which are good enough to demonstrate the helicity of an OV beam wavefront [1,2], can not give high resolution for an accurate inspection of the details such as Poynting vector orientation.

The goal of this communication is to report the first to our knowledge experimental approach to the direct test of the OV beam structure with a use of a prism-film coupler [3]. This simple kind of an interferometric device was shown to be a very sensitive optical tool [4]. The reason is the multiple-beam interference within a planar waveguide, producing high angular resolution, which allows us to use it for the search of inner structure of a light current within a beam possessing optical vortex.

The schematic in Fig. 1 shows a leaky-wave coupler using two prism substrates and am immersion liquid between them. The necessary condition for the liquid refractive index to be less than the substrate index is easily realized. Also, it makes no experimental difficulties to achieve parallel surfaces of the film with a thickness of several wavelengths. The operation in the reflection-beam detection can resolve a narrow range of incident angles within an optical beam with diffraction-limited divergence, as the following analysis shows.

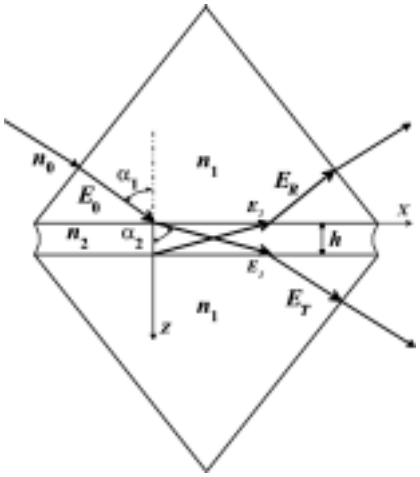

Figure 1. Sketch of the waves in a leaky-waveguide device: E_0 is the incident plane wave, E_R is the reflected wave, E_T is the transmitted wave. Two waves E_1 and E_2 exist within the liquid film of the thickness h and refractive index n_2 between the prisms with refractive index n_1. X-axis is parallel to the film, Y-axis is perpendicular to the plane of incidence, Z-axis is directed inside the film.

For TE polarized plane wave with amplitude E_0 incident to a waveguide liquid film with refractive index n_2, located between two identical substrates of refractive index n_1, the boundary conditions on the first surface of a film ($z = 0$) will look as follows:

$$E_0 + E_R = E_1 + E_2,$$
$$E_0 - E_R = \frac{n_2 \cos\alpha_2}{n_1 \cos\alpha_1}\left(E_1 - E_2\right), \qquad (1)$$

where E_1 and E_2 are the amplitudes of waves within the film, E_R is the amplitude of the reflected wave, α_1 and α_2 are the angles of incidence and refraction, as indicated in Fig. 1.

On the other surface ($z = h$) the boundary conditions are

$$E_1 \exp(ikhn_2 \cos\alpha_2) + E_2 \exp(-ikhn_2 \cos\alpha_2) = E_T \exp(ikhn_1 \cos\alpha_1),$$
$$E_1 \exp(ikhn_2 \cos\alpha_2) - E_2 \exp(-ikhn_2 \cos\alpha_2) = \frac{n_1 \cos\alpha_1}{n_2 \cos\alpha_2} E_T \exp(ikhn_1 \cos\alpha_1), \quad (2)$$

where k is the vavenumber (in vacuum), E_T is the amplitude of the transmitted wave. The Snell low relates the angles α_1 and α_2: $n_1 \sin\alpha_1 = n_2 \sin\alpha_2$.

Calculation of the reflection coefficient $R = |E_R/E_0|^2$ leads to the result

$$R = \frac{\sin^2(khn_2 \cos\alpha_2)}{\sin^2(khn_2 \cos\alpha_2) + 4\beta^2}, \quad (3)$$

where

$$\beta = \frac{n_1 n_2 \cos\alpha_1 \cos\alpha_2}{n_1^2 - n_2^2}. \quad `(4)$$

Evidently, the transmission coefficient $T = 1- R$. The smaller β, the sharper is the resonance peak in transmission and the gap in reflection, which correspond to the leaky mode excitation. The half-width of the gap can be estimated to be $\Delta\alpha_1 = 2\beta$.

The resulting reflection coefficient (intensity) is shown in Fig. 2 as function of the angle of incidence α_1. It is important that in the reflected wave the condition of a leaky mode excitation corresponds to a zero intensity. Therefore, for an ordinary divergent beam (Gaussion laser mode, for example) a narrow dark line in the reflected beam cross-section, oriented perpendicularly to the plane of incidence, will appear and will be observable in the near field as well as in the far field. Diffraction spread-out is not able to wash out the zero-intensity line across the beam due to the difference in phase on π occurring between the beam sides divided by the dark line. This feature is very important, as it gives a sharp notch on a beam, irrespectively to the width of the gap in the reflection function.

The dark line in the reflected beam visualize a narrow range of angles of incidence within a beam, corresponding to the effective leaky mode excitation. Having in hands this sensitive instrument, we can apply it for the analysis of inner structure of a helicoidal-wavefront optical beam, or a beam possessing axial optical vortex [2].

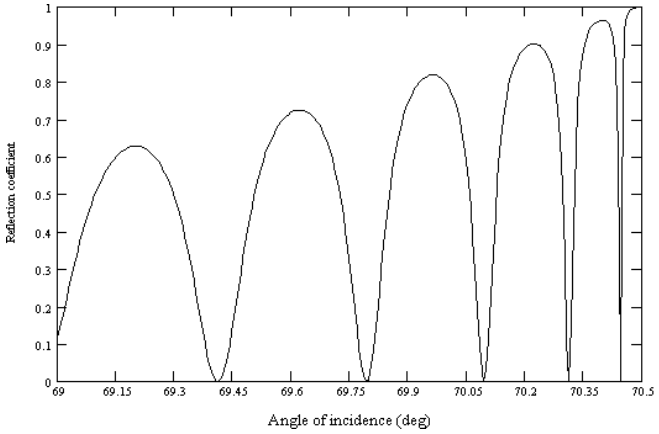

Fig. 2. Calculated angular dependence of the reflection from a leaky waveguide (glass/glicerine/glass). The angle 70.5º corresponds to the total internal reflection.

To analize the shape of helicoidal wave front inside the angle of diffraction limit the "ray" model of OV beam was used. Figure 3 represents a calculation of the line being a cross-section of the ray family which have in *YZ* plane zero inclination with respect to the beam axis ($\delta = 0$). All these rays will excite a waveguide mode, what can be detected as in the transmitted beam, as in the reflected beam. Observation of the dark line in the reflected beam will give therefore a visual picture of the loci of rays with equal angle of incidence in the *YZ* plane.

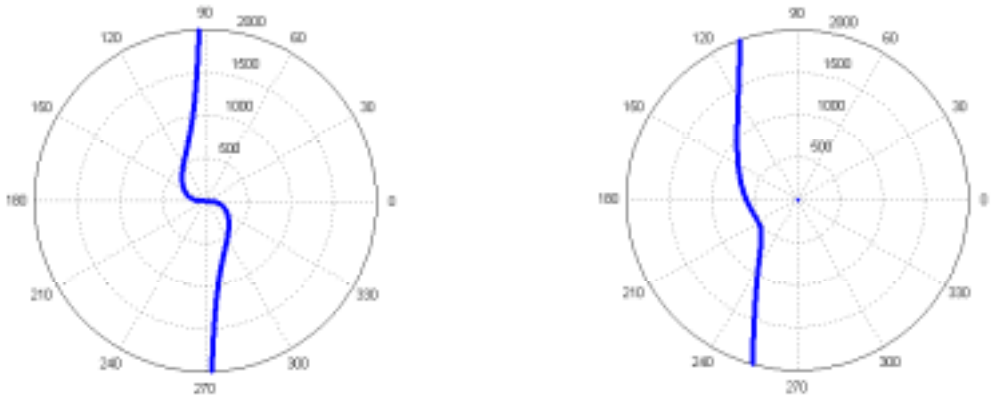

(a) (b)

Fig. 3. Calculation of the cross-section of the loci of ray family with zero inclination with respect to the beam axis, in the plane of incidence. In calculations, we let $k = 10\ \mu m^{-1}$, $R = 1.5 \cdot 10^6\ \mu m$, the radial scale is given in micrometers and the azimuth scale in degrees. For zero detuning ($\delta = 0$) all these rays will excite a propagating leaky mode in the waveguide, thus producing a dark line in the reflected beam (a). (b)The shape of the dark line in the reflected beam for constant ray inclination with respect to the beam axis, which compensates the beam angular detuning $\delta = -4 \cdot 10^{-4}$.

The shape of the line strongly depends on the wave-front curvature and the detuning δ. Non-zero detuning shifts the dark line from the beam axis. The smaller is the spherical component of the curvature, the sharper is the influence of the helical componentgives an For example, at $R = \infty$, and $\delta = 5 \cdot 10^{-5}$: the line turns now to a closed loop. This situation corresponds to the focused laser beam, when the incident beam enters the waveguide just in the waist. For another sign of the detuning, the loop will appear in the upper half plane. Zero detuning in this case corresponds to the horizontal line through the beam centre.

Two identical 60° glass prisms with refractive index $n_1 = 1.515$ were used to compose a leaky-mode waveguide. A drop of glycerine ($n_2 = 1.43$) placed between prisms produced a parallel film after the stressing the prism faces. The thickness of the layer was estimated to be about

The quality of just obtained waveguide was tested with an expanded (divergent) laser beam (Gaussian mode) from He-Ne laser. A set of vertical narrow dark lines appears in the reflected beam. With non-expanded beam from the laser output, the resonance conditon of leaky mode excitation can be detected by observation of one dark line crossing the beam (Fig. 4a).

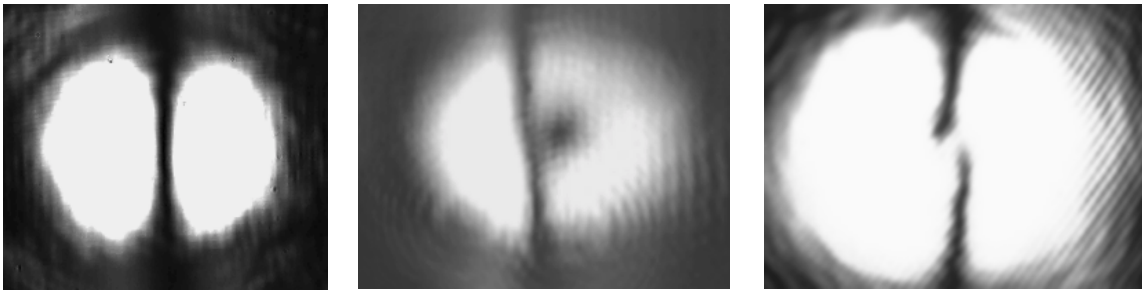

(a) (b) (c)

Fig. 4. Dark line crossing the Gaussian beam reflected from the leaky waveguide, zero angular detuning (a), the same for an incident OV beam, non-zero detuning (b), zero detuning (c).

To create an OV beam, we used a usual technique of laser beam (TEM mode from HeNe laser) diffraction by a computer-synthesized hologram [2].

The divergence of the OV beam obtained in the first order of diffraction (m = 1) was measured to be about 2º. The OV beam was directed to the prism-film coupler, which was mounted in a table rotating with high precision.

In order to verify in one experimental scheme the predictions of the theoretical analysis both for convergent and divergent beams, we used a lens with focal length 30 cm and gradually move the prism coupler before and behind the focal plane.

The images of the reflected beam taken by CCD camera are shown in Fig. 4b,c. The angle of incidence was chosen to observe the first mode resonance in the reflected beam. For non-zero angular detuning, there is a slightly bent dark line crossing the beam, in accordance with the geometrical optics analysis (Fig. 4b).

There is noticeable deviation from the expectation folloing from the geometrical optics description in the case of zero detuning. Just in the vicinity of the OV axis we have detected a tear of the dark line and disappearence of the central zero-intensity point which is the OV core (Fig. 4c), instead of the calculated continuous dark line crossing the OV core (Fig.3).

As a summary, the used leaky-mode waveguide was shown to be very sensitive instrument for a detail investigation of the structure of an OV beam with diffraction-limited divergence. The reason is the multiple-beam interference within a liquid film, producing high angular resolution, especially for low-order modes (the quality of the wavegide is higher for them due to the higher reflection on the boundaries).

References

1. J.M. Vaughan and D.V.Willetts, Optics Commun. 30 (1979) 263.
2. Optical Vortices, M. Vasnetsov and K. Staliunas eds, Nova Science Publishers, NY, 1999.
3. R. Ulrich and W. Prettl, Appl. Phys. 1, 55 (1973).
4. R. Th. Kersten, Optica Acta 22, 503-513 (1975).

2.8 Second harmonic generation of OV beams with fractional topological charge

We have shown that there is a possibility to create optical beams which possess optical vortices with fractional topological charge by a holographic technique [1]. Now we report an elaborated technique and the experimental results. We also discuss some nontrivial effects of second-harmonic generation (SHG) of OV beams with fractional topological charges.

One of the most important properties of an optical vortex is the circulation of phase around its axis, in the form [2]

$$\Phi(z = const) = m\varphi, \qquad (1)$$

where φ is the azimuth angle and m is the topological charge of an OV. This transversal phase structure is responsible for the specific interference pattern produced with an ordinary tilted reference wave (Fig.1a). Instead of a usual periodic fringes, the splitting of one fringe appears into m new fringes [3]. The interference with a coaxial plane reference wave produces spiral fringes, as shown in Fig.1b.

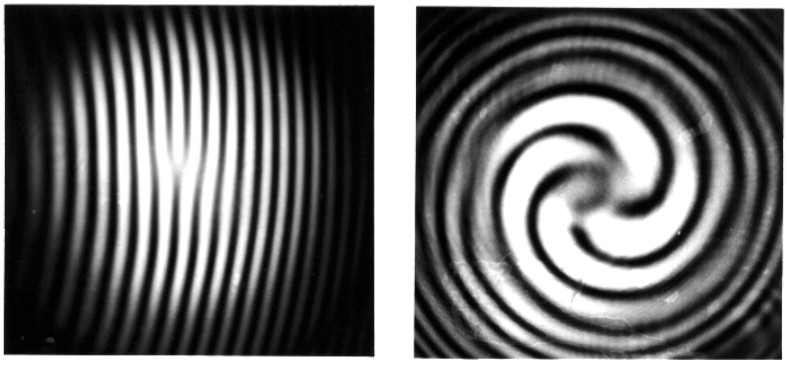

Fig. 1. Pattern of interference between charge 1 OV beam and tilted plane reference wave (a) and between charge 4 OV beam and coaxial plane reference wave (b).

The idea of OV beam formation by use of diffraction of an ordinary wave on a computer-generated grating is based on the holographic principle: a readout beam restores the wave, which participated in the hologram recording. Instead of writing a hologram with two actual optical waves, it is enough to calculate the interference pattern numerically and print the picture in black and white or gray scale. Then the picture after reduction of the transverse dimensions serves as an amplitude grating producing OV beams in diffraction orders [4]. Examples of binary gratings are shown in Fig. 2.

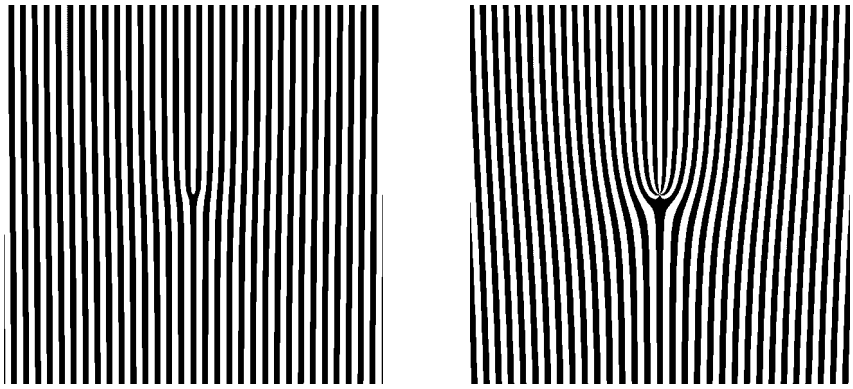

(a) (b)

Fig. 2. The computer-generated patterns for gratings which are able to produce in the first diffraction order OV beams with topological charges m =1 (a) and m = 5 (b).

The holographic principle can be applied also for the production of more complicated beams with specific features. For the task of OV beams with fractional topological charge creation, it is necessary to calculate the interference pattern which corresponds to the phase dependence, according to Eq.(1), with the fractional charge m. An example of a binary grating for m = ½ is shown in Fig. 3a [1]. A half-cut of the fringes appears along a line $\varphi = 0$, due to the phase step on π on this line. However, this method is not unique. We propose now more interesting technique, which is based on the production of subharmonic diffraction orders. Let us suppose that the grating function has the form

$$T(\rho,\varphi) = T_0\left[a_0 + a_1\cos\left(\rho\cos\varphi + \varphi + \varphi_0\right) + a_2\cos\left(\frac{\rho\cos\varphi + \varphi + \varphi_0}{2}\right)\right]. \qquad (2)$$

With the condition

$$a_0 = a_1 + \frac{a_2^2}{8a_1}, \qquad (3)$$

formula (2) gives minimum transmission $T_{min} = 0$, and periodically alterating maximum transmission between $T_{max1} = T_0(a_0 + a_1 + a_2)$ and $T_{max2} = T_0(a_0 + a_1 - a_2)$. The structure of the

transmission function is shown in Fig. 3. The choice of $\varphi_0 = 3\pi/2$ permits to obtain a symmetric function. Figure 3 shows the transmission function.

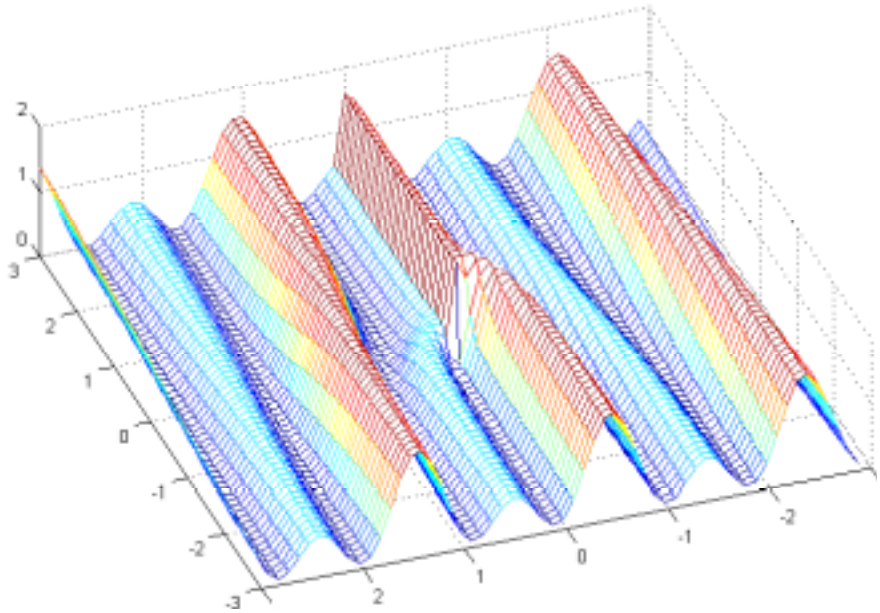

Fig. 3. Mesh of the transmission function of a grating with m = ½ subharmonic, according to Eq.(2).

The diffraction by the grating with modulated contrast will produce, except ±1 diffraction orders, which corresponds to the fundamental period, a pair of subharmonic orders, which will be spatially located on the bisectrix between the ±1 diffraction orders. In a similar way we can construct gratings which can produce any necessary fractional charge of an OV.
The rectangular-profile pattern for a computer-generated diffraction grating was calculated on the basis of the transmission function

$$T(\rho,\varphi)=\begin{cases} 1, & \cos\left(\varphi+\dfrac{2\pi}{\Lambda}\rho\cos(\varphi)\right)<0 \\ 0.5, & \cos\left(\dfrac{1}{n}\left(\varphi_0+\dfrac{2\pi}{\Lambda}\rho\cos(\varphi)\right)\right)<\cos\left(\dfrac{\pi}{n}\right) \ \ and \ \ \cos\left(\varphi+\dfrac{2\pi}{\Lambda}\rho\cos(\varphi)\right)>0, \\ 0, & \cos\left(\dfrac{1}{n}\left(\varphi_0+\dfrac{2\pi}{\Lambda}\rho\cos(\varphi)\right)\right)>\cos\left(\dfrac{\pi}{n}\right) \ \ and \ \ \cos\left(\varphi+\dfrac{2\pi}{\Lambda}\rho\cos(\varphi)\right)>0, \end{cases} \quad (4)$$

where $\varphi_0=\begin{cases}\varphi-2\pi, & \varphi>\pi \\ \varphi, & \varphi<\pi\end{cases}$, integer $n = 1/m$, Λ is the grating spacing.

The example for a grating pattern with n = 2 (m = ½) is shown in Fig.4c.

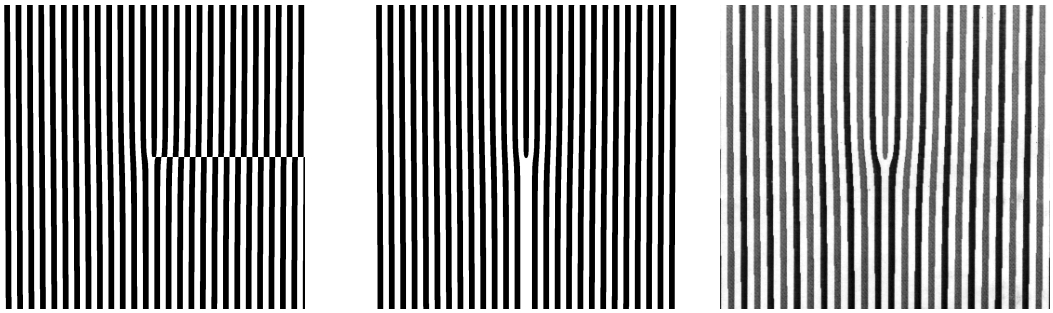

(a) (b) (c)

Fig.4. Three examples of computer-generated gratings, suitable for the production of OV beams with fractional topological charge $m = ½$. (a) Binary grating with a half-cut of fringes along a horizontal line; (b) Binary grating with a half-cut along a vertical line; (c) Grating with periodically modulated contrast

The proposed techniqe is easily applied for the creation of any subharmonic beams with fractional charges $m = 1/n$, $2/n$, $..(n\text{-}1)/n$.. Figure 5 represents the diffraction orders for the computer-synthesized grating shown in Fig. 4b. A half-cut oriented roughly vertically appears in the subharmonic beam just behind the grating, and then gradually transforms to a single OV in the far field. Subharmonic beam with the topological charge 3/2 has more complicated structure in the near field, and possesses two isolated OVs in the far field.

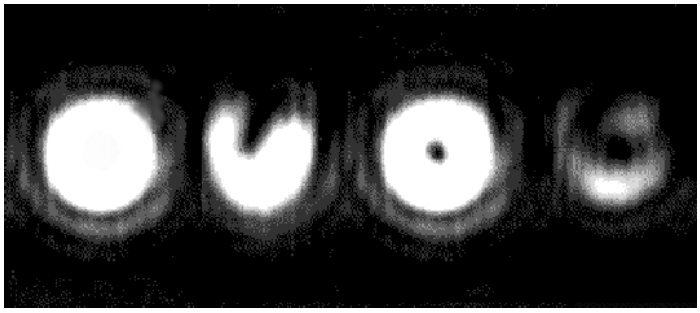

Fig. 5. Diffraction orders in the near field, from left to the right: zero, subharmonic1/2, first, subharmonic 3/2.

Figure 6 shows the diffraction orders for the grating produced to create 1/3 subharmonic, as well as 2/3 subharmonic beams. In the far field both subharmonics (1/3 and 2/3) have one single-charged OV.

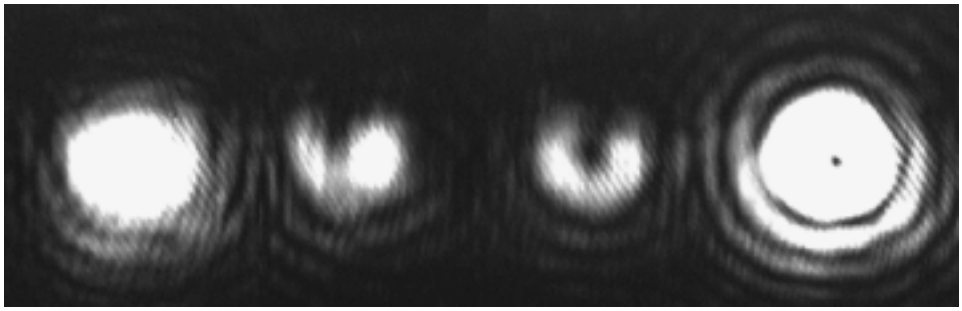

Fig. 6. Diffraction orders, from left to right: zero, subharmonic1/3, subharmonic 2/3, first.

Both gratings (shown in Figs 5 and 6) give a single-charged axial OV in the first fundamental order, which remains the same up to the far field.

As it was established earlier, OV beams with fractional topological charges are not stable along the propagation path, in contrast to an axial charge 1 vortex (e.g. Laguerre-Gaussian mode LG^{l}_{0}). A decomposition of the diffracted beam to the set of LG modes shows an immidiate decay of the initial half-cut of the wave front to an infinite set of individual vortices, which gradually leabe the beam along its propagation path. In the far field, the number of vortices is equal to mod(m).

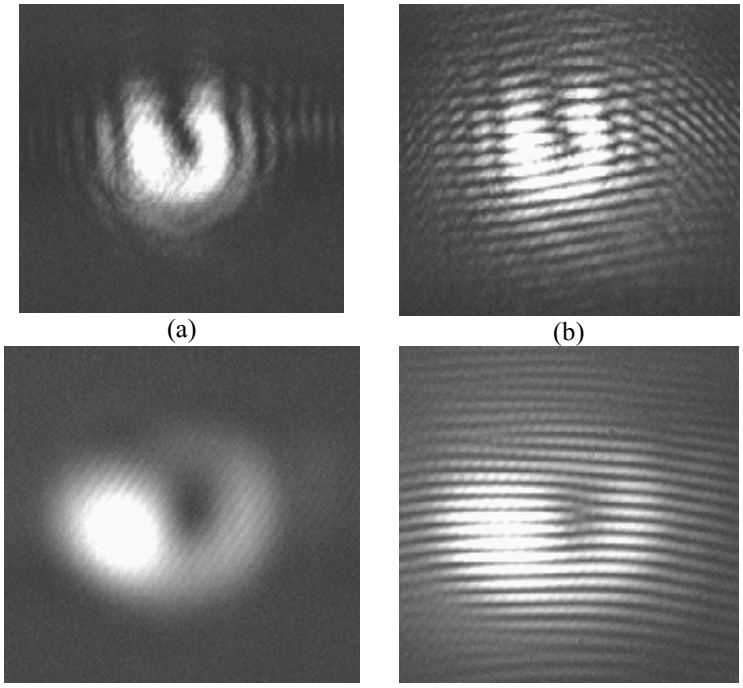

Fig.7. Evolution of an OV beam with fractional charge 1/2 in the near field. (a) The ½ subharmonic diffraction order on a distance 16 cm from the grating and (b) the corresponding interferogram. The vertical dark line crosses the beam, there is a phase step seen in the interferogram. Individual vortices are not resolved. (c) The diffracted beam on the distance 100 cm from the grating. The central isolated vortex is seen, several peripheral vortices can be also found in the interference pattern (d).

With respect to the process of second-harmonic generation (SHG) with OV beams, an interesting optical paradox appears. The phase doubling, which occurs in the SHG and leads to the doubling of the topological charge of the OV [1,5], will create a single-charged OV from the fractional charge ½ in the fundamental frequency (FF) beam. From the other hand, if the nonlinear frequency-doubling element will be located far enough from the grating, the incident beam will contain a single off-axis OV, and two off-axis OVs are expected to appear in the SH beam [1,5]. In the intermediate situation, a set of vortices existing in the FF beam will produce a doubled set of OVs in the SH beam. The evolution of this set of OVs will take place in the SH beam, and the result is not evident in advance.

References

1. I.V.Basistiy, M.S.Soskin, M.V.Vasnetsov, “Optical wavefront dislocations and their properties”, Opt. Commun. **119** 604-612 (1995)
2. M. Vasnetsov and K. Staliunas (Eds), Optical Vortices, Nova Science Publishers, Commack, New York, 1999.
3. I.V.Basistiy, V.Yu.Bazhenov, M.S.Soskin and M.V.Vasnetsov, “Optics of light beams with screw dislocations”, Opt. Commun. **103** 422-428 (1993)
4. V. Yu. Bazhenov, M. V. Vasnetsov, M. S. Soskin, “Laser beams with screw dislocations of wave front”, Sov. JETP Lett**. 52** 429-431 (1990).
5. M.S.Soskin and M.V.Vasnetsov, “Nonlinear singular optics”, Pure & Appl. Optics **7** 301-311 (1998).

Chapter 3
Multichannel Optical Manipulator Based on OV Beam

3.1 Introduction

The physical background of manipulations (translation, rotation, arrangement, etc.) by OVs with captured micron-size particles is considered. Manipulation of biological objects allows to carry out biological reactions between selected components or to accelerate natural reactions by means of closing reacting components.

In 1974 Ashkin and Dziedzic [1] showed that TEM^{*}_{01} "doughnut" laser mode could be used to levitate various types of spheres. They described levitation of hollow transparent and metallic spheres and also solid transparent spheres. Solid transparent spheres levitated within a single vertically upward propagating doughnut beam while hollow transparent and metallic spheres was levitating under action of a combination of two counter-propagating beams and one vertically upward beam. Physical base of optical trapping arises from Lebedev's work on measurement of radiation pressure in 1901. Firstly, a particle exchanges the momentum with the light field. Next, the local flow of momentum is configured in such a way so that an equilibrium point exists. The mechanism of particle trapping with single OV was studied by Heckenberg and collaborators in detail [2].

3.2 Computer simulation of the multichannel optical manipulator

Contrasting to the aforeciting researches on controlled 3D and 2D trapping, we propose the theoretical base for trapping of two microparticles (or group of them) with a possibility of simultaneous manipulation of them. All manipulations are possible in each cross-section plane of the beam.

We constructed the beam with two embedded OVs of opposite signs (OV "dipole" OVD) disposed on some distance from the beam centre [3]. Such beam can be produced easy by superposing of several HG modes or the combination of the HG and the LG modes with a necessary phase shift. The following mode composition can be used:

$$LG_0^1 + 2i\,HG_0^1 + HG_0^0\,e^{i\psi} \Leftrightarrow \text{'Vortices Dipole'}, \qquad (1)$$

where ψ is the phase parameter, introduced to control the OVD size. The distribution of the intensity in the cross-section of OVD is depicted in Fig. 1. Each dark spot is the OV core. Microparticles within the OV cores happen to be captured radially. Thus, we have a two-channel trap. Each OV in OVD has the local intensity and phase structure near the OV axis similar to a single OV.

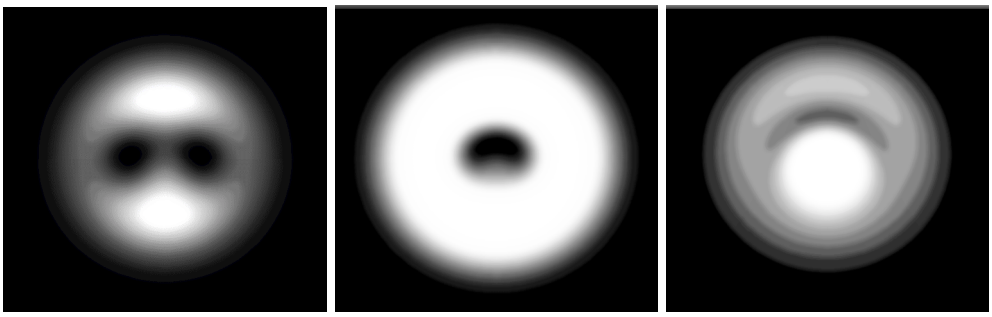

(a) **(b)** **(c)**

Fig. 1. Intensity distribution in the cross-section of the Gaussian beam with embedded OVD: (a) the initial state, (b) close to the annihilation state and (c) after the annihilation.

The ability of OVD to change the size and finally to annihilate under incursion of some phase shift of the HG_{00} mode is the base of the multichannel OV manipulator. We use the phase shift ψ to control the OVD size. Figure 2 presents the OVD size vs phase shift. In experiment the phase variation can be easily controlled.

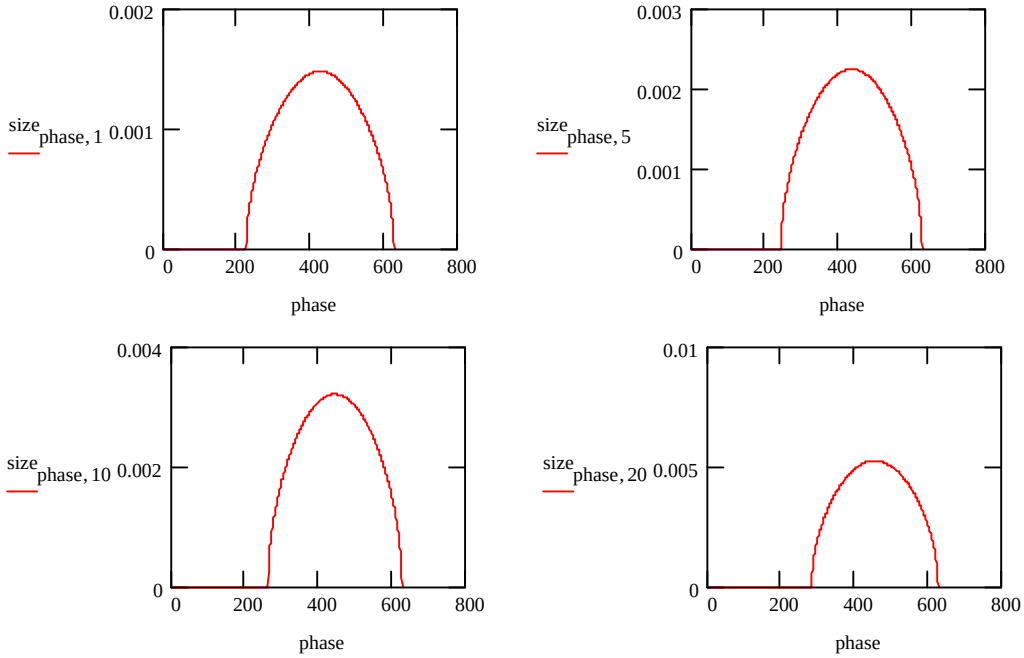

Fig. 2. OVD size vs phase shift ψ: (a) one Rayleigh distance from the waist; (b) 5 Rayleigh distances, (c) 10 Rayleigh distances, (d) 20 Rayleigh distances. The phase scale (horizontal axis) is measured in radians, multiplied by 100. Vertical axis: the OVD size is presented in units normalized on the current transversal size of the Gaussian beam.

Next our step is the tree-channel manipulator. It bases on the following principle, with only two LG modes used to compose the manipulator (all three vortices have the same sign):

$$LG_0^3 + A\,LG_0^0 \exp(i\psi) \Leftrightarrow \text{‘Three-channel manipulator’}, \qquad (2)$$

where A and ψ are the control parameters. As for the case of two-channel manipulator, we introduce here the phase ψ in Gaussian LG_0^0 mode. Besides, a new control parameter A appears, which is responsible for the distancing of all channels radially. The larger is A, the larger is the distance of the OV from the centre of the beam. When A equals to zero, the channels are not separated.

Unlike previous case of two-channel OVD system, ψ is the azimuth parameter responsible for the rotation of all channels. The increasing ψ to 2π results in the one full turn of the whole system of channels. Decreasing of ψ leads to the pattern rotation in opposite direction.

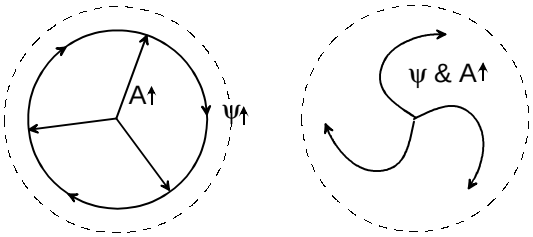

(a) **(b)**

Fig.3. (a) radial motion of the channels while *A* is increasing and circular motion when ψ is increasing; (b) spiral channels motion while *A* and ψ are increasing simultaneously.

3.3 Experimental realization: analysis of possibilities of the manipulator

The operating parameters were chosen widely by comfortable way of realisation in experiment. The variation of phase ψ can be produced with a mirror on the piezo-element put in optical setup. The use of piezo-elements for small space displacement is widely used technology in optics.

The parameter being the LG_0^0 mode amplitude can be changed by many ways. The simplest one is the introducing of an attenuator on the way of the beam. In our opinion, it is better to use the dielectric mirror, which possesses angular dependence of reflectivity. By the tuning of such mirror we are able to operate the intensity of the passing beam.

The principle used for the constructing of three-channel manipulator can be extended to the construction of a manipulator with any number of channels. Two modes are enough to construct these manipulators: LG_0^m and LG_0^0 modes, where $|m|$ is number of the channels. The advantage of such approach is that the number of operating parameters for manipulation remains two.

References

[1] A.Ashkin, J.M.Dziedzic, J.E.Bjorkholm and S.Chu, Observation of a single-beam gradient force optical trap for dielectric particles. Optics Letters, **11** (5):288,1986.

[2] H.Ne, N.R.Heckenberg, and H.Rubinzstein-Dunlop, Optical particle trapping with higher-order doughnut beams produced using high efficiency computer generated holograms. Journal of Modern Optics, **42** (1):217-223,1995.

[3] Basistiy I V, Marienko I G, Soskin M S and Vasnetsov M V, *Nonlinea*r *Dynamics in Lasers*, eds. N. B. Abraham and Ya. I. Khanin, *SPIE Proc*. **2792** (1996) 172.

Chapter 4
Optical-vortex fiber sensors (OVFS) with cw and pulse operation

Summary

The theoretical and experimental study of optical-vortex fiber sensors (OVFS) and their assessment are performed The computer simulation of applicability of short-pulse lasers in OVFS is carried out.

As a basis of OVFS, the physical approach involving the analysis of a light beam propagation along a OV-generated unit, OV-guided unit and OV-detection unit is developed. A computer processing technique of an output interference image was elaborated.

OV decay in a fiber was considered. Exploitation of optical fibers preserving a guided OV in supersensitive fiber-optical devices for a monitoring both temperature parameters and inertial navigation systems is discussed.

4.1 Analytical review and statement of the problem

The special properties of OVs enable us to develop new optical measurement and research methods [1-4]. In particular, the studies on the OV phenomena can also extend our understanding of the topological manifestations in different fiber-optical effects and, in turn, new fiber-optical devices.

Interferometric fiber-optical sensors have been the subject of considerations for last twenty years [5]. The application of OVs as probe and signal waves may stimulate new success in this area.

Although some types of fiber-optical sensors on the base of high-order fiber modes have been described before [6-8,12-14], their use for OV-based sensor are presented here for the first time.

Consider at first the main features of two- and one-arm single-mode fiber interferometers.

4.1.1 Two-arms fiber interferometer

Let the length of the reference arm be L_1 and the signal arm (fiber) L_2. The reference arm is thermally stabilized, and the signal arm is affected by the temperature variations. Hence, relative phase changes are restricted to the variations of the signal arm parameters. Therefore the phase in the reference arm is constant, and in the signal arm is

$$\Phi_2 = \frac{2p}{l}\tilde{n}L_2, \qquad (1)$$

where $\tilde{n}$ is the effective refractive index of the fiber for the fundamental HE_{11} mode of the fiber, l is the vacuum wavelength of the used source.

The temperature sensitivity of the system arises from thermal expansion and from the temperature dependence of the refractive index in the signal arm:

$$\frac{1}{L_2}\frac{d\Phi_2}{dT}=\frac{2p}{l}\left(\frac{\tilde{n}}{L_2}\frac{\P L_2}{\P T}+\frac{\P \tilde{n}}{\P T}\right), \qquad (2)$$

where T is the absolute temperature. Typically [7] $\frac{1}{L}\frac{\P L}{\P T}\propto 5\times 10^{-7}K^{-1}$, $\frac{\P \tilde{n}}{\P T}\propto 10^{-5}K^{-1}$, hence the temperature dependence of the refractive index dominates and $\frac{1}{L}\frac{d\Phi}{dT}\propto 100\frac{rad}{Km}$ for l =0.63 μm.

A number of data processing schemes for the fiber interferometer have been developed [5,7] which yield phase resolution in the $1mrad \div 1mrad$ range. The particular value of the

temperature sensitivity depends on an optical fiber structure. The birefringence single-mode fibers are affected by the most temperature action on account of strong internal tensions. For example, the birefringence fiber with the beat length up to 1 mm gives the temperature sensitivity more than $200\ \frac{rad}{Km}$ [7].

4.1.2 One-arm interferometer

Other type fiber optical interferometers are one-arm devices. In contrast to the two-arm interferometers those are extremely simple constructions. It requires only two polarizers for the splitting and reconstruction of the two interfering modes. A particularly advantageous sensor in this respect is a fiber-optical interferometer employing a fiber with high internal lateral stresses [9]. This fiber is highly birefringent, and two eigen-modes are the fast and slow HE_{11} modes of mutually orthogonal linear polarizations. The temperature sensitivity is due to the thermal expansion, which affects the magnitude of the internal lateral stress and, therefore, the fiber birefringence. Simultaneously, this fiber is fairly insensitive to isotropic pressure variations.

In all interferometric sensors discussed here, the phase response Φ is proportional to the length *L* of that section of a fiber, which is exposed to the external influence *F* to be sensed. The influence *F* may be caused by a variation either of temperature *T* or of other ambient thermodynamics values. The phase delay of modes in a fiber of length *L* is $\Delta\Phi = k\left(\tilde{n}_1 - \tilde{n}_2\right)L = k\Delta\tilde{n}\,L$, where $\Delta\tilde{n}$ is the difference of the mode effective indices. The phase response becomes

$$\frac{1}{L}\frac{d\left(\Delta\Phi\right)}{dF} = k\frac{d\left(\Delta\tilde{n}\right)}{dF} + k\Delta\tilde{n}\frac{1}{L}\frac{dL}{dF}. \qquad (3)$$

This is a *F*-sensitivity of the one-arm interferometer. If *R* is a birefringence, we have from Eq. (3)

$$\frac{d\left(\Delta\tilde{n}\right)}{dF} = \frac{\P\left(\Delta\tilde{n}\right)}{\P F} + \frac{\P\left(\Delta\tilde{n}\right)}{\P R}\frac{\P R}{\P F}. \qquad (4)$$

The temperature sensitivity for a stress-induced single-mode fiber may be expressed as [9]:

$$\frac{1}{L}\frac{d\left(\Delta\Phi\right)}{dT} = \frac{k}{L}\left(L\frac{\Delta\tilde{n}}{\tilde{n}}\frac{d\tilde{n}}{dT} + \Delta\tilde{n}\frac{dL}{dT} + L\frac{\Delta\tilde{n}\left(T\right)}{T - T_S}\right), \qquad (5)$$

where T_S is the softening temperature of the inner cladding. So the temperature sensitivity for the birefringent single-mode fiber with the beat length $\Lambda = 3.2\,mm$ or $\Delta\tilde{n} = 2\times10^{-4}$ is $\frac{1}{L}\frac{d\left(\Delta\Phi\right)}{dT} = 2.48\frac{rad}{Km}$, while the temperature sensitivity of the two-arm interferometer with the same fiber [9] becomes $\frac{1}{L}\frac{d\left(\Delta\Phi\right)}{dT} = 124\frac{rad}{Km}$.

In order to increase the temperature sensitivity of the one-arm interferometers one makes use of different special adjustments for a fiber. To the end, for example, an isotropic single-mode fiber is coiled under some tension around a hollow cylinder having a high thermal expansion coefficient [10]. In such a case the fiber becomes equivalent to a retardation plate with birefringence depending on the outer radius. When the temperature is increased the two principal indices of the fiber change because of thermooptic effect and elastooptic effect caused by the thermal expansion of the cylinder. As a consequence the phase shift of the eigen-modes are

modified by different amounts. In this way the temperature sensitivity $\frac{1}{L}\frac{d(\Delta\Phi)}{dT} = 340\frac{rad}{Km}$ has been reached.

The other way of the temperature sensitivity increase is concerned with the spectral registration of a fiber output signal [11]. If a white light excites the fiber the modes with different wavelengths has a different temperature response. This high accuracy method for spectral data processing allows achieving a temperature resolution of $3\times 10^{-3} K$ for a wide temperature range.

4.1.3 Dual-mode fiber sensor

In the works [6,12-14] the dual-mode acoustic and temperature sensors on the base of a multimode fiber are discussed. The multimode fiber turns out to enable to increase the sensitivity of the fiber-optical sensors. Two modes of the fiber (LP_{01} and LP_{11}) form two signal arms and produce differential phase change between the beams propagating in the two modes.

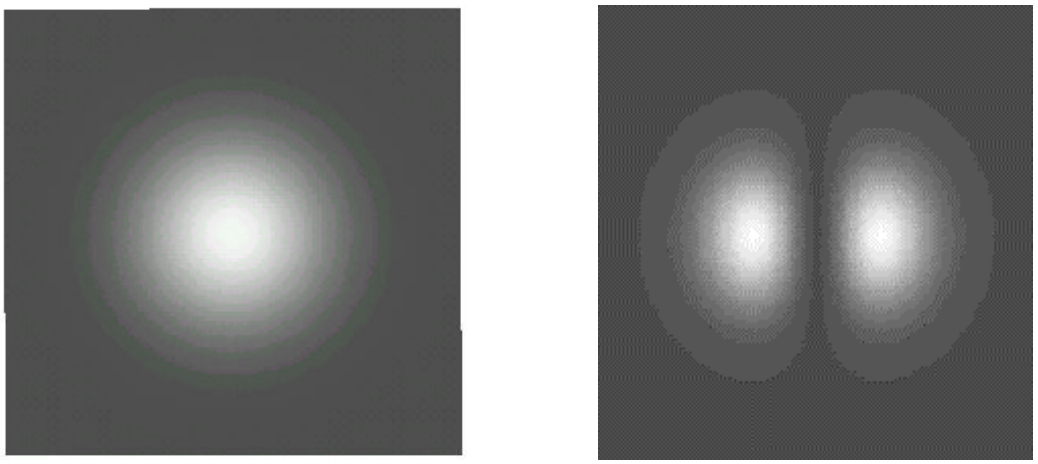

(a) **(b)**

Fig.1. Intensity distribution of LP_{01} (a) and LP_{11} (b) modes at the fiber cross-section [6].

The fiber used in the experiments of the work [6] was a conventional quasi-step index communications type fiber designed to be single-mode at 1.3 μm. The experiments were performed in the 1 μm wavelength region where the fiber guides two modes, according to [6]. The polarization state of the two modes was the same. As it can be seen from Fig.1b, the intensity structure of the LP_{11} mode represents two lobes because of the p - phase difference between them. The phase variations take place due to the different phase velocities of LP_{01} and LP_{11} modes. The variation in the phase difference can be seen as a transfer of power between two lobes. The simplest detection scheme selects, spatially, a single lobe from the fiber near field, and as the phase difference is varied, the detected intensity oscillates through a series of maxima and minima. This method of the signal registration gives only $0.18\frac{rad}{Km}$, while the spectral registration method raises the temperature sensitivity up to $150\ \frac{rad}{Km}$ [6] (the sensor with the spectral registration method is considered Section 4.3.3).

4.1.4 Statement of the problem

Fiber-optical sensors have been a research field in their own right since 1975. Some sensors have been the subject of intense research, particularly for hydrophone and gyroscope applications, and some extremely complex and highly sensitive devices have been engineered.

Nevertheless, there are a large areas which have received relatively little attention and there is much scope for the development of novel and improved sensing devices, in particular, the fiber-optical sensing on the base of multimode fibers.

Indeed, development of those highly sensitive schemes as two-arms interferometers (for example, Mach-Zehnder interferometer configuration) is faced with great difficulties. The main problems with this technique are connected with occasional phase shift caused by physical variations other than ones to be measured. At the same time, the two-arms interferometric sensors of temperature, for example, have the temperature sensibility more than $100\frac{rad}{Km}$.

These problems are partially solved by means of utilizing of the one-arm interferometers, in particular, the devices on the base of multimode fibers. These temperature sensors are able to raise the temperature sensitivity up to $200\frac{rad}{Km}$ and more if the spectral registration of signals is used. However the intensity registration conceals some problems. The main one is concerned with noise sources such as laser instability or laser intensity fluctuations.

Moreover, the use of a multimode fiber assumes a monomode or duel-mode regime, i.e. one or two modes must propagate along the fiber only. In turn, this tough requirement is closely associated both with the excitation conditions of the fiber and concordance of mode polarizations. So, authors of the work [6] claim that the modes LP_{01} and LP_{11} transmit through the fiber sensor as the eigen-modes, and these modes have the same polarization state. However, the LP_{11} mode is known [15] to be no the fiber eigen-mode but to be either the sum of TE_{01} and HE_{21}^{od} or TM_{01} and HE_{21}^{ev} fiber eigen-modes. Moreover, their polarization state changes along the fiber and the linear polarization is recovered at certain planes of the fiber cross-section only. Hence, the dual-mode fiber sensor is an instable device with a strong mode noise: any slight fiber perturbations cause the experimental mistakes.

In order to avoid or to reduce the intensity instability it is necessary to interchange the registration method in principle by another one. The mode noise may be reduced by means of the excitation of a relatively more stable mode superposition such as circularly polarized fields.

The OV fiber modes have these properties. On the one hand, the singular beams are the circularly polarized eigen-modes, which propagate along the circular optical fiber without changes of their field structure [16,17]. On the other hand, the interference pattern of the optical vortex and fundamental Gaussian beam represents the spiral-like image rotating around its axis due to the phase difference between the signal and reference beams [18,19]. Besides, the rotation angle of the spiral image is directly proportional to the phase difference between the beams. In this case the registration process becomes different: the data processing is replaced by the image processing. This enables us to avoid the influence of laser intensity fluctuations and to raise the sensitivity of the fiber-optical device.

On the base of the above listed conclusions the follow problems of investigations were studied:

1) Theoretical and experimental study of OVFS.

2) Consideration and computer simulation of applicability of short-pulse lasers in OVFS. Theoretical and experimental solution of these problems will be done in the following sections.

References

1. W.L. Power, L Allen, M. Babiker, V.E. Lembessis. Atomic motion in light beams possessing orbital angular momentum, Phys. Rev. A.**52,** (1995) 479-488.
2. M. Babiker, V.E. Lembessis, W.K. Lai, L Allen. Doppler cooling of ion cyclotron motion in counter-propagating Laguerrre-Gaussian beams, Opt. Commun. **123** (1996) 523-539.

3. M.Totzek, H.J.Tiziani. Phase singularities in 2D diffraction fields and interference microscopy, Opt. Commun. **138** (1997) 365-382.
4. K.T. Gahagan, G.A. Swartzlander, Simultaneous trapping of low-index and high-index microparticales observed with an optical-vortex trap. J .Opt. Soc. Am. **B15** (1998) 533-537.
5. B. Culshaw. Optical Fiber Sensing and Signal Processing. London, U.K.: Peter Peregrinus, 1984.
6. J.L. McMillan, S.C. Robertson. Single-mode optical fiber sensors. GEC Journal of research **2**, No 2 (1984) 119-124.
7. J.D.C. Jones, D.A. Jackson Monomode fiber optic sensors, Analytical Proceedings. **22** (1985) .207-211.
8. N.Shidata, M.Tateda, Sh.Seikai, N.Uchida. Spatial technique for measuring modal delay differences in a dual-mode optical fiber. Applied Optics. **19**, No 9 (1980) 1489-1492.
9. W.Eickoff. Temperature sensing by mode-mode interference in birefringent optical fiber. Optical Lett. **6**, No4 (1981) 204-206.
10. D.Chardon, J.Huard. A new interferometric and polarimetric temperature optical fiber sensor. Journ. Lightwave techn. **LT-4**, No7 (1986) 720-725.
11. R. Courts, A.V. Khomenko, A.N. Starodumov, N. Arzate, L.A. Zentano. Interferometric fiber-optic temperature sensor with spiral polarization couples// Optical Commun. **154** (1998) 268-272.
12. M.R. Layton, J.A. Bucaro. Optical fiber acoustic sensor utilizing mode-node interference. Appl. Opt. **18** (1979) 666-670.
13. J.L. Mcmillan, S.C. Robertson. Duel-mode optical fiber interferometric sensor. Electron. Lett. **20** (1984) 136-137.
14. J.W. Attrige, J.R. Cozens, K.D. Leaver, N.L. Webster. Coaxial fiber sensors. Journ. Lightwave Tecgn. **LT-3**, No3 (1985) 1084-1091.
15. A.W. Snyder, J.D. Love. Optical Waveguide Theory. London-New York, Chapman and Hall, 1983.
16. K.N. Alexeyev, T.A.Fadeyeva, A.V. Volyar, M.S. Soskin. Optical vortices and the flow of their momentum. Semiconductor Physics, Quantum Electronics & Optoelectronics. **1** (1998) 1-8.
17. K.N. Alexeyev, M.S. Soskin, A.V. Volyar. Spin-orbit interaction in a generic vortex field transmitted through an elliptic fiber, Quantum Electronics & Optoelectronics. **3**, No4 (2000) 501-513.
18. Basistiy I.V., Bazhenov V. Yu., Soskin M.S., Vasnetsov M.V. Optics of light beams with screw dislocations// Opt. Comm. **103** (1993. V.. P.422-428.
19. A.N. Alexeyev, A.V. Volyar, Y.V. Izdebskaya, M.S. Soskin Fiber-optical interferometric sensors of physical values with a singular reference beam, SPIE Proc. (2000) 4403 P.264-266.

4.2 Optical-vortex fiber sensors

The review performed above has showed numerous advantages of OVFS on the base of low-mode and single mode fibers as against other technologies. Such their properties as high sensitivity, resistivity to external electromagnetic perturbations, geometrical versatility, safety in hazardous environment and so on make them irreplaceable devices for quite a number of applications. We shall consider sensors based on low-mode fibers and further restrict our attention to those worked into single-vortex regime.

4.2.1 Guided optical vortices and devices on their base

OV transmittion through inhomogeneous medium of an optical fiber has essential differences with those propagation in free space. Without going into detail discussed in the works [1-6] at full length, we outline general traits of these guided field forms.

At once it is worthy to note that guided OVs are the main form of a field existing in circular optical fibers. All other eigen-modes of a fiber can be presented as an OVs superposition since the guided OVs by themselves are the eigen-modes written in a circularly polarized basis [1,2,5]. There is exception of this rule: azimuthally-symmetric TE and TM modes can not be written in the circularly polarized basis because of their specific field structure [2,3]. The fact is that the guided OV is essentially vector field structure, due to impossibility to separate its topological charge l and circular polarization state characterized by a helicity $s = \pm 1$ (the sign of the circular polarization). This OV property is a consequence of a spin-orbit interaction in the OV field [4]. The difference between OV and TE and TM modes manifests itself as polarization corrections db to a scalar part of the propagation constant of a mode $\tilde{b} : b = \tilde{b} + db$. The polarization corrections for TE and TM modes are strongly differed so that their superposition $TM \pm iTE$ is unstable [2]. Although this superposition forms vortex-like structures at some fiber lengths, in the intermediate distances, there is a mode mixture without definite topological charge and helicity (the polarization state). This mode superposition is called sometimes as IV mode (instable vortex). In contrast to the IV mode, the guided OV called CV mode (circularly polarized vortex) in any point has definite state with both positive topological charge and helicity $|+1,+1\rangle$ or negative ones: $|-1,-1\rangle$. There are, as a rule, one CV mode and one IV mode in a low-mode circular fiber (*l=0,1*). In an anisotropic fiber such as a strongly elliptic-core fiber or a stress-induced core fiber, the CV mode in a pure state cannot exist [6]. Nevertheless, a slightly birefringent fiber or even a fiber with a strong circular birefringence maintains CV vortex at large distance [7].

Therefore we have employed either fibers with a slight birefringence or circular core-birefringent ones as a sensitive element of a fiber-optical sensor which the guided vortices can be translated through. The typical scheme of a OVFS is reproduced in Fig.1 [7].

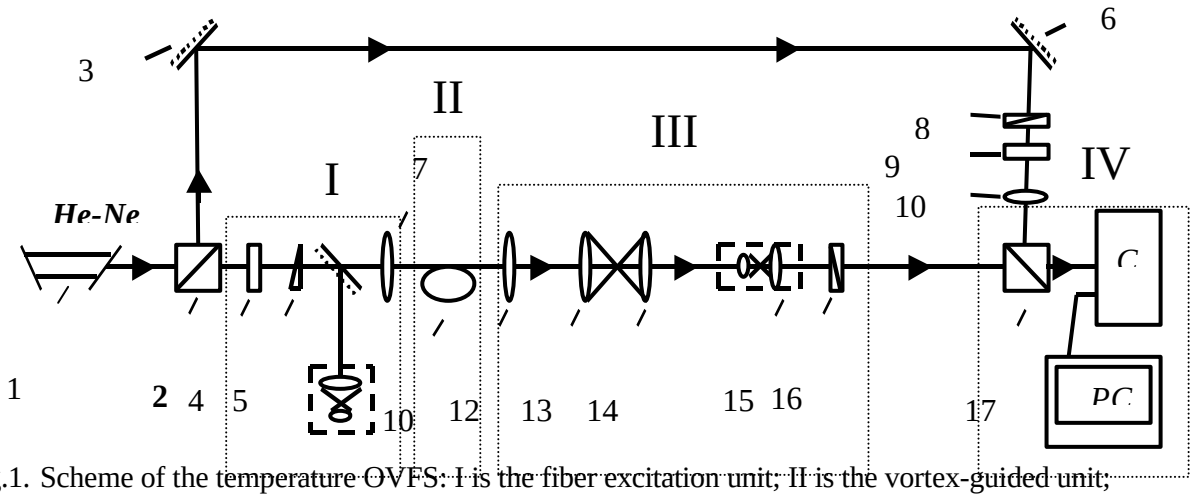

Fig.1. Scheme of the temperature OVFS: I is the fiber excitation unit; II is the vortex-guided unit; III is the vortex-forming output unit; IV is the detection unit matched with the image processing system. 1 is the He-Ne laser; 2,17 are the beam splitters; 3,6 are the mirrors, 4 is the $\lambda/4$ plate; 5 is the optical wedge, 7,12 are the microlenses, 8,16 are the polarizers, 10 is the optical fiber, 13,14- are the co-centered microlenses, 15 is the collimator, 18 are the CCD matrix and PC.

There are four main units in this scheme that will be analyzed in the following subsections: the fiber excitation unit, the vortex-guided unit, the vortex-forming output unit and the detection unit matched with the image processing system.

The fiber excitation unit serves for the excitation of the CV mode in a low-mode fiber.

The vortex-guided unit is an optical fiber positioned into a special arrangement reinforcing influence of a physical parameter under test.

The output unit consists from two microlenses (and diaphragm between them, if necessary).

The detection and image-processing unit employs the CCD-matrix matched with computer for recording and processing of experimental data in a real time.

The consequent subsections are devoted to the detailed analysis of the each optical unit.

References

1. A.V. Volyar, T.A. Fadeyeva Optics of singularities of a low-mode fiber: I. Circular disclinations// *Optics and Spectroscopy*.V.85.No.2, pp.264-271 (1998).
2. A.V. Volyar, T.A. Fadeyeva Optics of singularities of a low-mode fiber: II. Optical vortices// *Optics and Spectroscopy*. V.85. No.2, pp.272-280 (1998).
3. A.V. Volyar, T.A. Fadeyeva Optical vortices in low-mode fiber: 1. Angular momentum of field// *Optics and Spectroscopy.* V.86. No.2, -pp.242-250. (1999).
4. A.V. Volyar, V.Z. Zhilaitis, V.G. Shvedov Optical eddies in small-mode fibers: 2. The spin-orbit interaction, *Optics and Spectroscopy*. V.86. No.4, pp.664-670. (1999)
5. K.N.Alexeyev, T.A. Fadeyeva, A.V.Volyar, M.S. Soskin. Optical vortices and the flow of their angular momentum in a multimode fiber// *Semiconductor Physics. Quantum Electronics & Optoelectronics.* V.1. No.1, pp.1-8. (1998).
6. C.N. Alexeyev, M.S.Soskin, A.V. Volyar Spin-orbit interaction in a generic vortex field transmitted through an elliptic fiber // *Semiconductor Physics. Quantum Electronics & Optoelectronics.* V.4. No.3, pp.500-513. (2000).
7. A. Volyar, T. Fadeyeva Transmitting, destruction and self-recovery of the optical vortices in low-mode fiber-optical systems // SPIE proc. 2001 (to be published).

4.2.2 High-efficiency generation of optical vortices

As a rule, coupling of an optical fiber and an OV beam in free space is connected with energy losses up to 50% and more. Besides, energy efficiency of an OV beam generation by computer-generated holograms, widely discussed in a number of works (see, for example, [1] and references therein), amounts several percents. Consequently, a computer-generated hologram/optical fiber system has very low efficiency for a design of the OVFS.

On the other hand, a number of the experimental results [2] shows that a rather simple optical device such as an optical wedge enables us to obtain OVs with the high efficiency. Some theoretical aspects of this problem have been recently considered in the work [3].

The aim of the given section is the experimental and theoretical study of the diffraction of a Gaussian beam by an optical wedge as a high efficiency device for an OV beam generation.

Let us consider an optical wedge illuminated by a Gaussian beam (see Fig.1) in such a way that one-half of the beam passes through the wedge and the other-half propagates in free space.

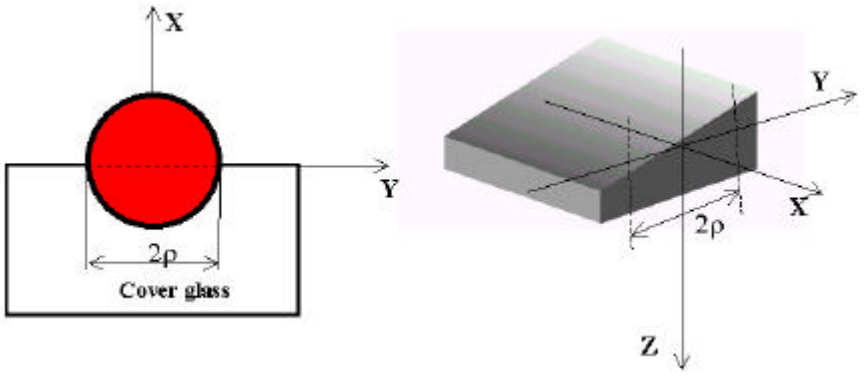

Fig.1. The Gaussian beam diffraction by the optical wedge.

If peripheral rays of a laser beam have the phase difference $2p$, then a circuit with the radius r around optical axis gives $2p$. It is the relevant requirement of an optical vortex existence. However, the phase shift on the computer-generated hologram is not dependent on the circuit radius while this requirement does not fulfilled in our case. The OV formation by the optical wedge is therefore more complicated process.

The analysis of the OV generation was performed by means of the Kirchhoff integral [4] for a far field. The wave function has a form:

$$\Psi = \frac{1}{2}\frac{r}{z}\sqrt{\frac{2zp}{\nu}}\exp\left[i\frac{1}{2}arctg\left(\frac{z_0}{z}\right)\right]\exp\left[-2k\left(z_0 - i\,z\right)\frac{x^2+y^2}{\nu^2}\right]\times$$

$$\times\left\{\exp\left[-2kz_0\frac{z(n-1)\,tga\,\left[z(n-1)tga-2y\right]-i\,2z_0(n-1)tga\left[y-\frac{1}{2}z(n-1)tga\right]}{\nu^2}\right]\times\right.$$

$$\left.\times\exp\left[i(2m+1)(n-1)p\right]\ erfc\left[\sqrt{\frac{k}{2}}\frac{x}{\sqrt{i\,z\left(1+i\frac{z}{z_0}\right)}}\right] + erfc\left[-\sqrt{\frac{k}{2}}\frac{x}{\sqrt{i\,z\left(1+i\frac{z}{z_0}\right)}}\right]\right\}, \quad (1)$$

where a is the wedge angle, $\nu = \sqrt{2\left(z^2+z_0^2\right)}$, $z_0 = \frac{kr^2}{2}$ is the Rayleigh length, $erfc(Z) = 1 - erf(Z)$, $erf(Z) = \frac{2}{\sqrt{p}}\int_0^Z \exp\left(-t^2\right)dt$ is the probability integral.

The key role in the OV beam formation plays the relation between the beam waist r and the wedge angle a. From eq.(1) we obtain the following expression for a very wide beam (nearly plane wave) incident on the wedge:

$$\Psi_\infty \approx \sqrt{\frac{2p}{kz}}\,e^{i\frac{p}{4}}\left\{\exp\left[i\frac{1}{2}(n-1)\,ktga\left[2y+z(n-1)tga\right]\right]erfc\left(\sqrt{i}\,x\sqrt{\frac{k}{2z}}\right)+erfc\left(-\sqrt{i}\,x\sqrt{\frac{k}{2z}}\right)\right\} \quad (2)$$

It is interesting to give a comparison of the theoretical results obtained by means of eq. (2) and the experiment (see below).

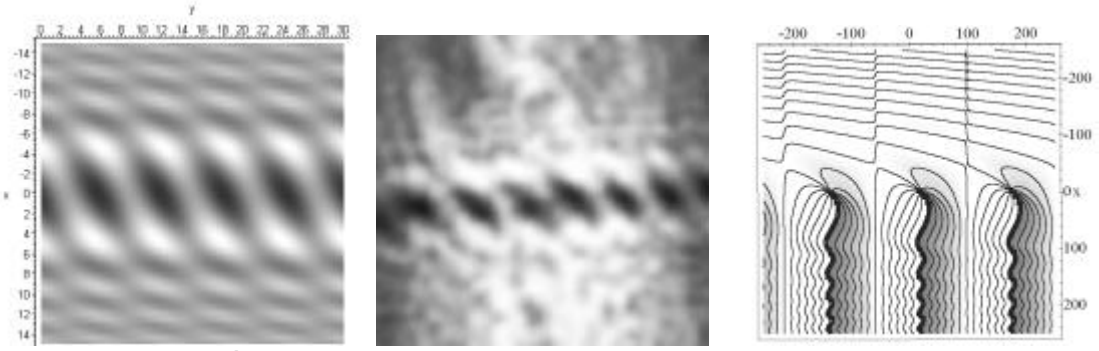

à b ñ

Fig.2. The generation of OVs street by the optical wedge: (a) theory; (b) the experimental results obtained by a microscope cover glass; (c) the theoretical phase distribution in the OVs street. The distance from the glass wedge is $z = 1000\ l$, the beam waist is $r = 500\ l$, and the wedge angle is $a = 0.08\ rad$.

The distance Δy between neighboring vortices in the street is defined by Eq. (2):

$$\Delta y = \frac{l}{(n-1)\tan a}, \qquad (3)$$

where n is the refractive index of the wedge.

A single OV will appearin in the optimal form, if the distance between OVs is $\Delta y = 2r$. From eq. (3) one has

$$r = \frac{l}{2(n-1)\tan a}. \qquad (4)$$

The good agreement of analytical (Fig.2a,c) and experimental (Fig.2b) results allow us to rely on theoretical predictions in designing of a high efficiency device of the OV generation.

Consider now the properties of an optimal-formed OV.

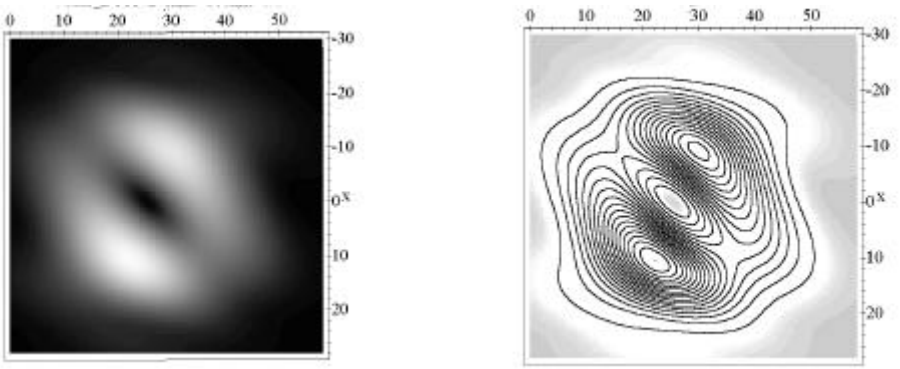

(à) (b)

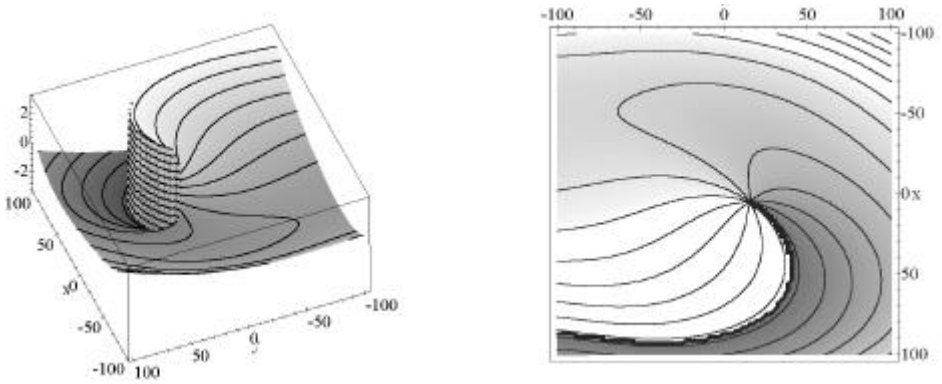

(c) (d)

Fig.3. The intensity in gray scale (a), the intensity level lines (b), phase surface (c), and equal phase lines (d) for the optimal OV, calculated by eqs.(1) and (4) under $z = 1000\,l$, $a = 0.08 rad$

The experimental investigation of the OV generation by an optical wedge was implemented in experimental set-up shown in Fig. 4.

The first set-up (Fig. 4a) enables to observe the generation process of the OV street and the optical wedge features by means of the interference pattern in the reflected light [5]. The second set-up (Fig.4b) enables to study the properties of a single OV. The cover microscope glass plates were used as samples of optical wedges. The interference pattern shown in Fig.5 points out the modulated wedge thickness.

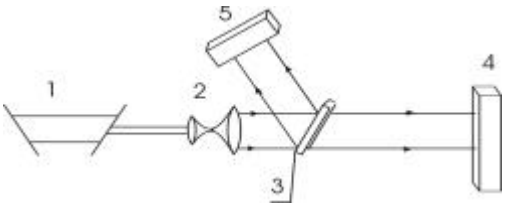

(a)

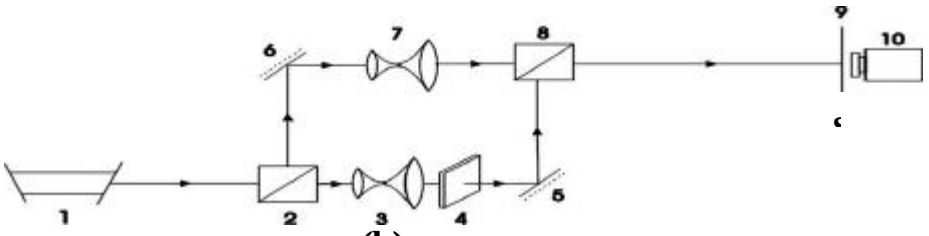

(b)

Fig.4. The experimental set-up for the investigation of a Gaussian beam diffraction by an optical wedge. (a) Generation of the OV street: 1 is the He-Ne laser, 2 is the telescopic objective, 3 is the optical wedge, 4,5 are the CCD matrices. (b) Generation of a single OV: 1 is the He-Ne laser, 2,8 are the beamsplitters, 3,7 are the telescopic objectives, 5,6 are the mirrors, 9 is the diaphragm, 10 is the CCD-matrix.

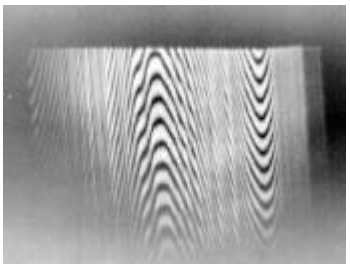

(a)

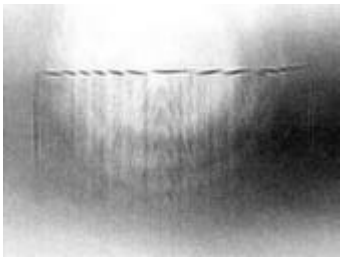

(b)

Fig.5. The interference pattern obtained in the beam reflected by the cover glass (a) and the corresponding OV street in the transmitted beam (b).

Because the period of the cover glass modulation is rather large, an area with a nearly straight wedge can be chosen.

The typical experimental picture demonstrated in Fig.6 (a) gives a good agreement with the theoretical prediction of a single OV generation depicted by Fig.6 (c).

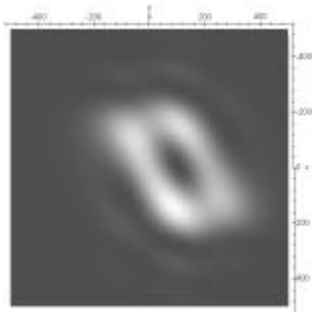

(a)

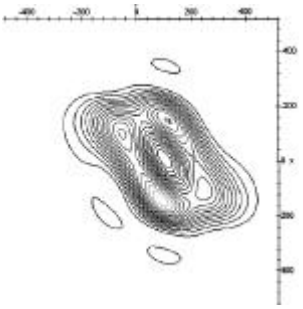

(b)

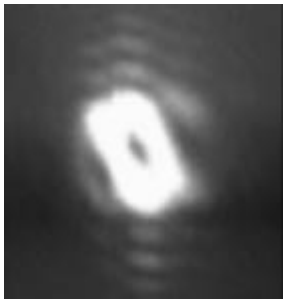

(c)

(d)

Fig.6. The intensity distribution and level lines of the optimal OV generated by the optical wedge with angle $a = 8.8 \times 10^{-4} rad$: (a,b) the experiment, (c,d) the theory.

The considered above study should be treated as a preliminary approach to the problem of a high-efficiency generation of OV for OVFS. The analytical and numerical analysis, confirmed by the experimental results, shows the simple way for obtaining of an OV with a high efficiency. The shape of the single vortex is defined by both the wedge and laser beam parameters.

References

1. M.S. Soskin, M.V. Vasnetsov. // Horizons in World Physics, edited by M. Vasnetsov and K. Staliunas, 1999. V. 228. P. 1-35.
2. N. Alexeyev, O. S. Borodavka, V. G. Shvedov. Birth and evolution of the optical dipoles on the dielectric transparent wedge, Proceedings of SPIE. 1999, 3904. P.68-73.

3. V. Gorshkov at all.// SPIE proc. 2001. (to be published).
4. M.Born, E. Wolf. Principles of optics. Oxford, Pergamon Press, 1968.
5. Izdebskaya Ya., Shvedov V., Kurabtzev D., Alexeyev A., Volyar A. " The optical vortex generation by optical wedge" // SPIE proc. (to be published).

4.2.3 Design and assessments of the two-arms fiber-optical interferometer on the base of an optical vortex

The main advantages and imperfections of single- and multimode sensors having been in detail discussed in the Section 4.1. The aim of the given section is to develop the design and to carry out the assessments of the OVFS as whole. We shall consider here two possible constructions of the two-arms interferometers differed by transmission ways of an optical vortex through either a signal or a reference arm [1]. In the former case the OV propagates along a fiber and it is a guided fiber mode, and we deal with a free-space OV in the latter case.

The greatest advantage of the OV sensor is that the development of a new interferometric technique of the image processing enables us to extend essentially the range of the device linearity and to eliminate partially noise caused by intensity instabilities of a light source.

The sketch of the experimental set-up is represented in Fig.1.

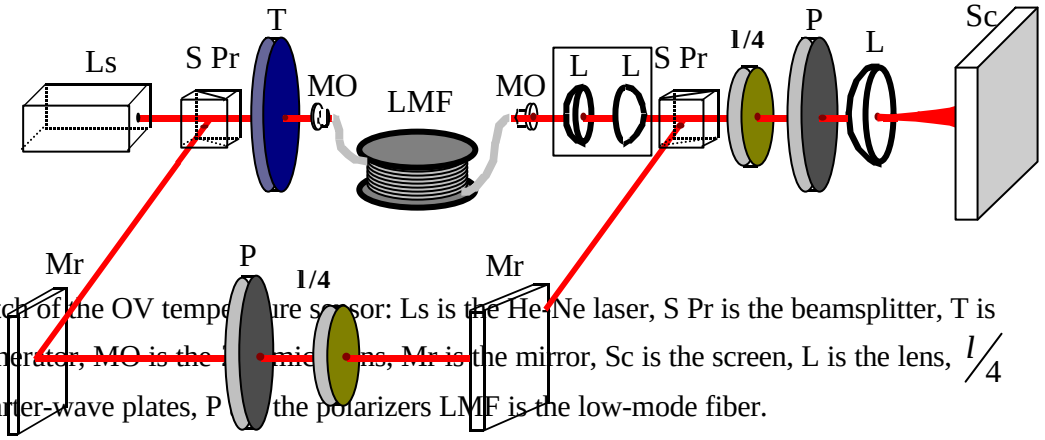

Fig.1. Sketch of the OV temperature sensor: Ls is the He-Ne laser, S Pr is the beamsplitter, T is the OV generator, MO is the microlens, Mr is the mirror, Sc is the screen, L is the lens, $l/4$ are the quarter-wave plates, P are the polarizers LMF is the low-mode fiber.

The linearly polarized light from the single-frequency laser (l =0.6328 μm, power is about 2 mW) in a form of a fundamental Gaussian mode passed through the beamspliter forming the two arms of the interferometer. In the reference arm, the beam was attenuated by the polarizer P and then transformed into the circularly polarized one after the $l/4$- plate. The reference arm was put inside a thermostat to protect the arm from possible ambient temperature variations. In the signal arm, three main optical units were positioned. In the vortex-generating unit, the Gaussian beam diffracted by the optical wedge was converted into the OV. The scattered light was cut off by the optical filter consisting from two lenses and a diaphragm between them.

The cleaned OV was launched into the fiber by the $20^{\times}$ microlens. The conventional low-birefringent optical fiber consisting from the GeO_2 / SiO_2 core and the B_2O_3 / SiO_2 cladding with circular cross-section was used as a guided vortex system. The birefringence was less than 10^{-6}, the core radius was r = 4 μm, the fiber parameter was V = 5.1. This fiber could maintain the following modes (in the linearly polarized basis): fundamental $HE_{11}^{ev}, HE_{11}^{od}$ and $HE_{12}^{ev}, HE_{12}^{od}$ modes, azimuth symmetric TE_{01}, TM_{01} modes and hybrid $HE_{21}^{ev}, HE_{21}^{od}$, $EH_{11}^{ev}, EH_{11}^{od}, HE_{31}^{ev}, HE_{31}^{od}$ modes. They are associated with the following types of vortices: $HE_{11}^{\pm}, HE_{11}^{\pm}, CV_{11}^{\pm}, IV_{11}, CV_{21}^{\pm}$. The higher modes, such as the $CV_{21}^{\pm}$ vortex or $EH_{11}^{ev}, EH_{11}^{od}, HE_{31}^{ev}, HE_{31}^{od}$ modes, have the excitation effency less than 10 %. The fiber ends

were fixed on a 3-coordinate tables provided by microscrews with transverse and longitudinal displacements about 5 μm. The input and output microobjectives were mounted on the 3-coordinate tables provided by microscrews and a hydraulic mechanism with accuracy up to 0.5 μm. The OV generation unit has also the lateral image microscope to observe the vortex spot position at the fiber input face. The fiber was coiled without tension around a copper cylinder with 32 mm outer diameter and 30 mm inner diameter was placed into a bath with oil. Then, this construction was put in a thermostat, where the temperature was measured by a thermocouple with the precision 0.05° C at the range from 20° to 50° C.

Two centered $20^{\times}$ microobjectives, mounted on optical tables, were placed at the fiber output. The optical tables were supplied with microscrews and a hydraulic arrangement to provide an accuracy of the displacement up to 0.5 μm.

The signal and reference beams were combined by the beamsplitter and directed to the window of a CCD-matrix producing the image on the TV monitor. The interference pattern looks like a spiral fringe [1]. The CCD-matrix having 512×582 sensitive elements and was matched with computer Pentium-3 (800) to process the spiral interference image in real time. We detected the rotation of the interference spiral and calibrated the rotation angle in temperature degrees.

The experiment runs as follows. The OV generation unit forms a CV mode for launching it into the fiber (see Section 4.2.3). The free OV and the guided CV mode will be completely coupled if only their transversal parameters are the same. In reality the OV beam axis is slightly inclined and a little bit displaced relative to the fiber axis. As a result, the additional eigen-modes in the fiber such as IV mode and the fundamental HE_{11} mode are excited. The HE_{11} mode field displaces merely the CV mode center and causes no noise for the sensor operation. The IV mode produces fairly strong noise effect to the interference image. Even a slight displacement of the OV beam spot relative to the fiber axis (less than 0.5 μm) stimulates an appearance of the IV mode (see Section 4.2.4). The sensitivity of the sensor radically reduces as the measurement error raises. Besides, even if the free and guided vortices are strongly coupled and the only CV mode is excited in the fiber input, any slight perturbations of the fiber itself cause the IV mode birth and, consequently, growth of the measurement error. For the pure CV mode exitation the laser spot at the fiber face must be positioned with accuracy better than 0.5 μm relative to the fiber axis.

If the only CV mode appears at the fiber output, or the noise intensity is as little as third of the CV mode intensity, the filtering two-lens system is removed from the set-up. For large noise level the measurements are run as it is described in Section 4.2.4.

After adjusting the set-up we carry out cleaning of an interference spiral image from the noise. The contrast of the spiral image can be improved by equalizing of the intensities of the reference and signal beams. Besides, the interference image must have no large-scale patterns. To eliminate them, optical filter is placed in the reference arm. In the signal arm this function carries out the two-lenses/diaphragm system.

The image of the interference spiral is directed to the computer image processing. The experimental results (temperature) are displayed on the TV monitor simultaneously with the spiral image in a real-time scale with the time resolution about 0.4 c (see Section 4.2.5).

Figure.2 represents the typical experimental results.

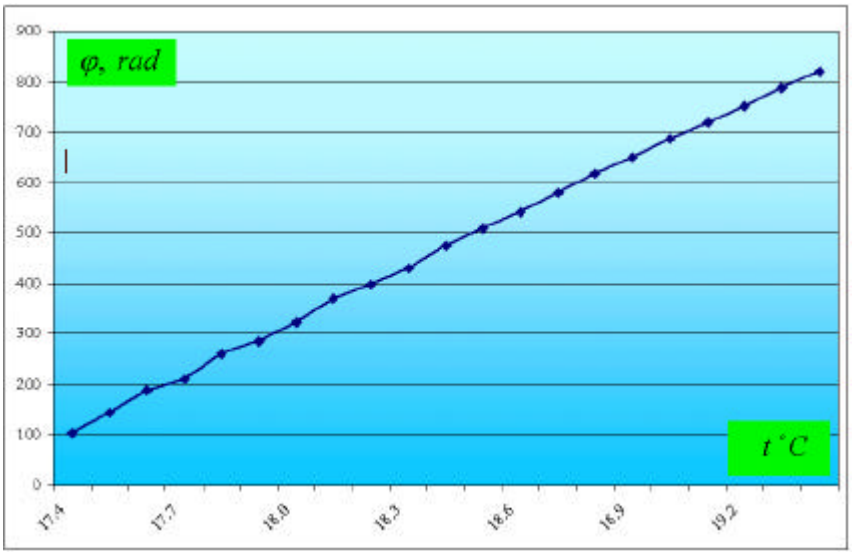

Fig.2. The experimental dependence of the spiral angular position j (in rad) vs the temperature t° C for the fiber-optical interferometer with the CV in the signal arm.

As it can be seen from the curve in Fig. 2, the temperature dependence of the angular rotation has a linear character at a temperature range from 20 to 50 ^{o}C. In contrast to conventional types of fiber optical sensors, our vortex sensor has a linear range of the angular dependency within $0 \div 2p$ interval of phase shift variations between a referent and signal beam. Deviations of the linearity are within to 0.01 rad. The temperature sensitivity is about 140 $\frac{rad}{Km}$. The experimental reproducibility for different 2.5-meter pieces of the same fiber is up to 2 %.

We have also considered an alternate type of a OVFS [2]. A single-mode fiber was used in a signal arm and a free OV beam served as a reference. The single-mode low-birefringence fiber had the following parameters: the core radius r = 3.4 μm, the waveguide parameter V= 2.1 at the wavelength 0.63 μm, the linear birefringence was less than 10^{-6}. So, the fiber can maintain the $HE_{11}^{\pm}$ mode only. For example, exciting the fiber by the right-hand polarized with an ellipticity degree Q = 0.99 Gaussian beam, we obtain Q = 0.73 after passing through the 10 m-length fiber. Consequently, the beating length in the given low-birefringent waveguide is less than 20 m.

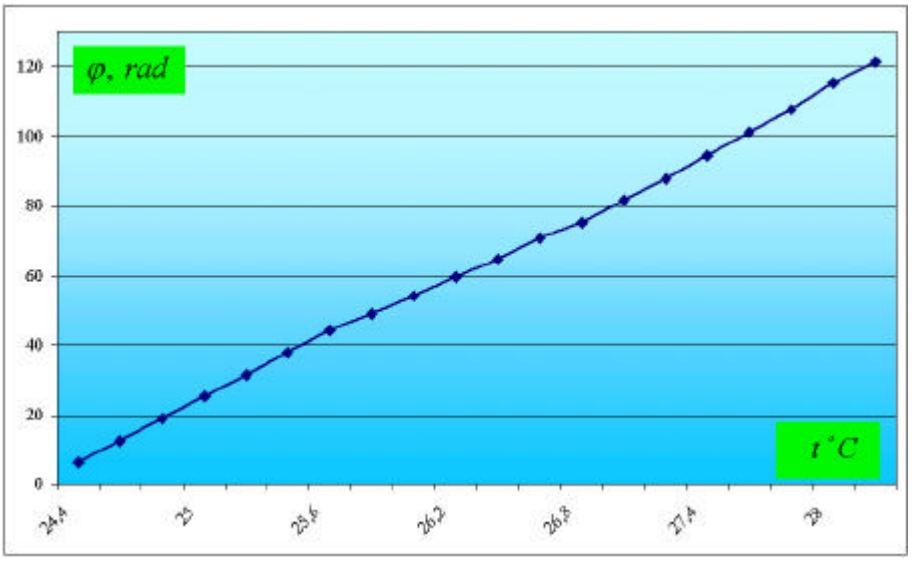

Fig.3. The experimental curve as a function of the interference spiral rotation j (in rad) vs the temperature t ^{o}C for the fiber-optical interferometer with a vortex in a reference arm; fiber length is about 27 cm.

The free OV propagated along the signal arm. It should be noted that a coherence length of our single-frequency laser source was a fairly large. The contrast of the interference image in the fiber-optical interferometer with the arm difference about 30 m was not less than 0.9.

Similar to the former case we measured the dependence of the angular rotation of spiral image vs temperature variations. Figure.3 illustrates a nearly straight line as a function of the angular position j (in rad) and the temperature t° C. Though the latter design is a steady sensor relative to random mechanical perturbations we can see that the sensibility of it is about 110 $\frac{rad}{Km}$ while the linearity and the accuracy is similar to the former sensor.

The grater sensibility of the interferometer with a vortex in a signal arm is a result of that the guided CV vortex propagates along a fiber with a less phase velocity than a HE_{11} that is an optical path for the same fiber length is larger.

Thus, we have experimentally realized two types of a two-arm OVFS with the OV in the signal or reference arm and carried out the assessments of their operation.

References

1. A.N. Alexeyev, A.V. Volyar, Y.V. Izdebskaya, M.S. Soskin Fiber-optical interferometric sensors of physical values with a singular reference beam // SPIE proc., 2000. V.4403. P.264-266.
2. Yu. Egorov, A. Alexeyev, 0. Shipulin, A. Volyar, M. Soskin Birth and Death Events in Topological Multipole Fields after Emitting from an Optical Fiber // SPIE proc. (to be printed).
3. A.W. Snyder, J.D. Love. Optical Waveguide Theory. London-New York, Chapman and Hall, 1983.

4.2.4 Fiber-optical interferometer with the OV recovery system

Notwithstanding the fact that any slight ambient perturbations affected the OV on the base a conventional low-mode fiber cause a strong mode noise of the interferometer, its high sensitivity and a constructive simplicity permit to design special devices for filtering of outside noise. At the same time, in order to avoid of unnecessary energy losses, a noise field must be conversed into a useful signal. Evidently, there exist no physical mechanisms to ensure that process over all optical fiber length. Nevertheless, it had been known some nonlinear ways for recovering of a useful optical information without energy losses at the fiber input [1]. In our case, it is necessary to recover an optical information carrying with optical vortices. The fact is that an initial guided OV split into a number of other optical vortices at the expense of external perturbations but a total topological charge is preserved. It turns out to be possible an inverse optical process of annihilating of «parasitic» optical vortices and recovering of the initial one so as a total topological charge is preserved as well [2,3].

The aim of the given section is to study experimentally and theoretically death, birth and recovery processes of optical vortices at an optical fiber input.

Let us consider the optical system consisting of an optical fiber and two short-focusing lenses (Fig.1). The first lens forms the image of the fiber output at the inner observation plane Z, the second lens passes this image at the outer observation plane P.

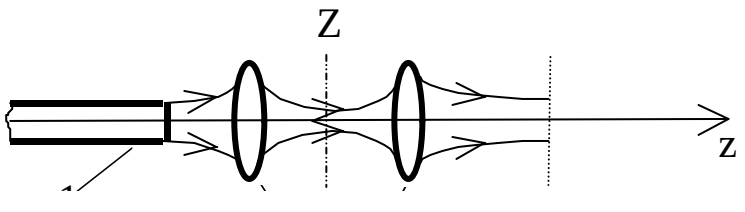

Fig.1.The sketch representation of the experimental set-up: 1is the optical fiber, 2 are the short-focusing lenses

Let us suggest that the CV vortex, the fundamental HE_{11}, HE_{12} and LP_{22} modes are realized in the optical fiber. It is a typical case of the CV excitation in a conventional low-mode fiber [4,5]. In the scalar nonparaxial approximation the wave function of the light near the focal plane Z has a form [2,3]:

$$\Psi^{(D)} = \Psi_{02}^{(LB)} + G \cdot \Psi_{1,1}^{(ED)} + F \cdot \Psi_{0}^{(0)} + D \cdot \Psi_{11}^{(V)}, \quad (1)$$

where $\Psi_{02}^{(LB)} = \left(1 - \frac{2}{3}kz_0\right) j_0(kR) - \frac{1}{3}kz_0\left(2 - 3\frac{r^2}{R^2}\right) j_2(kR)$ is the combined Legandre–Bessel beam, $\Psi_{11}^{(ED)} = \frac{r}{R}\cos j \; j_1(kR)$ is the Legendre–Bessel beam with *l = m = 1*, $\Psi_0^{(0)} = j_0(kR)$ is the fundamental Bessel beam, $\Psi_{11}^{(ED)} = \frac{r}{R}\exp(ij)\, j_1(kR)$ is the nonparaxial OV, $j_m(kR)$ is the spherical Bessel function of the first kind, *m*-th order, $R = \sqrt{r^2 + (z + iz_0)^2}$ is the complex radius, G,F,D are the constant coefficients.

Two possible wave processes take place in the system in accordance with the value of the coefficient D in eq. (1). If D=0, the fiber is excited by a topologically neutral beam and symmetric topological dipoles or quadruples [6] appear at the fiber output. (The symmetric dipoles or quadruples represent a system with the same «weights» of positive and negative topological charges.) If $D \neq 0$, there are a topological charged beam at the fiber input.

The Fig.1 shows the case of the topological neutral fiber excitation. The space trajectories were built from the condition: $\mathrm{Re}\left[\Psi(x,y,z)\right] = 0$, $\mathrm{Im}\left[\Psi(x,y,z)\right] = 0$ and characterize the behavior of the symmetric topological quadruple.

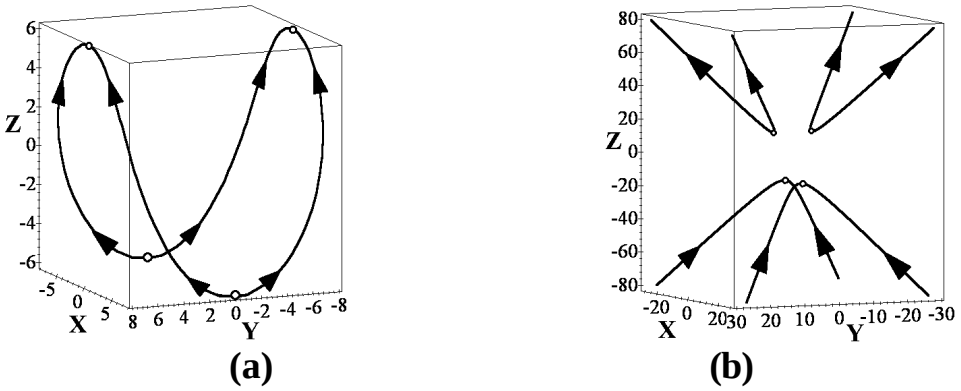

(a) **(b)**

Fig.2. The space trajectories of the symmetric topological quadruple (D=0): (a) F=1, G=3; (b) F=-1,G=2.

The nonparaxial topological quadruple has two types of trajectories. They differ by forms of forbidden or allowed zones. The trajectory in Fig.2a corresponds to the quadruple within allowed zones. At the front wall of the zone, four coupled OVs of the quadruple are born passing through the focal plane. They annihilate at the back wall. There are no OVs outside of the zone.

The opposite case is shown by the space trajectory in the Fig.2b. There is the forbidden zone, at the edges of which the OVs are annihilated or born. There are no OVs inside of the zone.

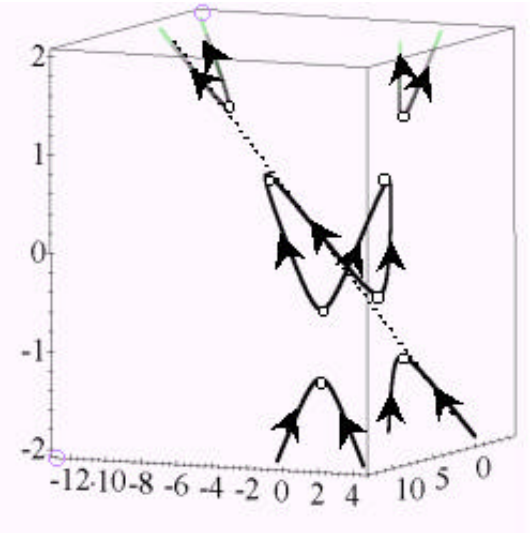

Fig.3. The asymmetric topological quadruple: F=0.5, G=-0.3, D=1.

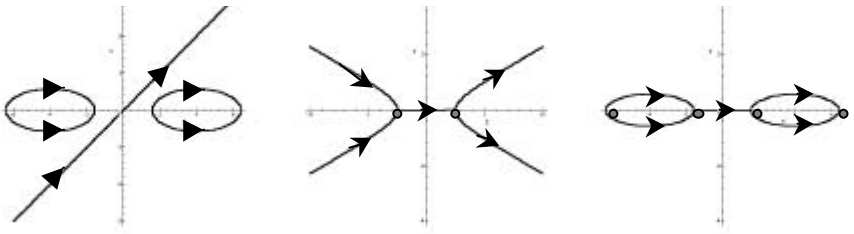

Fig.4.The space trajectories of the asymmetric dipole: (a) the hyperbolic-like trajectory for F=1, G=-1, D=1; (b) the parabolic-like trajectory for F=-0.5, G=-0.1, D=1; (c) the elliptic-like trajectory for F=-1, G=0.1, D=1.

The practical interest presents the case of a topological charged excitation beam ($D \neq 0$). The space curves of the Fig.3 represent the OV behavior of the beam carrying both coupled and free vortices. Similar to the former case there are both forbidden and allowed zones but they exist simultaneously. Besides, the quadruple becomes the asymmetric one. At the front edge of the forbidden-allowed zone, the four OVs are at first annihilated and then born.

However «the weights» of these OVs are unequal. The OV with the topological charge identical to the initial OV is transmitted near the optical axis, whence the rest OVs are forced out far from the optical axis and have a negligibly small «weight» in the vicinity of the focal plane. At the back edge of the forbidden-allowed zone the OVs are at first annihilated and then born. As the singular beam is transmited far from the focal plane, the «weights» of OVs are equalized.

Fig.4 represents other calculated practically interesting situations. It is important to keep in mind that the OV in the asymmetric dipole and quadruple is selected near the focal plane.Therefore, the rest coupled OVs are either annihilated or their «weight» is essentially reduced, and they are forced out far from the optical axis. In any single case, the «parasitic» OVs are suppressed, and information is carried by the useful OV without energy losses. The numerical estimations show that the"distance of life" of the free OV is about some wavelengths at the vicinity of the beam waist.

As a base of the experimental set-up, the device, schematically represented in the Fig.1 from .4.2.2, was used. The main unit of the device was the centered system of two $40^{\times}$ microobjectives fixed on the three-coordinate tables. The microsrew system and the hydraulic arrangement permit us to displace the microobjective along the optical axis and in the transverse directions to within 0.5 μm. As before, the conventional fiber was coiled on a cylinder and excited by a circularly polarized light from the He-Ne laser. Beforehand, the polarized Gaussian beam passes through the optical wedge and converts into an OV. Besides, the signs of the topological charge and the circular polarization form either $|+1,+1\rangle$ or $|-1,-1\rangle$ group. Such adjustment of the initial beam ensures the primary excitation of the CV in the fiber. In order to insure the topologically neutral fiber excitation, it is sufficiently to remove the optical-wedge transparence from the beam.

Concerning the output radiation, the analyzer may be inserted in the beam in order to make better an image contrast. The fundamental Gaussian beam in the reference arm has a circular polarization. The CCD-matrix detector has 512×582 sensible elements recording both the signal beam and the interference pattern. The experimental results are operated by the computer-Pentium 3(800) in real-time scale.

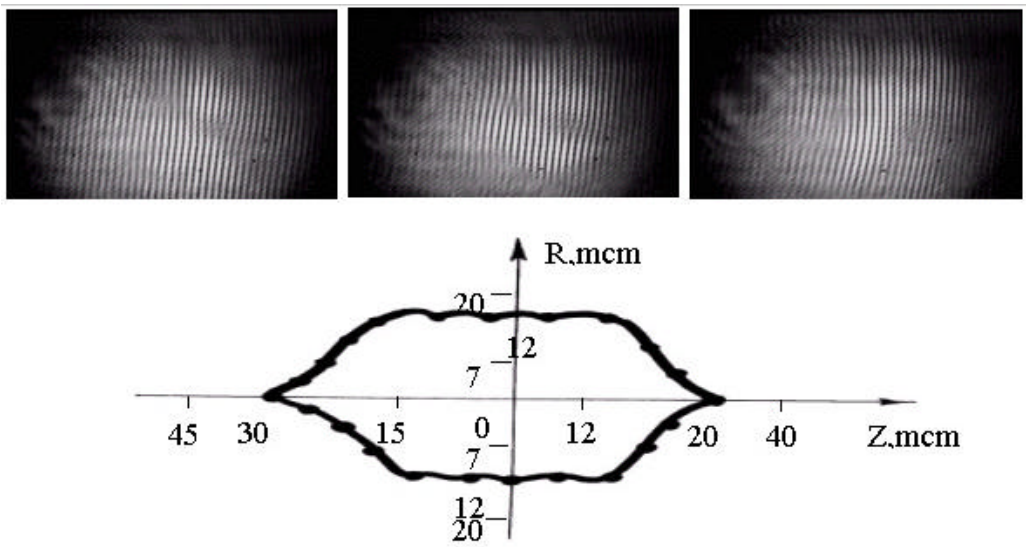

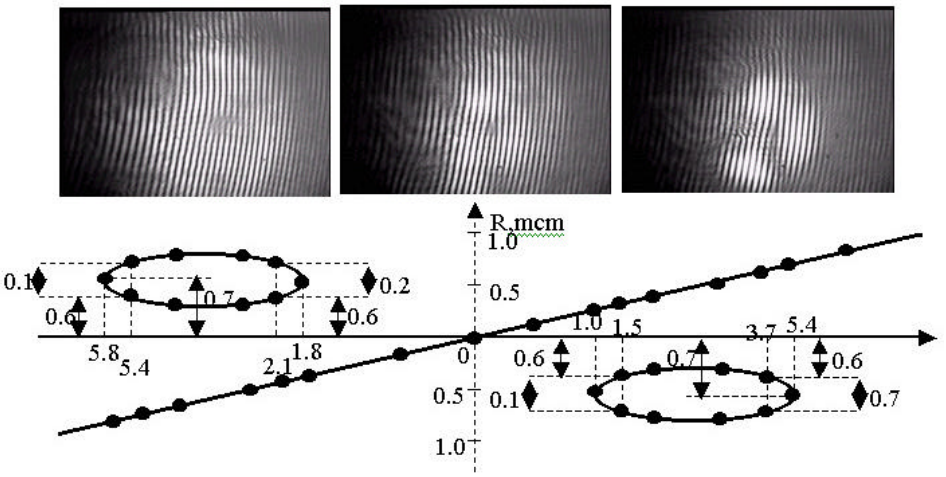

Fig.5. Space trajectories of the coupled and free OVs in the output beam near the focal plane: (a) the topologically neutral initials beam; (b) the topologically charged initials beam.

The radiation after the optical fiber turns out to manifest itself in special way unexpected before. It had been predicted that the beam after the fiber matches completely from the Laguerre-Gaussian modes of free space and propagates to the far field without any structural changes. Our experiments show that such is not the case [7].

We have investigated the evolution the beam intensity distribution with the distance between the observation plane Z (see Fig.1) and the end.of the fiber for two cases, when the incident beam is topologically neutral or charged. The former the latter casesaredepicted in the Fig.5a,b. The upper pictures are the interference patterns with typical fork's positions. It is those positions that represent the bellow curves as the functions of the distance R from the optical axis to the fork and the distance z between the fiber end and the observation plane.

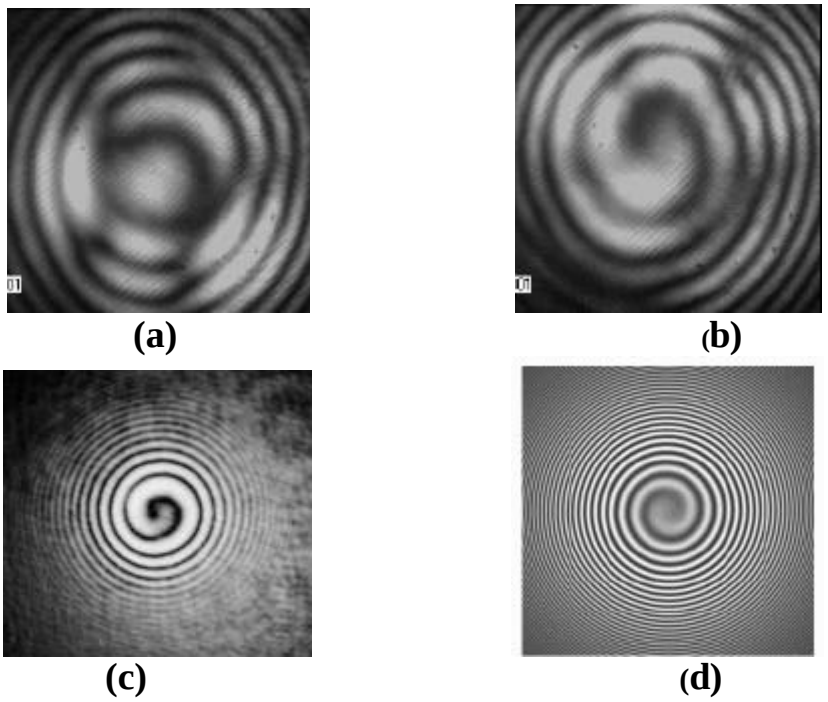

Fig.6. The interference patterns of the symmetric (a) and asymmetric topological quadruples and the recovered OV (c). For comparison the interference spiral of the "ideal" computer-generated OV is depicted (d).

The space curve in the Fig.5a characterizes the positions of the coupled OVs in the topologically neutral beam, The fiber excitation is chosen by such a way that the coupled OVs form the elliptic-like trajectory similar to that depicted in Fig.4c. The form of the trajectory points out existence of the forbidden zone with extension about 50 μm. At its edges OVs are born and annihilated.

A completely different type of the space trajectory occurs in the topologically charged beam (see Fig.5b). Indeed, there are two closed pieces of the curve positioned before and after the focal plane and one straight-line crossing the beam waist. The closed curves are produced by the coupled OVs while the straight line is traced by the free OV. The free OV is located inside the forbidden zone with "life length" about 3 μm. It enables to ensue suppressing of the mode noise in a OVFS without energy losses.

Although the intensity distribution of the recovered field has not an ideal structure of the OV, the interference patterns are near to spiral of the ideal OV. Fig.6 illustrates a typical interference image of the recovered field.

Thus, we have shown that the centered microobjective system placed at the fiber output is able to recover the image of a single OV without energy losses. Similarity of the recovered interference spiral and the ideal one permits to design operating samples of the OVFS on the base of conventional commercial optical fibers.

References

1. N.V. Kukhtarev, A.V. Volyar, A.V. Gnatovsky Polarized phase conjugation and some principles of parallel information transmission by a fiber/crystal system // Nonlinear Optics. 1993. **.2**.,447-464.
2. A.V. Volyar, T.A. Fadeyeva Optics of singularities of a low-mode fiber: I. Circular disclinations// Optics and Spectroscopy. 1998 **.85**., 264-271.
3. A.V. Volyar, T.A. Fadeyeva Optics of singularities of a low-mode fiber: II. Optical vortices// Optics and Spectroscopy, 1998, **85,** 272-280.
4. A.V. Volyar, T.A. Fadeyeva The Topological Multipole Dynamics: 1. High–Order Nonparaxial Singular Beams // Optics and Spectroscopy. 2001. (in press).
5. A.V. Volyar, T.A. Fadeyeva The Topological Multipole Dynamics: 2. Birth, death and evolution of nonparaxial optical vortices // Optics and Spectroscopy. 2001 (in press).
6. M.S. Soskin, M.V. Vasnetsov. // Horizons in World Physics, edited by M. Vasnetsov and K. Staliunas, 1999. V. 228,1-35.
7. Yu. Egorov, A. Alexeyev, 0. Shipulin, A. Volyar, M.Soskin, Birth and Death Events in Topological Multipole Fields after Emitting from an Optical Fiber // SPIE Proc. 2001. (to be published).

4.2.5 Computer processing of the interference spiral

A computer processing of an operative information from fiber-optical sensors, as a rule, is succeeded by operation with numerical data, for example, a total intensity after a sensor [1,2]. At the same time, it is well known that intensity fluctuations of a laser source and other similar reasons cause the greatest errors in operation of a device reducing both accuracy and sensitivity. On the other hand, a destructive effect of the initial intensity variations can be essentially reduced or entirely eliminated by means of processing of an interference image as a whole, by a computer image processing.

The aim of the given section is to develop and to test the computer image processing technique of the angular location of the spiral interference pattern as a whole in a vortex fiber-optical sensor.

The phase shift between singular and reference beams in the ideal case is a linear function of the angular position of the interference spiral. Consequently, optical fiber perturbations caused by external parametric fields (a temperature, a pressure, acceleration, etc.) can be defined by means of the direct measurement of the spiral angular position. Moreover, in contrast to other interference ways this one gives more high operating accuracy and reproducibility of experimental results.

Consider the intensity distribution occurring as a result of the interference between the optical vortex and Gaussian beam as [3]:

$$I = I_1 + I_2 + 2\sqrt{I_1 I_2}\cos(\Phi_1 - \Phi_2), \quad (1)$$

where I_1, I_2 ,Φ_1, Φ_2 are the Gaussian beam and optical vortex intensities and phases, respectively. The interference image looks as bright and dark spirals. Position of the bright curve is defined by the phase difference:

$$\Phi_1 - \Phi_2 = 2mp, \quad (m = 0,1,2\ldots) \quad (2)$$

(for the dark curve, it is $\Phi_1 - \Phi_2 = (2m+1)p$). The Gaussian beam phase is [5]

$$\Phi_1 = kz + \arctan\left(z/z_{0g}\right) + \frac{kr^2}{R_g(z)} + f_{og}, \quad (3)$$

where $R_g(z) = z\left(1 + \frac{z_{0g}^2}{z^2}\right)$ is the wavefront radius curvature, $z_{0g} = \frac{kr_g^2}{2}$ is the Rayleigh length, r_g is the beam waist, f_{0g} is the initial phase.

On the other hand, the OV phase is [4]

$$\Phi_2 = kz + (l+1)\arctan\left(z/z_{0v}\right) + \frac{kr^2}{R_v(z)} + f_{0v} - lj, \quad (4)$$

where $R_v(z) = z\left(1 + \frac{z_{0v}^2}{z^2}\right)$ is the OV curvature, $z_{0v} = \frac{kr_v^2}{2}$ is the Rayleigh length, r_v and f_{0v} are the OV waist radius and initial phase, r, j are the polar coordinates in the observation plane.

From equations (2) – (4) we have

$$\Phi_1 - \Phi_2 = \arctan\left(z/z_{0g}\right) - (l+1)\arctan\left(z/z_{0v}\right) + kr^2\left(\frac{1}{R_g(z)} - \frac{1}{R_v(z)}\right) + f_0 + lj. \quad (5)$$

Since $z=const$ at the observation plane, the equation (5) can be rewritten as:

$$\Phi_1 - \Phi_2 = -ar^2 + b' + lj, \quad (6)$$

where $a = k\left(\frac{1}{R_v(z)} - \frac{1}{R_g(z)}\right)$, $b' = \arctan\left(z/z_{0g}\right) - (l+1)\arctan\left(z/z_{0v}\right) + f_0$.

The equation of equiphase lines on the spiral image can be written as $lj = ar^2 + b_0$ ($b_0 = \Phi_2 - \Phi_1 + b'$). The most simple spiral form being comfortable for the image computer processing ($l=1$) expressed as:

$$j = ar^2 + b_0. \quad (7)$$

We have considered various techniques of the computer processing of spiral images.

The first technique defines the phase difference as the position (r, j) of the intensity minimun along circumference with the given radius (see fig.1).

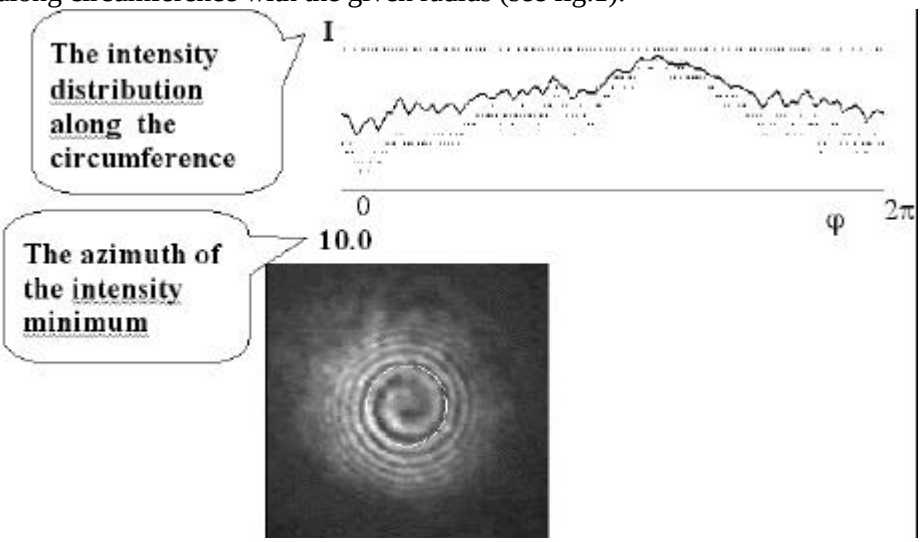

Fig.1. The first technique of the spiral image processing.

The advantage of this technique as against the other ways is the very high rate of the experimental data processing, while its imperfection is the high sensitivity to a local noise.

The second technique defines the angular position of the line with a major minimum intensity obtained as a Moire's pattern.

The Moire's patterns are obtained by subtraction of two interference images: initial and instantaneous. The inversion process is operated relative to the X-axis of the mirror-reflection of the image.

The obtained image has the strongly delineated minimum in a form of the black band (see Fig.2). The theoretical value of this minimum can be defined as follows. Due to a mirror-reflection, the angle j transforms into $-j$ in eq. (6). It corresponds to the sign change of the OV topological charge and the sign of the curvature of the spiral changes too. Mathematically this process is written as:

$$I = I_1 + I_2 + 2\sqrt{I_1 I_2}\cos(ar^2 - lj + f) - \{I_1 + I_2 + 2\sqrt{I_1 I_2}\cos(ar^2 + lj\} \qquad (8)$$

(l=1) or

$$I = 2\sqrt{I_1 I_2}\{\cos(ar^2 - lj + f) - \cos(ar^2 + lj)\} = 4\sqrt{I_1 I_2}\sin\left\{(ar^2 + f)/2\right\}\sin\{lj - f/2\}$$

As it can be seen from the last expression, an axis of the black band turns into the $\frac{f}{2}$ angle relative to X-axis.

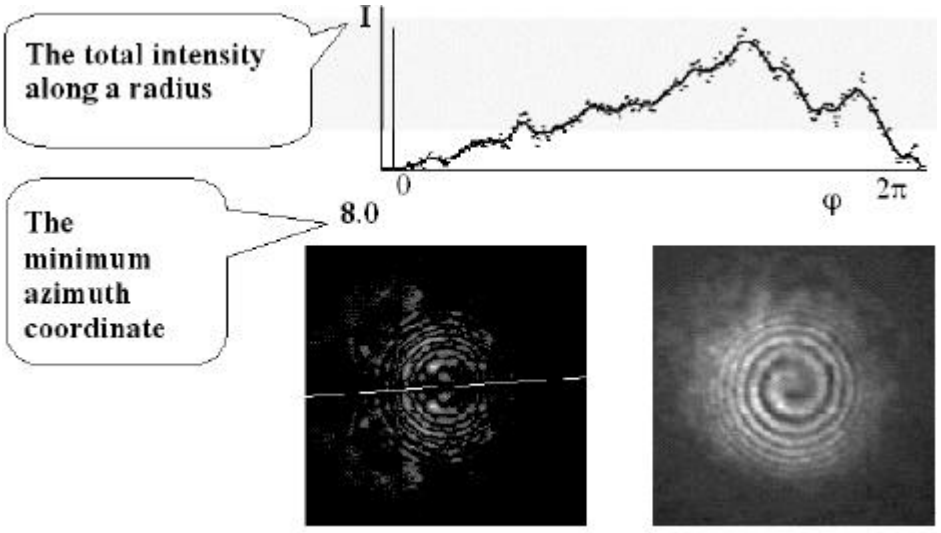

Fig.2. The second technique of the image processing.

The advantage of the given technique as against the first one is the noise diminution at the expense of the intensity averaging-out over the radius. Its imperfection is the large sensibility to any shifts of the spiral center. Deviations of the center's coordinates cause appearance the "fork-like" intensity distribution instead of the clearly delineated straight band (see Fig.3).

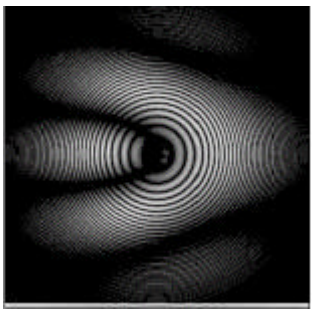

Fig.3. The fork-like image

The third technique defines the phase position φ_0 along the darkest line in the interference image (see. Fig.4).

As the matter of fact, the interference image is constellation of the dark and the bright spirals. The brightness of these spirals is defined by the phase difference between beams on the given curve. Knowing the spiral curvature parameter *a*, we can always define the integral intensity on the given spiral and, consequently, obtain the required phase shift. This technique underlains the experimental measurement of the real phase differences induced by the external parametric fields.

The main advantage of the given technique is the very weak sensitivity to ambient noise due to the intensity integration along the spiral curve. Besides, it has the lesser sensitivity to the determination of the interference spiral center as against the 2-nd way.

In order that these techniques can be realized it is necessary to find coordinates of the interference spiral center. Find "the center of gravity" of the dark and the bright spirals. They are a little bit removed relative to the center of a true image. But "the center of gravity" of the dual spiral is just the sought true center of the all interference pattern.

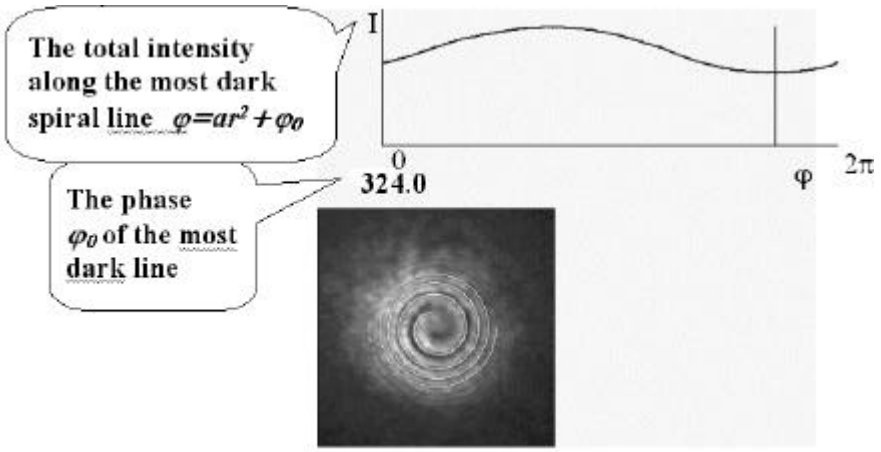

Fig.4. The third technique of the image processing.

For that reasons the next mathematical method was developed. The interference image was scanned along the X- or Y- axes. On the each line, the intensity minimum and maximum were defined. Besides the x_i - and y_i - coordinates of the midst of the most wide interval between the maximum and minimum was found. Then the coordinates the spiral center were expressed as

$$X_c = \frac{\sum_{i=1}^{N} x_i}{N}, \; Y_c = \frac{\sum_{i=1}^{N} y_i}{N}, \tag{9}$$

where N is the number of lines with the most wide interval.

The x_i coordinate of the widest interval is a little removed relative to the true center. However there is any other mirror-symmetric line relative to the true center. Moreover its x_i' coordinate on this interval is removed at the same distance but with opposite sign. The superposition $\frac{x_i + x_i'}{2}$ gives the location of the true spiral center (see Fig.5).

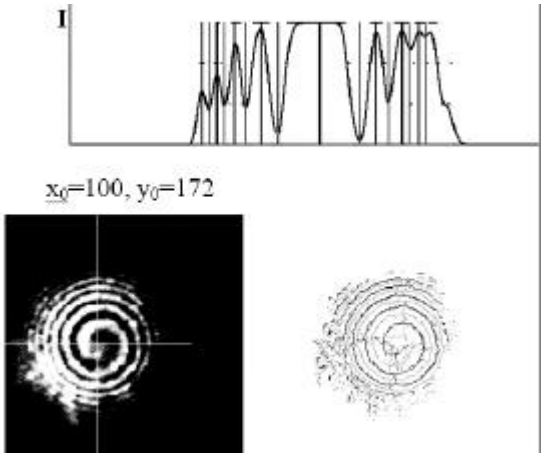

Fig.5. The detecting of the spiral center coordinates.

To realize the third technique [6] it is necessary to find the *a*- parameter of the spiral curvature from the eq.(7). To do that, it can be used the method similar to the 1-st one. Let us change the radius of some ring encircling the spiral center, from $r_{\min}$ to $r_{\max}$. we find the intensity minimum with the azimuth angle j on the each circle. The Fig. 6 shows that dependence $j\ (r^2)$.

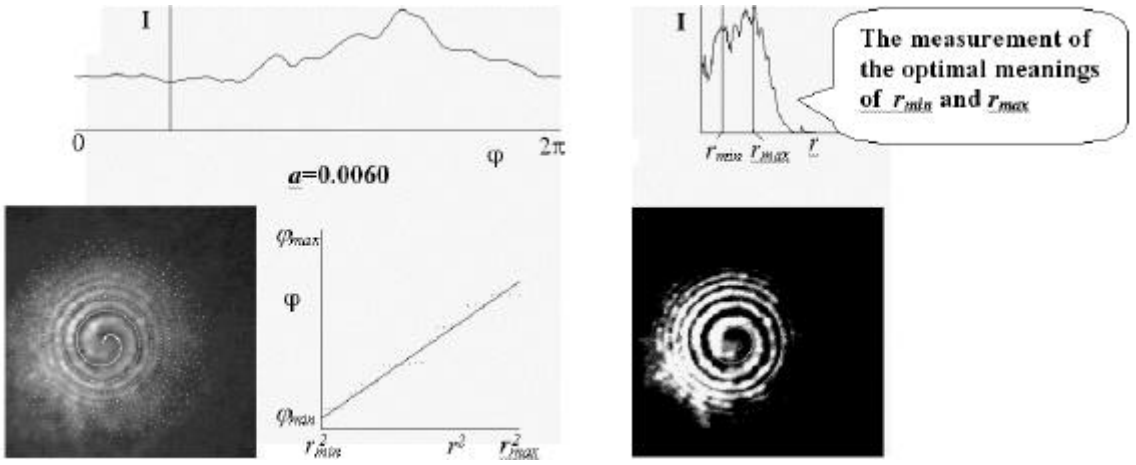

Fig.6. The detecting of the a- parameter of the spiral curvature.

The *a*-parameter of the spiral curvature was found by means of the least-squares method. The *a*- parameter and the spiral curvature *K* are coupled by each other as

$$K = \sqrt{a}\,\frac{\lfloor 4(j - j_0)^2 + 3\rfloor\sqrt{4(j - j_0)}}{\sqrt{[4(j - j_0)+1]^3}}\ .$$

The experimental data as functions of temperature t^oC was obtained on the base of OVFS. The CCD-camera fixs the changes of the interference image. The temperature varies from 18.4 $^{\circ}$Ñ up to 24.6 $^{\circ}$Ñ during 10 min. The temperature variations from one frame to another was $\Delta T \sim 4\cdot 10^{-4}$ $^{\circ}$Ñ. The dependence of the spiral phase on the number of frame (it corresponds to the temperature variations) for the frame succession was computed in concordance with the techniques 1 – 3. The Fig.7 represents these results for the techniques 1 – 3. The obtained dependence was approximated by the linear function $y=ax+b$. Further, the standard deviation was defined as $\Delta = \sqrt{\dfrac{\sum_{i=1}^{n}(y_i - y)^2}{n(n-1)}}$. Values of the parameters a, b, Δ are represented below the curves.

The comparison of these curves shows that the best accuracy, linearity and also the least deviation corresponds to the third method.

To process the interference image in a real-time scale, we have developed the specific computer program adopted to DELPHI-5, what enables us to realize the image processing of one frame during 0.4 c in according to the third technique (see Fig.8). For the beginning, the program defines the coordinates of the spiral center and the curvature parameter *a* averaged over 10 frames (see Fig.8a). Provided their mean square is more than 10%, the process is repeated until these values will be 10% or less to eliminate ambient noise hindrances exceeding a given threshold. Further, an angular position of the spiral is viewed on the TV monitor graduated in terms of temperature (see Fig.8b).

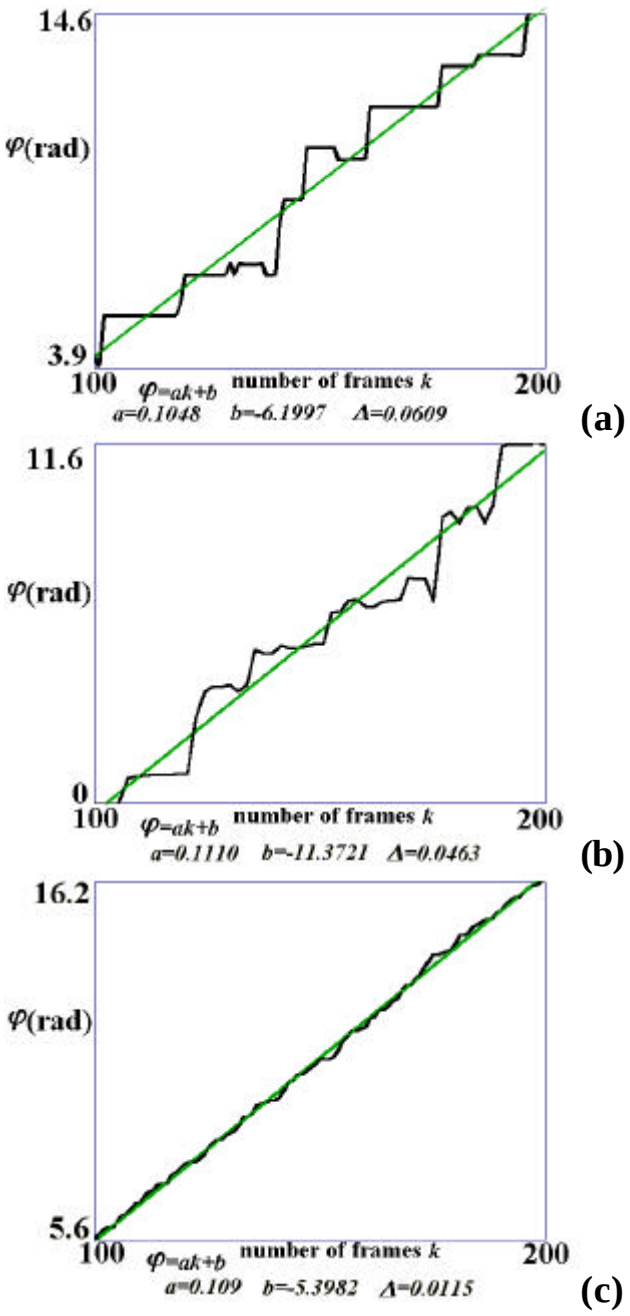

Fig.7. The dependence of the spiral phase on the number of frames

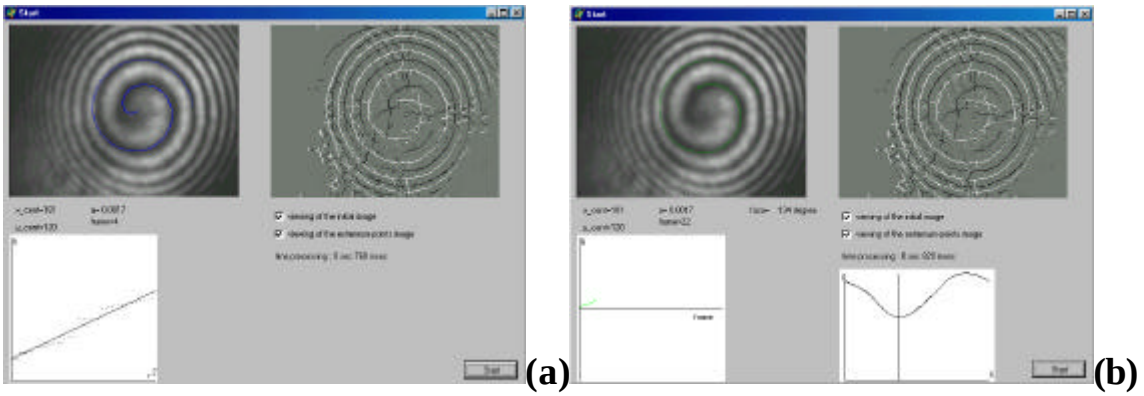

Fig.8. View of the operating windows of the computer processing: (a) processing of the spiral's parameters, (b) processing of the image angular position

Thus, we have developed and compared three techniques of the computer image processing for the OVFS. It was shown that the third technique, i.e. determination of the angular position along the dark line in the interference image has been employed as most optimal. The developed technique permits to process a spiral interference image in a real-time scale during 0.4 c per one frame. The accuracy of the temperature measurement is up to 0.012 rad in the angular scale.

REFERENCES

1. A.L. Harmer Principles of optical instrumentation, Measurement and Control, **15**, 143-151. (1982).
2. T. Okosi, K. Okamoto, T. Okosi, K. Okamoto, M. Otcu, H. Nisihara, K. Kyuma, K. Xarate, "*Fiber-optic sensors*" Leningrad: Energoatomizdat, (1990) 256 p.
3. M. Born, E. Wolf, "*Principles of optics*", Oxford, Pergamon press, 1963.
4. S. Solimeno, B. Crosignani, P. DiPorto, *"Guiding, diffraction and confinement of optical radiation*" Orlando, Acadimic press, Inc., 1986.
5. I.V. Basisty, V.Yu. Bazhenov, M.S. Soskin, M.V. Vasnetsov, "Optics of light beams with screw dislocations/", *Optics Comm.*, V.103, p.422-528, 1993.
6. T. Fadeyeva, D.Kurabtzev, A. Volyar, M. Soskin Computer Processing of Fiber – Vortex Sensor Data // SPIE Proc. 2001. (to be published).

4.2.6 Design and assessment of one-arm OVFS

The main problems with two-arm interferometers such as, for example, a single-mode Mach-Zehnder interferometer configuration, are attributed to the noise, especially instability and spurious phase shifts. The one-arm interferometric configuration holds undoubted advantages in this point. The fact is that the interfering modes transmitting through the same fiber possess exactly the same ambient perturbations. The only distinction appears due to a different response of the mode propagation constants to temperature deviations.

The aim of the given section is to study theoretically and experimentally the optical properties of the one-arm OVFS on the base of the guided OV and to carry out its assessment.

As it was mentioned above, the main guided modes in a fiber are CV, IV and $HE_{11}^{\pm}$ wave fields with circular polarization [1,2]. In contrast to the CV mode, IV one manifests itself as the wave superposition of the azimuthall-symmetric TE_{01} and TM_{01} modes. The "weights" of these modes are defined by the excitation conditions and they can be strongly specified at the fiber input. The IV mode being broken up into the eigen-modes may change both the topological charge and the sign of its circular polarization.

Consequently, the circular polarization analyzer at the fiber output can suppress the CV mode and $HE_{11}^{\pm}$ mode, but not the IV mode.

Let us suggest that the $H\,E_{1\,1}^{\,+}$ mode and CV, IV modes are simultaneously excited at the fiber input. The wave function has a form $\boldsymbol{Ø} \Rightarrow A \cdot CV_{+}^{+} + B\,IV_{-}^{+} + C\,HE_{11}^{+}$ or

$$\boldsymbol{Ø} = \{A\begin{pmatrix} \exp(+ij) \\ 0 \end{pmatrix}\exp(i[\tilde{b} + db_{CV}]z) + B\begin{pmatrix} \exp(-ij)\cos\Delta bz \\ i\exp(ij)\sin(\Delta bz) \end{pmatrix}\exp(i[\tilde{b} + \Delta b]z)\}\,F_1(R)$$

$$+ C\begin{pmatrix} 1 \\ 0 \end{pmatrix}\exp(ib_{HE}z)\,F_0(R), \qquad (1)$$

where $F_{1,0}(R)$ is the function of the field profile, $R = \frac{r}{r}$, $\tilde{b}$ is the scalar propagation constant of the CV or IV modes, db_{CV} is the polarisation correction to CV mode, $\Delta b = \frac{db_{TM} - db_{TE}}{2}$, $db_{TM,TE}$ are the polarisation corrections for TE and TM modes, b_{HE} is the propagation constant of HE_{11} mode, *A*, *B* and *C* are constant coefficients.

If the beam after the fiber and and circular analyser loses the left-hand polarisation, the zero-intensity point moves according eq.(1):

$$\{\exp(ij) + G\exp(-ij)\cos\Delta b\,\exp(idb\,z)\}F_1(R) + F\exp(idb_0 z)F_0(R) = 0, \qquad (2)$$

where $db_0 = b_{HE} - \tilde{b} - db_{CV}$, $db = \Delta b - db_{CV}$, $G = \frac{B}{A}$, $F = \frac{C}{A}$.

Let us consider three possible cases.

1) The CV and HE_{11}^{+} modes are excited in the fiber only. Then

$$j = p + db_0 z, \quad F_1(R) + FF_0(R). \qquad (3)$$

It means that the OV center traces a circular line. The angular position of the amplitude zero depends both on the distance z and the difference db_0 between the propagation constants. The temperature sensitivity of the angle position of the zero point is

$$\frac{\Delta j}{\Delta T} = z\frac{\partial(db_0)}{\partial t} + db_0\frac{\partial z}{\partial t}, \qquad (4)$$

or

$$\frac{\Delta j}{L\Delta T} \approx \frac{\partial(db_0)}{\partial t} + db_0 a, \qquad (5)$$

where $n(t) = n_{co}(1 + a\,t)$, $z = L(1 + a\,t)$ and $a \propto 10^{-5}$ *ãðàä*$^{-1}$ typically. Besides, we suggest that field frequency is near the cut-off frequency of the fiber. Then, the transverse waveguide parameter ***U*** is [3]:

$$\tilde{U} = V\exp(-\frac{1}{V}) \approx 2{,}4\exp(-\frac{1}{V}). \qquad (6)$$

At the same time, $b = kn_{co}\left(1 - 2\Delta\frac{U^2}{V^2}\right)$ and the propagation constant of the HE_{11} mode is

$$b_0 \approx kn_{co}(1 - a\,t)\left[1 - 2\Delta(2{,}4)^2\frac{\tilde{V} - 1}{\tilde{V}^2}\left(1 + 2\frac{a\,t}{\tilde{V}}\right)\right], \qquad (7)$$

where $V \approx \tilde{V}(1 + a\,t)$.

On the one hand, the CV vortex has $\tilde{U}_{CV} \approx V$ and

$$b_{CV} \approx \tilde{b} \approx kn_{co}(1 - 2\Delta), \qquad (8)$$

or

$$db_0 \approx kn_{co}(2\Delta)\left\{1 - (2{,}4)^2\frac{\tilde{V} - 1}{\tilde{V}^2} - \left[1 + (2{,}4)^2\frac{(\tilde{V} - 1)(\tilde{V} - 2)}{\tilde{V}^3}\right]a\,t\right\}. \qquad (9)$$

Consequently, the temperature sensitivity is defined as

$$\frac{\Delta j}{L\Delta T} \approx 4a\ k n_{co}\Delta\left[1+3\frac{\left(\tilde{V}-1\right)\left(\tilde{V}-2\right)}{\tilde{V}^3}\right]. \qquad (10)$$

On the other hand, it can be considered that $2a\ k\Delta \propto 1$ and $\frac{\Delta j}{L\,\Delta T} \approx 4\frac{\partial \grave{a}\ddot{a}}{\grave{\imath}\ \tilde{a}\eth\grave{a}\ddot{a}}$ for V=3.

It means that a heating of one-meter fiber by $1^o C$ rotates the intensity zero on 1, 27 turn around an optical axis.

2) All three modes propagate along a parabolic-index fiber. Then $\Delta b = 0$ [1,3] and thetrajectory ofzero is

$$x = -\frac{F}{G+1}\cos b_0 z,\quad y = \frac{F}{G-1}\sin b_0 z. \qquad (11)$$

Thus, the vortex trajectory has an elliptic form with semiaxes $a = \frac{F}{G+1}$, $b = \frac{F}{G-1}$. The temperature sensitivity does not change compared with the first case.

3) All three modes propagate along a step-index fiber. The polarization correction of the CV is [3]

$$db_{CV} = -\frac{(2\Delta)^{3/2}}{r}\frac{WU^2}{V^3}\frac{K_1(W)}{K_0(W)}, \qquad (12)$$

where $K_n(x)$ is the McDonald function.

In order to take into account the temperature changes of the polarization correction, one assumes that $U \approx U_{\hat{e}\partial} + (2\Delta)^{1/2}\Delta V$, where ΔV the detuning of U relative to the cut-off frequency. Besides, $K_0(W) \approx -\ln W + (\ln 2 - g)$, $g \approx 0{,}58$, $K_1(W) \approx 1/W$ and $W \approx \sqrt{2V\Delta V}$. Whence,

$$db_{CV} \approx 2\frac{(2\Delta)^{3/2}}{rV}\frac{1}{\ln(2V\Delta V)}. \qquad (13)$$

and

$$\Delta b = -\frac{(2\Delta)^{3/2}}{2r}\frac{WU^2}{V^3}\frac{K_1(W)}{K_2(W)}. \qquad (14)$$

But $K_2(W) \approx \frac{2}{W^2}$, consequently $\Delta b \propto W^2 \to 0$.

Assuming that $F_1 = \mathrm{Re}\,xp(-1/2VR^{2)}$ è $F = \exp(-1/2VR^{2)}$ one finds the trajectory's equation:

$$x = -\frac{F}{G\cos db_{CV} z + 1}\cos db_0 z,\qquad y = \frac{F}{G\cos db_{CV} z - 1}\sin db_0 z \qquad (15)$$

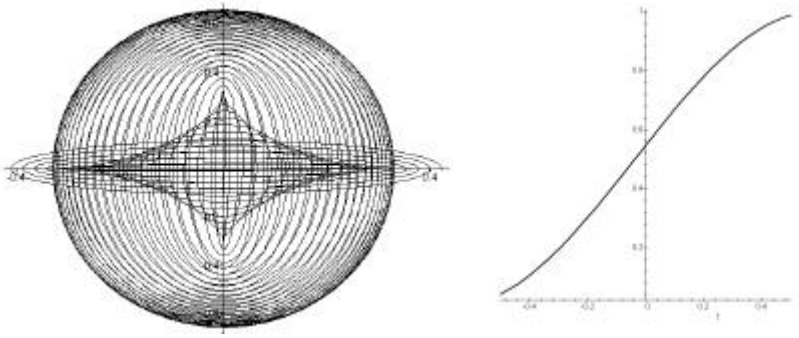

(a) **(b)**

Fig.1. The trajectories of OV in the temperature sensor at: (a) F=1, G=3, $\Delta t = 1^{o}C$, z =100 m. The dependence of the angular position j on temperature at F=1, G=0.1, z = 0.3 m (b).

The variable amplitudes in eq.(15) point to a precession movement of the OV trajectory. Provided $db_0 >> db_{CV}$ and G<<1, the temperature sensitivity will be really the same as in the first and second cases. The Fig.1 and Fig.2 show the OVs trajectories and the intensity distribution as function of temperature.

The s temperature sensitivity defined from Fig.1b is about $\frac{\Delta j}{L\Delta T} \approx 3.3\frac{rad}{Km}$ and has a good agreement with the obtained result for the first case.

The experiment is brought about by means of the set-up with the single interferometric arm. The input and output ends of the fiber are positioned on the three-coordinate tables. The laser spot at the plane of the fiber input was controlled up within 0.5 μm and observed by the reflected light microscope.

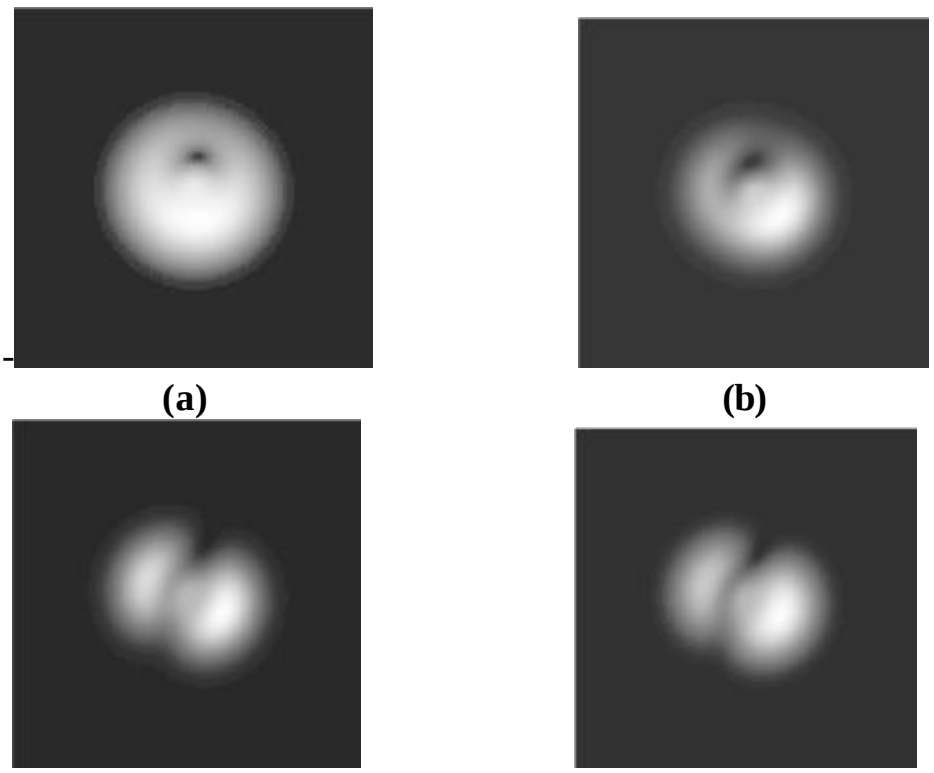

(a) **(b)**

(c) **(d)**

Fig.2. The intensity distribution of the mode field viewed at the different temperature values: $25^{o}C$ (a,c) and $26^{o}C$ (b,d), respectively: G =0.2, F =1 (a,b); G =1, F =1 (c,d)

The low-birefringent fiber was made by CVD method and consists from GeO_2 / SiO_2 core, the B_2O / SiO_2 cladding and the silica substrate. It had the circular geometry with the core radius r =3.4*mm*. The linear birefringence was less than 10^{-6}. This fiber was designed to be single-mode at l = 0.85 μm but the experiments were performed at 0.*63 mm* wavelength region where the fiber guides three waves: HE_{11} mode, CV_{01} and IV_{01} vortices. The length 30-m section of the fiber was looped in several loose coils and was placed in a temperature controlled water bath. The output fiber end was magnified by the $20^{\times}$ microobjective, recorded by the CCD-matrix with 512×582 sensible elements and viewed on the TV monitor to be processed by the computer - Pentium 3 (800). The angular positions of the zero intensity in the field image was measured as a function of temperature

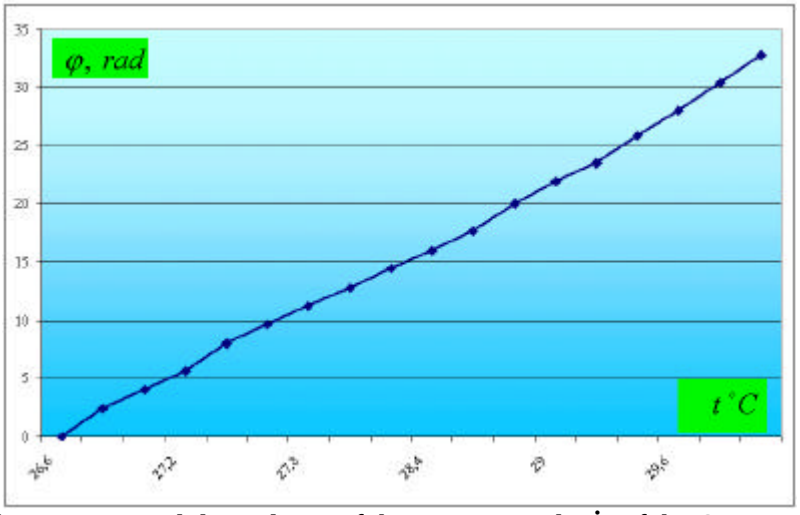

Fig.3. The experimental dependence of the rotation angle j of the OV center on the temperature $t^{o}C$. The experimental accuracy is about 1.5%, the fiber length is 30 m.

The circular analyzer placed after the fiber output suppresss partially the «parasitic» noise inserted by the IV mode. The value of the noise suppression was about 20 dB.

The Fig.3 demonstrates the experimental curve of the temperature sensitivity. The sensitivity of the device can be seen to be a linear function of the temperature at least at the range from 20 to $40^{o}C$ the measured temperature sensitivity is about $1.03\frac{rad}{Km}$ and in good agreement with the represented above theoretical estimations. The reproducibility of the experimental results for different pieces of the given fiber is about 3.4%.

References

1. A.V. Volyar, T.A. Fadeyeva Optics of singularities of a low-mode fiber: II. Optical vortices// *Optics and Spectroscopy*. V.85. No.2, p.272-280 (1998).
2. K.N.Alexeyev, T.A. Fadeyeva, A.V.Volyar, M.S. Soskin. Optical vortices and the flow of their angular momentum in a multimode fiber// *Semiconductor Physics, Quantum Electronics & Optoelectronics.* V.1. No.1, p.1-8. (1998).
3. 3. A.W. Snyder, J.D. Love. Optical Waveguide Theory. London-New York, Chapman and Hall, 1983.

4.3 Optical-vortex pulses in OVFS

4.3.1 General analysis

Behavior of the OV pulses in a fiber inserted to an interferometer is the subject of the peculiar attention due to special properties of the interferometric sensor. At the same time this problem has not been yet studied.

The aim of this paragraph is to give the theoretical estimation and computer simulation of a pulse OV propagation in an optical fiber without perturbations.

Consider a quasimonochromatic pulse in the form

$$E(t,r) = E_0 \exp\left(-\frac{t^2}{T_0^2}\right)\exp(-i\,w_0\,t)F(r). \qquad (1)$$

Here $F(r)$ is a profile function of the beam, $r = \sqrt{x^2 + y^2}$, T_0 is the pulse duration, E_0 is the amplitude, w_0 is the central frequency.

The spectral decomposition of the beam gives

$$\tilde{E}(w) = \int_{-\infty}^{\infty} \exp(iwt')E(t')dt', \qquad (2)$$

or, taking into account (1)

$$\tilde{E}(w,r) = E_0 F(r)\sqrt{\frac{p}{T_0}}\,\exp\left(-\frac{(w-w)^2}{n_0^2}\right), \qquad (3)$$

where $n_0 \equiv \frac{1}{T_0} << w_0$.

Thus, the spectral distribution has a form of a narrow peak in the vicinity of w_0 with the bandwidth n_0.

Let us take that the pulse comes to the fiber input. Naturally, it excites the whole mode spectrum. If the only guided OV is excited in the fiber then the wave field propagating along the fiber is

$$E = C(w)E(t,r,z)\exp(ib_w z - iwt), \qquad (4)$$

where $b_w = b_w(w)$ and

$C(w) = \sqrt{\frac{p}{T_0}}\,\exp\left[\frac{(w-w_0)^2}{2n_0^2}\right]$. The fiber field at the point z at moment *t* equals

$$E(t,r,z) = \frac{1}{2p}\sqrt{\frac{p}{T_0}}\int_{-\infty}^{\infty} dw \exp\left[-\frac{(w-w_0)^2}{2n_0^2}\right]\exp(ib(w)z - iwt)F(r). \qquad (5)$$

Because the interval is very narrow, the range $2n_0$ is cut out from the all integration area. Since, we can write

$$b\,(w) \approx b\left(w_0\right) + b'\left(w_0\right)\left(w - w_0\right) + \frac{1}{2} b''\left(w - w_0\right)^2 + \ldots . \qquad (6)$$

After the integration of (5) by the Laplace method we obtain

$$E\left(t,r,z\right) \approx \frac{E_0}{\sqrt[4]{1+\frac{z^2}{L_D}}} \exp\left\{ - \frac{\left(t - \frac{z}{v_g}\right)^2}{T_0^2\left(1+\frac{z^2}{L_D^2}\right)2} \right\} - \exp\left\{ i \frac{\left(t - \frac{z}{v_g}\right)^2}{T_0^2\left(1+\frac{z^2}{L_D^2}\right)} z - \frac{i}{2} \arctan\frac{z}{L_D} \right\} F(r)\,, \quad (7)$$

where $L_D = \frac{T_0^2}{4D}$, $D = \frac{1}{2}\frac{d^2 b(w)}{dw^2}\Big|_{w=w_0}$, $v_g^{-1} = \frac{d\,b\,(w)}{dw}\Big|_{w=w_0}$. Here v_g is the group velocity of the pulse and the constant D characterizes the pulse broadening [1] in the fiber.

In order to estimate the pulse broadening and the group velocity of a fiber OV let $dt_j = 2\frac{z\,n_{co}}{c\;w} DV\Delta dw$. However $d\,t_j = \left(\frac{d^2 b_j}{dw^2}\right) dw$ since we find $D = \frac{1}{2}\frac{d^2 b}{dw^2} \approx \frac{n_{co}}{cw}\tilde{D}V\,\Delta$, where n_{co} is the refractive index of the fiber core, Δ is the height of the refractive index profile, V is the waveguide parameter: $V^2 = U^2 + W^2$, U and W are the core- and the clad- waveguide parameters, respectively. Besides, the group velocity is evaluated for a step-index fiber as [2]

$$v_g \approx \frac{c}{n_{co}} \left\{ 1 + \Delta \frac{U^2}{V^2} \left[1 - 2 \frac{K_l^2(W)}{K_{l-1}(W)\,K_{l+1}(W)} \right] \right\} \qquad (8)$$

and $l \geq 1$, $K_l(W)$ is the McDonald's function.

For the typical low-order CV in the step-index fiber with V=5, we have D=-0.01, U=3.15, W=3.9, $T_0 = 10^{-8}$ c, $n_{co} = 1.48$, $n_{cl} = 1.46$, $\Delta = 0.014$, $l = 0.63$ μm, whence $D \approx 1.16 \times 10^{-27} \frac{c^2}{m^2}$, $v_g \approx 2.07 \times 10^8 \frac{m}{s}$ and $L_D \approx 8.6 \times 10^{10}\, m$. Consequently, not very short pulses have $\frac{z}{L_D} \approx 0$.

At the OVFS output the wave field is the sum of the signal E_S and the reference E_R beams:

$$E_S \propto E_0 \exp\left(- \frac{\left(t - \frac{z_S}{v_g}\right)^2}{T_0^2} \right) F(r) \exp\left(-iw\,t\right),\; E_R \propto E_0 \exp\left(- \frac{\left(t - \frac{z_R}{c}\right)^2}{T_0^2} \right) F(r) \exp\left(-iw\,t\right), \quad (9)$$

where z_S, z_R are the lengths of the signal and the reference arms.

The total field intensity at an observation plane is written as

$$I \propto \left|E_S + E_R\right|^2 \propto E_0^2 \Big\{ \exp\left(-2\frac{\left(t-\frac{z_S}{c}\right)^2}{T_0^2}\right) + \exp\left[-2\frac{\left(t-\frac{z_R}{v_g}\right)^2}{T_0^2}\right] +$$

$$2\exp\left(-\frac{\left(t-\frac{z_S}{c}\right)^2}{T_0^2}\right)\exp\left(-\frac{\left(t-\frac{z_R}{v_g}\right)^2}{T_0^2}\right)\cos\left(\Delta(b\,z)+l\,j\right)\Big\}F(r), \qquad (10)$$

where j is the azimuth angle, $\Delta(b\,z) = b_0 z_S - k\,z_R$.

As it can be seen from (10), two processes affect the pulses and the interference pattern. The first process is defined by difference of time of the pulses propagation through the interferometer arms. The second process is the frequency dispersion. As the result, the image contrast of the interference patterns diminishes.

To evaluate the image contrast let us pass to dimentionless variables:

$$t = \frac{t}{\sqrt{2}\,T_0}, \quad z_0 = v_g T_0 \approx 2.7\,m, \quad z_R = \sqrt{2}\,\frac{z_R}{z_0}, \quad z_S = \sqrt{2}\,\frac{z_S}{z_0}$$

It should be taken into account that the photodetector records time-avereged value. In our case, the pulse duration T_0 is time of averaging. Consequently, the observed intensity distribution will be:

$$\langle I\rangle = \langle I_S\rangle + \langle I_R\rangle + \langle I_{RS}\rangle\cos\left[\Delta(b\,z) - l\,j\right], \qquad (11)$$

where $\langle I_S\rangle = \frac{1}{2}\sqrt{\frac{p}{2}}\left\{erf\left(\sqrt{2}-z_S\right)+erf\left(z_S\right)\right\}F(r)$,

$$\langle I_R\rangle = \frac{1}{2}\sqrt{\frac{p}{2}}\left\{erf\left(\sqrt{2}-z_R\right)+erf\left(z_R\right)\right\}F(r),$$

$$\langle I_{RR}\rangle = \sqrt{\frac{p}{2}}\left\{erf\left[\sqrt{2}-\frac{1}{2}\left(z_R+z_S\right)\right]+erf\left[\frac{1}{2}\left(z_R+z_S\right)\right]\right\}\exp\left[-\frac{1}{4}\left(z_R-z_S\right)^2\right]F(r).$$

Thus the image contrast is

$$\mathrm{K} = \frac{I_{\max}-I_{\min}}{I_{\max}+I_{\min}} = \frac{\langle I_{RS}\rangle}{\langle I_R\rangle+\langle I_S\rangle}, \qquad (12)$$

where $I_{\max}$ and $I_{\min}$ are the maximum and minimum intensities of the interference image respectively.

The Fig.1 illustrates the evolution of the intensity distribution of caused by interference oftwo OV-pulses transmited through the two-arm interferometer. (The patterns of the Fig.1 are depicted in accordance with equations (10), (11)). The interferometric sensor is tuned to the zero-order band when the only dark straight line is observed. The angle direction of the line is proportional to the phase shift between the beams.

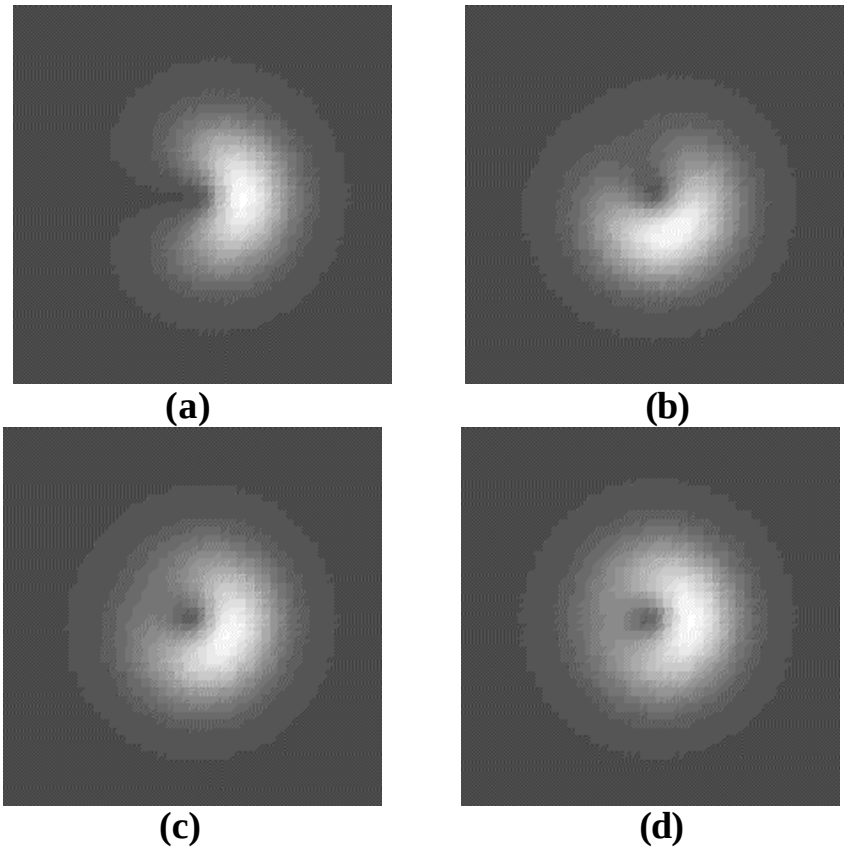

Fig.1. The intensity distribution in after interference of two OV pulses at he output of the two-arm OVFS: (a) $z_S = 1,\ z_R = 1$; (b) $z_S = 2,\ z_R = 1$; (c) $z_S = 2.3,\ z_R = 1$; (d) $z_S = 2.5,\ z_R = 1$.

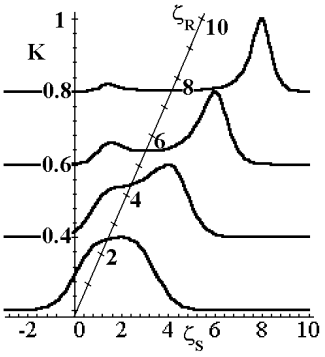

Fig.2. The dependence of the image contrast K on the dimensionless length z_S and z_R of the interferometer arms.

As the difference between the beam's optical paths increases, the image clarity sharply reduces and practically vanishes at $z_S = 2.5,\ z_R = 1$. In fact, the interference band is spread. It corresponds to the following optical path ratio $L_S / L_R = 2.5$. The clarity increases with increasing the pulse duration T_0.

It is convenient to characterized the clarity by means of the image contrast defined by Eq. (12).The Fig.2 represents the set of curves describing the dependency of the image contrast on the dimensionless z_S and z_R parameters. Negative or positive z_S-values corresponds to advancing or delaying of pulses relative to one another. The behavior of the contrast curves shows that

increasing the phase shift between the beams and decreasing the pulse duration causes the spreading of the interference image. The sharp peaks on the curves at the small phase differences are gradually reduced at the expense of either the optical path increasing or the pulse duration decreasing and they can not essentially effect the interference pattern quality.

Thus, employment of short-laser vortex-pulses in two-arm interferometric sensors is not efficient. Indeed, there exist two main optical processes, which destroy an interference pattern in the OVFS. The first process is affected by advancement or retardation of pulses relative to one another so that their contours are partially overlapped or are not overlapped at all. The second process is associated with the broad spectrum of monochromatic waves that corresponds to any short pulse. Both these reasons cause the scrambling of isolated interference patterns, and aggravation of the image quality.

References

1 G.P. Agraval.. Nonlinear Fiber Optics. Academic Press INC, New York, London, 1989.
2. A.Snyder, J.Love. Optical Waveguide Theory. Chapman and Hall, London, New Jork, 1983.

4.3.2 Super sensitive one-arm OVFS

In the work [1] the problem on a super sensitive temperature measurement by means of an one-arm fiber-optic interferometer on the base of the fundamental HE_{11} eigen mode of a single mode fiber has been discussed. That temperature sensor represents a system consisting of a single mode fiber at the ends of which two special mode couplers are fitted. The only linear polarized light component passes through the single mode fiber if an electrical vector of an input beam is oriented along a main fiber axis. The first coupler divides the initial linearly polarized mode between the two linearly polarized ones. The second coupler combines these modes yielding the mode polarization interference. The fiber excitation is brought along by a tungsten lamp with a broadband of a light spectrum. Light emitted from the fiber output is analyzed by a spectrograph. As the authors point out this fiber sensor has a temperature resolution of $3\times 10^{-3}\ ^{o}C$ for a wide temperature range.

The first, it should be noticed that the above mentioned sensor is unstable one to any slight perturbation. Indeed the single mode fiber in this device is excited by a broadband light source (a tungsten lamp). But a single mode fiber is known to have a cut-off frequency for high-order modes at V = 2.4, where $V = \frac{2p}{l} r\sqrt{n_{co} - n_{cl}}$ - the waveguide parameter, l is a wavelength, r is a fiber core radius, n_{co}, n_{cl} - refractive indices of a core and a clad, respectively. Besides, a light beam with a wavelength less then the cut-off wavelength l_C excites high-order modes in the fiber. The authors make use of the F-SPV birefringence optical fibers that have the critical wavelength $l \approx 0.85mm$. In these fibers the $HE_{11,} HE_{21}$ even and odd, TE_{01} and TM_{01} modes are realized at the wavelength $l = 0.74mm$ at which the authors worked. Any slight perturbation of the fiber means as causing an energy mode conversion that changes the light spectrum and to induce a mode noise.

The second, the mode polarization couplers at the fiber ends are deformed due to boiling or cooling and change the mode transformation value. It causes a mode noise as well.

The aim of the given section is to study the new fiber-optic sensor on the base of an optical vortex devoid of the above mentioned deficiencies.

The main idea is as follows. If the optical fiber excites the light beam with a topological charge *l* and a circular polarization s having different signs, there are born three mode types in the fiber, namely a steady CV vortex, an unstable IV vortex and a fundamental $HE_{11}^{(s)}$ mode. The CV vortex and $HE_{11}^{(s)}$ mode have the same polarization state as the initial light beam while the

polarization state of the IV vortex may be changed. The circular polarization analyzer separated a circular polarized light gets to fit at the fiber output. This analyzer suppresses one of circular polarizations. Let the analyzer will be tuned in the IV mode polarization. Then the CV and HE modes are suppressed and the IV vortex turns out to be the work wave. As the matter of fact that the IV vortex is a sum of symmetric TE_{01} and TM_{01} modes transmitting with different phase and group velocities. In fact, we are concerned with two arms interferometer but its two arms are combined into one directed line - an optical fiber. It should be worth noted that our method in contrast to the previous one is not needed the special birefringence fiber types but it can be used an ordinary commercial optical fiber.

Consider this method in detail. The wave function of the light field after passing through the fiber and the circular polarization analyzer is

$$\Psi^{(-)} = \Psi_0(l)\exp(-j)\sin\left(\frac{\Delta b(l)}{2}z\right)\exp\left(ib\tilde{z}\right)F(r), \qquad (1)$$

where the optical fiber is suggested to be excited by a right-hand circularly polarized optical vortex with the topological charge *l=1*; the analyzer cuts off the right-hand circular polarization while the left-hand polarized light component passes through it without losses. The sign (-) means a left-hand circular polarization, $\Delta b = \frac{db_{TM} - db_{TE}}{2}$, $\tilde{b}$ is a scalar propagation constant, db_{TM} and db_{TE} are polarization corrections to the scalar propagation constant $\tilde{b}$, $F(r)$ is a field profile function, $\Psi_0(l)$ is the input intensity; the light field propagates along z-axis.

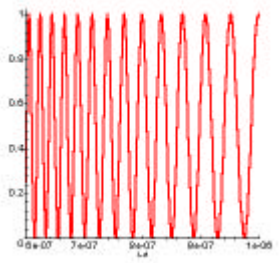

Fig.1. The spectral response $S(l)$ of the optical fiber with IV vortex, $\Delta\tilde{n}_0 \approx 10^{-9}$, z =1 m.

In a general case the difference of the polarization correction for the TM and TE modes may be written in terms of the effective refractive indices $\Delta\tilde{n} = n_{TM} - n_{TE}$ in the form

$$\Delta b = \frac{2p}{l}\Delta\tilde{n}(l) \qquad (2).$$

The dependency $\Delta\tilde{n}$ on a wavelength l is suggested as being far off absorption bands and to be described by the phenomenon of a normal material dispersion.

The spectral response of the optical fiber is

$$S(l) = \frac{|\Psi(l)|^2}{|\Psi_0(l)|^2} = \cos^2\left(\frac{p}{l}\Delta\tilde{n}(l)z\right)F^2(r). \qquad (3)$$

Assuming the normal dispersion has a weak response in the given spectral range $\Delta\tilde{n}(l) \approx \Delta\tilde{n}_0$ it is found out the plotting dependency shown by Fig.1

The curve on the Fig.1 has an oscillation form and equals zero at the points

$$\frac{p}{l_1}\Delta\tilde{n}(l)z = 2p\left(N + M + \frac{1}{4}\right), \qquad \frac{p}{l_2}\Delta\tilde{n}(l)z = 2p\left(N + \frac{1}{4}\right) \qquad (4)$$

for the wavelength l_1 and l_2 respectively, M is the number of cycles between l_1 and l_2, N is integer. Excluding z from (4) we have

$$N = \frac{\Delta\tilde{n}(l_2)l_1}{\Delta\tilde{n}(l_2)l_1 - \Delta\tilde{n}(l_1)l_2} M - \frac{1}{4} \approx \frac{l_1}{l_1 - l_2} M - \frac{1}{4}. \quad (5)$$

For the neighboring wavelengths we have M=1 and

$$N \approx \frac{l_1}{l_1 - l_2} - \frac{1}{4}. \quad (6)$$

The temperature control is brought along by means of the spectral measurement, i.e. the temperature changes causes the wavelength shift and are recorded by a spectrograph.

Evaluate the spectral temperature sensitivity $\frac{\P l}{\P T}$. From (4a) we have

$$\frac{\P l_1}{\P T} = \frac{1}{2(N+M) + \frac{1}{2}} \frac{\P(\Delta\tilde{n}_0 z)}{\P T}. \quad (7)$$

A boron-doped fiber has $\frac{\P\Delta\tilde{n}}{\P T} \approx \frac{\Delta\tilde{n}}{T - T_S}$, where T_S is a softening temperature so as for room temperature $T - T_S \approx 800^o C$ and $\frac{\P z}{\P T} \approx z\,5.5\times10^{-7}$ [2]. If M=1 we have $\frac{\Delta\tilde{n} z}{2N + \frac{5}{2}} \approx l_1$ and the spectral temperature sensitivity is

$$\frac{\P l}{\P T} \approx l_1\left(\frac{1}{T - T_S} + 5.5\times10^{-7}\right) \quad (8)$$

or $\frac{\P l_1}{\P T} \approx 0.8 nm/{}^0C$ at the wavelength $l_1 = 0.63 mm.$.

On the base of the above carried over consideration the follow conclusions may be drown.

The spectral temperature sensitivity of the one-arms fiber-optic interferometer does not depend explicitly on a fiber length. It is necessary only the temperature changes must cause changes of an optical fiber length no less than one wavelength.

The advantages of the given method are follows.

At first, when being a sum of the symmetric TM and TE modes the IV vortex is not very sensible to changes of a cut-off frequency at least as compared with HE_{11} mode. Indeed, as far as this fiber-optic system maintains only IV vortices it is responded to birth and death events of the TM and TE modes exclusively. The first mode pair is born at V=2.405 while the second one does it at V=5.52. This waveguide parameter corresponds to the cut-off wavelength $l_C = 0.347\,mcm$. It means that this wavelength is not analyzed by the experimental set-up. This thing extends the dynamics range of the device and reduces the measurement error.

The second, our experimental set-up has not the spiral polarization couplers since the measurement errors due to a temperature response of the couples are vanished.

The high spectral sensitivity about $\frac{\P l_1}{\P T} \approx 0.8 nm/{}^0C$ associated with the temperature resolution up to $2..4\times10^{-3}\,^oC$ enables us to originate super sensitive arrangement of temperature and other thermodynamics values.

References

1. R. Courts, A.V. Khomenko, A.N. Starodumov, N. Arzate, L.A. Zentano. Interferometric fiber-optic temperature sensor with spiral polarization couples// Optical Commun.,1998,V.154, P.268-272.
2. W.Eickoff. Temperature sensing by mode-mode interference in birefringent optical fiber. Optical Lett., V.6, No4, 1981,p.204-206.

4.4 New perspective approaches and their estimations

It was shown above that low-mode OVFS possess the greatest resolution among optical fiber sensors,. The basic mechanism is the temperature-induced changes of the phase and polarization states of a OV beam guided through thenfiber. Unfortunately, the transmission of OV through the conventional commercial fiber is very sensitive to external mechanical perturbations, so that the OV is decayed into different eigen-modes and a mode noise is induced in the device.

It has been well known technique of fabrication of the single-mode fiber at the expense of strong stresses inserting into a fiber material. Such optical fibers can preserve the mode polarization even if greatest ambient forces affect them.

In the given paragraph we shall consider some fiber constructions enable to preserve a single OV at large fiber lengths, which are designed on the base of single polarization-preserving fibers.

Assume that there are two kinds of optical anisotropy in some optical material, namely a linear birefringence Δn_L and a circular one Δn_C, where Δn is a difference between refractive indices of eigen- modes. In terms of plane waves, the response of that complex birefringent medium is expressed through the effective difference of the refractive indices Δn_R in a form [1,2]:

$$\Delta n_R = \sqrt{\Delta n_C^2 + \Delta n_L^2} \qquad (1)$$

Respectively, if the fiber has a complex birefringence, the polarization corrections to propagation constants of eigen-modes appear. If $\Delta n_L >> \Delta n_C$, the principal process is the linear birefringence and vice versa at $\Delta n_L << \Delta n_C$.

The main noise in the OVFS gives the IV mode. Its polarization correction is associated with the linear topological birefringence db_L [3], while the correction of Δb_C for the CV mode is unaffected by noise phenomena, whichoccur due to the circular birefringence. Consequently, if the strong circular birefringence takes place in the fiber ($d\tilde{b}_C >> db_L$), the mode noise in the fiber would vanish.

It has been also known [4] that the so-called “spun fibers” preserve the circular polarization of the fundamental HE_{11} mode. They have an elliptically screwed core and are fabricated by spinning of the platform during fiber drawing to impact the permanent twist of a fiber and thus to restore in average the circular symmetry of the waveguide structure. However, the transformation processes of guided OVs in such fibers are not yet studied.

In order to estimate the main features of the OV transformation process we have considered a fiber with a spirally screwed-core (see Fig.1).

(a) **(b)**

Fig.1. The spirally screwed-core fiber: (a) the single spiral; (b) the dual spiral.

A beam transmited through the spiral trajectory gains the topological Berry's phase [5]. In our case the Berry's phase per one turn of the spiral has a form:

$$g = 2p(1-\cos J) = 2p\left[1-\frac{1}{\sqrt{1+\left(\frac{h}{2p\,r}\right)^2}}\right], \qquad (2)$$

where r isthe radius of the spiral, h is the spiral pitch. The specific topological phase per unit length is

$$\Gamma = \frac{2p}{h}\left[1-\frac{1}{\sqrt{1+\left(\frac{h}{2p\,r}\right)^2}}\right]. \qquad (3)$$

The magnitude of the specific topological phase characterizes the polarization correction to the scalar propagation constant [6]: $\Gamma = d\tilde{b}_C$. Evidently, for the case $d\tilde{b}_C >> db_L$, the linear topological birefringence will be suppressed in the fiber, and the mode noise vanishes. For simplicity, we assume that $|db_L| \approx |db_C|$ in a step-index fiber [7] and

$$db_C \approx \frac{\sqrt{2\Delta}}{r\,V}, \qquad (4)$$

where r is the fiber radius, Δ is the height of the refractive index profile, V is the waveguide parameter and azimuth index *l=1*.

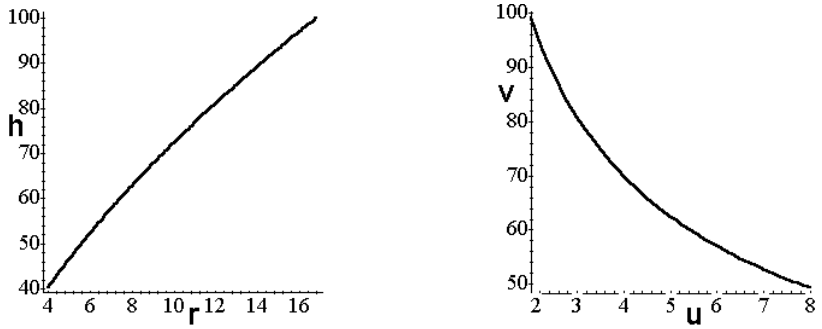

(a) **(b)**

Fig.2. The characteristic curve of the spirally screwed-core fiber. The scale r and h is in micrometers.(a). The same characteristic curve in the coordinates $u = 10^{-3}\frac{\left(\sqrt{2\Delta}\right)^3}{2pV}\frac{h}{r}$ and $v = \frac{r}{h}$ (b)

The Fig.2a,b represents the graphs of the characteristic curves.

$$\left(1-\frac{(2\Delta)^{3/2}}{2pV}\frac{h}{r}\right)^2\left(1+4p^2\frac{r^2}{h^2}\right)=1. \qquad (5)$$

The first curve in the Fig.2a was obtained from the inequality $d\tilde{b}_C >> db_L$ and eq. (3), (4) for typical fiber parameters: $\Delta \approx 10^{-2}$, $r = 4mm$, V=3.5. It is associated with the parameters of the spiral core only, while the second curve of the Fig.2b depends both from the parameters of the straight fiber itself and from its core torsion. The values of the spiral radius *r* and its pitch *h* above the curve of the Fig.2a correspond to the parameters of the spiral-core fiber preserving the guided OVs. At the same time, the values settled above the curve of the Fig.2b point to the admissible values of the straight fiber parameters at the given values of the torsion.

As a matter of fact, the real physical processes in the fiber are more complicated than presented above. Indeed, the spiral fiber is the waveguide with an imperfection of the refractive index along the optical axis. There is longitudinal modulation of the refractive index in the fiber, and hence there arises a counter waves due to the Bragg scattering. Moreover, azimuthally symmetric TE and TM modes are not realized in this system because of violation of waveguide symmetry. Instead of them it appears the new CV^S with a slightly different polarization correction than the CV has. As a result, any slight thermodynamical perturbations of temperature, pressure and so on, the spiral pitch changes cause violation of the Bragg's condition and detuning of the polarization corrections of the CV and CV^S vortices. If a polarization analyzer is positioned after the fiber output, there arise strong variations both of light intensity and thespectrum at the output of the OVFS.

We found also that the similar properties are to the elliptically screwed-core fiber (see Fig.3)

Fig.3. The elliptically-screwed core fiber.

It must be emphasized that the described above OV traits are mainly associated with phase properties of a wave than features of the OV beams. The point is that that guided OV in the fiber is itself an optical gyroscope similar to the mechanical top in a frame in contrast to the OV in free space that is similar to the top without a frame [8]. The main distinctive trait of the guided OV is the polarization correction db to the scalar part of the propagation constant $\tilde{b}$. The polarization correction db has been shown [8] to be immediately associated with the spin-orbit interaction as the same as that takes place for the mechanical gyroscope and other mechanical devices of the inertial navigation. Any variations of an angular position of the fiber coil stimulate changes of the polarization correction. Moreover, those changes depend both on a topological charge and a rotation rate. The magnitude of the polarization correction $db^{(G)}$ is proportional to the area enclosed by a single coil of a fiber during rotation and to the coil number. If two OVs formed as a topological dipole propagate along the rotating fiber, their centers begin to roll around the optical axis also. The rotation rate of the fiber coil is proportional to the rotation rate of the topological dipole. In contrast to the conventional fiber-optical gyroscopes in configuration of the Sagnac interferometer proposed OV device eliminates the counter-propagated waves and, consequently, eliminates all experimental errors inherent to a such OV interferometer.

References

1. A.V.Volyar, A.M. Bykov. Polarization optics of multimode lightguides // Optics and spectroscopy. 1984, 56,.894-899.
2. A. Yariv, Pochi Yeh. Optical Waves in Crystals. A Wiley-Interscience Publication, John Wiley & Son, New York, 1984.
3. A.V. Volyar, V.Z. Zhilaitis, V.G. Shvedov, M.S. Soskin, T.A. Fadeyeva Topological birefringence of optical vortices in an inhomogeneous media.// Optics of Atmosphere and Ocean. 1998. **11**, 1199-1214.
4. A.J. Barlow, J.J. Ramscov-Hansen, D.N. Payene. Birefringence and polarization mode-dispersion in spun single-mode fibers, Applied Optics,.**20**, 1981,.2962-2968.
5. M. Berry. Quantum phase corrections from adiabatic interaction // In Geometric phase in physics (ed. A. Shapere, F. Wilczek) Advanced Series in Mathematical Physics., **5**, 494-509. Singapore, New Jersey, London, Hong Kong, World Scientific. 1984.
6. A.V. Volyar, V.Z. Zhilaitis, V.G. Shvedov Optical eddies in small-mode fibers: 2. The spin-orbit interaction.// Optics and Spectroscopy. 1999, **86**, 664-670.
7. A.W. Snyder, J.D. Love. Optical Waveguide Theory. London-New York, Chapman and Hall, 1983.
8. A. Volyar, T. Fadeyeva Transmitting, destruction and self-recovery of the optical vortices in low-mode fiber-optical systems // SPIE proc. 2001. (to be published).
9. C.N. Alexeyev, M.S.Soskin, A.V. Volyar Spin-orbit interaction in a generic vortex field transmitted through an elliptic fiber // Semiconductor Physics, Quantum Electronics & Optoelectronics, 2000, **4,** 500-513.

4.5 Conclusions to chapter 4

We have made the analytical review and have shown the advantages and imperfections of optical sensors on the base of both single-mode and low-mode fibers. As a rule, a high sensitivity of these devices is immediately combined with errors at the expense of intensity fluctuations of a laser source. Besides, experimental results obtained by these sensors depend linearly on the beam phase difference only at narrow range of magnitudes.

We have developed and tested the specific physical approach to creation of the novel type of optical sensor: the OVFS, lacking a number of imperfections of the mentioned above schemes. This approach considers the OV interferometer as the complete wave system involving wave transmitting processes through the OV-generated unit, the vortex-guided unit, the vortex-recovered unit and on the final stage an interference image is subjected to a computer analysis by the processing unit. In accordance with our approach, the OV is employed as the signal or reference beam. The image obtained as a result of the waves superposition has the form of the interference spiral rotating around its axis due to the phase difference between the OV and a Gaussian beam. The computer processing of the spiral image instead of the measurement of the total intensity enables to avoid influence of intensity fluctuations. An angular position of the spiral image is proportional to the phase difference at a broad range of magnitudes. Two possible interferometric schemes were considered: (i) with an OV as the signal wave guided by the low-mode fiber and (ii) with an OV as the reference wave transmitted through free space and the single-mode fiber as the signal arm. The former device has temperature sensitivity about 180 $\frac{rad}{Km}$ while the latter one about 110 $\frac{rad}{Km}$. The specific technique of the image processing has been operated so that the measurement error of the device was only 0.01 rad and less and the reproducibility was up to 2 %. However, the former interferometer respondes rather strongly to ambient mechanical perturbations and the influence of coupled OVs implemented in the fiber.

This mode mixture was experimentally and theoretically revealed. The coupled OVs are suppressed and the single guided OV is recovered almost without any energy losses by the two-lens system. Also we have developed the technique of OV generation by an optical wedge.

Transmission through a fiber of short laser pulses is restricted by pulse duration. On the base of both the analytical consideration and computer simulation, we found that the contrast of an interference pattern is characterized not only by pulses mutual correlation in space and time but also by pulse dispersion. Two-arm OVFS cannot operate as optical sensors in the pulse regime. Nevertheless, we have developed and tested the one-arm OVFS suitable both for cw and pulse regimes. In this scheme, the CV, and HE_{11} modes propagate along the only fiber. The IV is partially suppressed by the circular polarization analyzer. The CV and HE_{11} modes have different responses to temperature influence and thus represent two interferometric "arms" launched into the single fiber. The angular position of the zero point of intensity characterizes the value of temperature. Such one-arm OVFS has low temperature sensibility, nothing but $2\frac{rad}{Km}$. However, we have theoretically developed a specific spectral technique raising the temperature sensitivity up to 200 $\frac{rad}{Km}$ and more.

We have studied the physical mechanism of OV decay in the conventional fibers and offered two novel fiber types preserving OVs., namely fiber with the spirally screwed core and the elliptical fiber with the twisting core, or «a spun fiber». Our estimations show that OV sensor on the base of the OV-preserving fiber is not merely high sensitive interferometer of thermodynamical values but it can be considered as the sensor for inertial navigation.

Conclusions to the project P 051

During one-year Partner Project P-051 a set of essential contributions were made into the understanding of the nature of optical vortices in free space, optical fibers and nonlinear media, as well as optical vortices assessment. Most important results are listed below.

Optical vortices understanding

1. New interference phenomena with optical vortices.

-The structure of transversal optical vortex around edge dislocation was analyzed. It was shown that interference of 2D Gaussian beams produces pair of edge dislocations. Their collapse and "unfolding" is possible in saddle-vortex topological reaction. Very important for understanding of edge dislocations was the consideration of phase velocity variation in the vicinity of zero-amplitude line. It was established that the transversal vortex rotates toward the region with *higher phase velocity.*

-It was predicted theoretically and realized experimentally the *spontaneous* (natural) birth of OVs by overlapping of mutually coherent non-coaxial co-propagating Gaussian beams with different parameters.

2. Diffraction and self-restoration of spatially truncated OV beams

-It was shown by computer simulation and experimental verification the effect of *self-restoration* of OV after up to 80 % cross-section screening of an OV beam, including its zero-amplitude axis, during free propagation behind the screen. This new nontrivial effect is a result of redistribution of the residual orbital angular momentum in the beam cross-section due to its rotation and diffraction behind the screen.

3. New type of topological charge and the orbital angular momentum transformation

-The observed transformation of OV beam passing through a cylindrical lens in the focal plane and vicinity was found to be quite unusual and unexpected. It was shown that orbital angular momentum of incident OV beam is conserved contrary to the topological charge of the axial OV, which changes its sign during passing through the focal plane. This effect needs more deep theoretical consideration.

-Theoretically calculated effect of the topological charge inversion during crossing of an OV "dipole" and circular edge dislocation was revealed.

Optical vortices assessment

1. Mode separator for a beam with an off-axis optical vortex

-The technique for spatial separation of modes with even and odd values of *modal index Q* was proposed and realized on the basis on two-arm interferometer with additional Gouy phase shift in one arm equal – *Q* ð. This simple technique allows to separate Laguerre-Gaussian modes and "purifying" in high extent an OV beam from parasitic coherent background.

2. Multichannel optical manipulator for microparticles

-The physical base for two-channel optical manipulator for microparticles has been developed. The manipulator was "constructed" as a focused singular beam possessing two OVs, with only one easy operating parameter for management of the OVs positions within the beam. Elaborated computer program simulates the process of manipulation.

-A new holographic technique was elaborated for creation of OV beams with fractional topological charges. It was predicted and shown by computer simulation that SHG of OV beam with fractional topological charge on the fundamental frequency possesses quite new features. Namely, the topological charge of SH of such OV beam depends in crucial way on the distance between the nonlinear element and the computer-synthesized hologram. This effect can be used for management of SH of OV beam.

3. The new high-resolution technique for testing of OV beam wave front

- A new technique for testing of OV helicoidal wave front in most delicate angular range inside the angle of diffraction divergence was elaborated and realized. It is based on multi-beams interference of OV beam put into a leaky waveguide. This technique deserves subsequent development and application.

4. Fiber-optical sensors based on optical vortices

The OV temperature sensors on the base of different types of optical fibers have been theoretically and experimentally studied. The OV fiber-optical sensor interferometer consists of the main units: the excitation system, the vortex guided system, the light output system and the detecting – computer processing system. The operation of the each unit was analyzed. Two types of interferometric configuration were considered: one- and two-arm interferometers. The advantages and disadvantages of these schemes were analyzed and the ways of their improvement were designed.

5. The new technique for OV beam generation

-The technique of efficient generation of optical vortices in free space was developed. The OV beam with efficiency up to 70% of conversion from a fundamental Gaussian beam by diffraction on a transparent optical wedge was obtained. The OV generation process was considered in detail both experimentally and theoretically. The optical and mechanical arrangement was elaborated for the optical fiber excitation.

6. Estimation of laser short pulses propagation in OV fiber sensors

-The coherence and duration of laser pulses is shown to limit the OV interferometer sensitivity. There are two physical phenomena decreasing the sensitivity of the vortex devices. The first one is that the optical path difference between the interferometer arms must be less than the pulse length. The second one is that a short pulse causes the spreading of an interference pattern due to a broadened spectral range. The analysis of the influence of these limitations was performed and computer simulation was realized.

7. Experimental realization of OV fiber sensors

-The one-arm OV fiber-optical sensor was experimentally developed. The temperature sensitivity of this device is up to $1-2\ \frac{rad}{K\cdot m}$. The two-arm OV fiber-optical sensor was experimentally developed. The temperature sensitivity of different types of these devices is up to $110-180\ \frac{rad}{K\cdot m}$ and the experimental error is up to 3×10^{-4} K. The linearity of the temperature measurement and reproducibility was verified. The test protocols of the examination of the devices are prepared.

Project manager Prof. Marat S. Soskin